



## AN ABSTRACT OF THE DISSERTATION OF

Gustavo Henrique T. C. de Albuquerque for the degree of Doctor of Philosophy in Chemical Engineering presented on March 17, 2017.

Title: Continuous Flow Microwave-assisted Synthesis as a Potentially Scalable Nanomanufacturing Approach

Abstract approved:

---

Gregory S. Herman

The development of nanomaterials and the potential enhancement of their chemical, mechanical, electrical, and optical properties have led to the investigation of methods for their synthesis at lower cost with enhanced performance for next generation devices. Along with the pursuit of new materials that exhibit properties of interest, industry requires scalable methods that enable high control over the final products properties. This work presents a promising approach in which microwaves are utilized in a continuous flow setup for the synthesis of nanomaterials. Microwaves induce the fast formation of nuclei and the rapid consumption of reagents leading to a separation of nucleation events from growth processes and consequent results in the formation of products with high uniformity. This method was employed in the synthesis of a metal-organic framework (MOF), and silver nanocubes. Both materials still present synthetic scalability issues. MOFs are hybrid porous materials that can have extremely high surface areas and low densities, making them suitable for gas storage applications. The continuous flow microwave reactor (CFMR) setup was used to synthesize MOF-74(Ni) particles with mild conditions of temperature and pressure

while obtaining high yields and high reagent utilization. This method provides a breakthrough in producing MOFs at larger scale. Silver nanocubes have exhibited enhanced catalytic and sensing performances that make them of scientific and industrial interest. The CFMR was used to allow the formation of highly monodisperse particles with high selectivities to the cubic shape. Formally,  $\text{Cu}_3\text{SbS}_4$ , or Famatinite, is a low band gap material with high absorption coefficients that can potentially be used in a tandem solar cell devices. High vacuum techniques are typically employed in deposition processes for solar cells, however a solution-based processing approach was performed with  $\text{Cu}_3\text{SbS}_4$  nanoparticles to develop a potentially cost-effective technique in fabricating solar cells. This dissertation will present an innovative and potentially scalable synthetic approach of nanomaterials and the use of inexpensive deposition steps that can potentially be used in applications including electronic, catalytic, gas storage, and membrane absorption systems.

©Copyright by Gustavo Henrique T. C. de Albuquerque  
March 17<sup>th</sup>, 2017  
All Rights Reserved

Continuous Flow Microwave-Assisted Synthesis as a Potentially Scalable  
Nanomanufacturing Approach

by  
Gustavo Henrique T. C. de Albuquerque

A DISSERTATION

submitted to

Oregon State University

in partial fulfillment of  
the requirements for the  
degree of

Doctor of Philosophy

Presented March 17, 2017  
Commencement June 2017

Doctor of Philosophy dissertation of Gustavo Henrique T. C. de Albuquerque  
presented on March 17, 2017

APPROVED:

---

Major Professor, representing Chemical Engineering

---

Head of the School of Chemical, Biological, and Environmental Engineering

---

Dean of the Graduate School

I understand that my dissertation will become part of the permanent collection of Oregon State University libraries. My signature below authorizes release of my dissertation to any reader upon request.

---

Gustavo Henrique T. C. de Albuquerque, Author

## ACKNOWLEDGEMENTS

I would like to firstly thank God for putting me into such a great family environment and for surrounding me with the amazing people I have met and learned from both in Recife and in Corvallis.

I want to dedicate this dissertation to my family, specially my mother Maria Roseane, aunts, and sisters, who gave up so much throughout the past 4 years and 6 months for my accomplishment or rather, our accomplishment. I want to specially thank my sister Berenice, my niece Christie, and my nephew Pedro who were always supportive in this journey. I want to thank my husband, Michael Springer, who has been very supportive and helped me through the difficult past two years. I wanted to give special mention to my friends Renato de Souza, Danilo Rodrigues and also the amazing friends that I have made through grad school—Ryan Frederick and Nicholas Kraaz—for their unconditional support.

From the CBEE staff, I would like to give my special acknowledgements to Charlotte Williams, Elisha Brackett, Lea Clayton, Andy Brickman, and Kristin Rorrer. They gave me great support in my PhD, besides being the kindest people.

The Herman group changed a lot over the course of my grad school period and I was honored to overlap with three different groups of scientists of various backgrounds who were very passionate and contributed substantially to my growth and continuous learning throughout my PhD. I should also thank Tristan Stickle, Derek Wong, Jonathon Lopez, and Abdulrahman Aldossary, who worked with me on several projects giving their contribution to this work.

I would like to thank Trey Diulus, Jonathon Lopez, and Dr. Sumit Saha for one of the greatest experiences I had performing experiments at a synchrotron source at the ALS. Dr. Richard Oleksak, Dr. Bob Fitzmorris, and Dr. Brendan Flynn for contributing to my PhD work and also for our great scientific trip to the Pacific Northwest National Laboratory.

In my assignments as a teaching assistant, I received a lot of influence from Professors Chang, Herman, Feng, and Koretsky. I am really grateful for all the lessons I learned from that experience, which substantially contributed to my flexible teaching/learning skills and also helped me develop my communication skills.

For the characterization techniques that I was exposed to, I would like to acknowledge all the people involved in my training on and off the OSU campus. Very experienced scientists made substantial contributions to my understanding of X-ray scattering and absorption, and electron microscopy. For that, I would like to thank Dr. Peter Eschbach, Teresa Sawyer, Josh Reznick, Prof. Nyman and Dr. Lev Zakharov. I also would like to specially thank Joe Bergevin for his humorous and thoughtful insight in some experimental issues.

I also wanted to acknowledge my first advisors Prof. Ingrid Weber, Prof. Cesar Moraes de Abreu, and Prof. Luciano Almeida, who gave me the inspiration to pursue this path. I need to thank my committee, who have been giving me guidance through the last years, but I would like to specially thank my advisor Professor Gregory S. Herman for providing a great combination of independent research and close guidance. He always let my curiosity drive my research and at the same time was always available to guide and help with science related and personal issues. I

could list many of the lessons learned from my advisor, however there is one saying that I would like to share with the readers of this work, which is: “There isn’t such a thing as a wrong experiment, there is an experiment that doesn’t tell you what you want to hear”.

Lastly and most importantly, I want to thank my father who sacrificed so much for my accomplishments. My father was my role model for good character, perseverance, and hard work. His dream was to live in an apartment on the roof of a hospital so he could rest and be ready to take care of his patients whenever he was needed. That was the example he gave me of how passionate for his work he was when I was just six. Being exposed to the routine of a doctor and dentist, made me quickly figure out that I wanted to be a chemical engineer and for that and many other great things, I would like to dedicate this work to my best friend and father, Luiz Carneiro de Albuquerque Filho.

## CONTRIBUTION OF AUTHORS

I am proud to say that a large number of scientists made contributions to this work. In chapter 3, where the synthesis of the MOF-74(Ni) is presented, the intellectual contribution of Dr. Fitzmorris and Dr. Kim needs to be acknowledged. In addition, Dr. Ahmadi contributed with beautiful TEM images and Dr. Wannemacher with the BET isotherms experiments. The important collaboration with two scientists of the Pacific Northwest National Laboratory (PNNL), Dr. Thallapally and Dr. McGrail were crucial for this work to be developed.

Chapter 6 involves the characterization of  $\text{Cu}_3\text{SbS}_4$  films, the intellectual contribution of Dr. Kim and Professor Chang, and Jonathon Lopez from OSU. Dr. Devaraj and Sundeep Manandhar from PNNL, and Dr. Liu from the Lawrence Berkeley National Laboratory gave intellectual contribution to this work.

Professor Gregory S. Herman contributed not only intellectually but also helped me in all steps of the preparation and the editing of manuscripts.

# TABLE OF CONTENTS

	<u>Page</u>
CHAPTER 1 .....	1
Segmented flow microwave-assisted synthesis of silver nanocubes .....	8
Gas-liquid segmented flow microwave-assisted synthesis of MOF-74(Ni).....	9
Structural and optical characterization of Cu <sub>3</sub> SbS <sub>4</sub> for solution-based thin film solar cells.....	10
CHAPTER 2 .....	17
X-ray Diffraction.....	18
X-ray absorption near edge structure .....	20
Electron Microscopy .....	21
Electron Sources.....	22
Electron Lenses .....	23
Electron interaction with matter .....	24
Scanning electron microscopy.....	25
Transmission electron microscopy .....	27
Bright Field Transmission Electron Microscopy.....	28
Selected Area Electron Diffraction .....	29
Scanning Transmission Electron Microscopy .....	29
Energy Dispersive Spectroscopy.....	30
Raman spectroscopy.....	31
Ultraviolet – Visible – Infrared spectroscopy .....	32

## TABLE OF CONTENTS (Continued)

	<u>Page</u>
Dynamic Light Scattering .....	33
Thermogravimetric Analysis .....	34
Inductively Coupled Plasma Optical Emission Spectrometry .....	35
Brunauer–Emmett–Teller isotherms .....	36
CHAPTER 3 .....	51
Abstract .....	52
Introduction .....	53
Experimental Section .....	54
Results and Discussion .....	57
Conclusions .....	63
Acknowledgments .....	64
CHAPTER 4 .....	72
Abstract .....	73
Introduction .....	74
Experimental section .....	76
Results and discussion .....	78
Conclusions .....	86
Acknowledgements .....	87
CHAPTER 5 .....	100
Abstract .....	101

## TABLE OF CONTENTS (Continued)

	<u>Page</u>
Introduction.....	102
Experimental section.....	104
Results and discussion.....	107
Conclusions.....	116
Acknowledgements.....	117
CHAPTER 6.....	128
Abstract.....	129
Introduction.....	130
Experimental section.....	132
Results and discussion.....	135
Conclusions.....	140
Acknowledgments.....	141
CHAPTER 7.....	151
CONCLUSIONS AND FUTURE DIRECTIONS.....	151
BIBLIOGRAPHY.....	155

## LIST OF FIGURES

<u>Figure</u>	<u>Page</u>
1: Qualitative representation of Gibbs Energy profile as bulk materials are transformed into precursors throughout the synthesis of nanoparticles.....	11
2: Gibbs energy profile dependence on the surface energy ( $\sigma$ ) and the bulk (volume) energy ( $\Delta G_V$ ).....	12
3: LaMer model describing burst of nucleation as conditions for nucleation such as temperature and supersaturation are achieved. ....	13
4: Qualitative description of the different synthetic approaches and main changes explained by the modifications added to the classical LaMer model. ....	14
5: Temperature profile of reactions using microwaves as the nucleation zone and the heating bath as a growth zone.....	15
6: Description of the segmented continuous flow microwave-assisted reactor being used for the MOF-74(Ni) synthesis. SEM image shows a MOF-74(Ni) particle.....	16
7: X-rays scattering from atoms of a crystalline sample.....	39
8: Simple schematic of fundamental phenomena that contribute to X-ray near edge structure spectra. ....	40
9: Detection modes of X-ray absorption near edge structure. TFY = Total fluorescence yield and TEY = Total electron yield. ....	41

## LIST OF FIGURES (Continued)

<u>Figure</u>	<u>Page</u>
10: Different observed phenomena when the primary beam interacts with an atom generating secondary electrons (Inelastic scattering), backscattered electrons (elastic scattering), Auger electrons, and photons.....	42
11: Sampling volume for each type of resulting emission due to the electron-sample interaction. The distances shown represent a rough estimation of the respective escape depths of each type of electron described and X-rays. ....	43
12: Scheme showing main parts of a transmission electron microscope (TEM) (Left) and a scanning electron microscope (SEM) (Right). ....	44
13: Bright Field Transmission Electron Microscopy (BFTEM) images of silver nanocubes. Left image shows cubes at lower magnification. Inset on the left and right image show silver nanocube in detail High Resolution Transmission Electron Microscopy mode (HRTEM). ....	45
14: (A) HRTEM of single $\text{Cu}_3\text{SbS}_4$ particle, (B) SAED of group of $\text{Cu}_3\text{SbS}_4$ particles, (C) STEM image of as synthesized $\text{Cu}_3\text{SbS}_4$ particles, and (D) Particle size distribution obtained using the STEM image shown in (C) .....	46
15: Fundamental phenomena that contribute to the detection of vibrational modes in Raman spectroscopy. The wavelengths shown in the figure represent the energy changes for each type of interaction. ....	47

## LIST OF FIGURES (Continued)

<u>Figure</u>	<u>Page</u>
16: Radiation interaction with an absorbing sample. Phenomenon is basic mechanism of UV-Vis-IR spectroscopy. ....	48
17: Representation of the elastic scattering phenomenon that occurs as a laser shines a dispersion of particles, which diffuse around in a liquid. ....	49
18: Types of isotherms presented by Brunauer <i>et al.</i> ....	50
19: TEM images of particles synthesized at $T_{MW} = 185\text{ }^{\circ}\text{C}$ $\tau_{GB} = 12\text{ min}$ using different concentrations of silver trifluoroacetate: (A) 282 mM, (B) 423 mM, and (C) 846 mM. (D) UV-Vis spectra for the solutions of the as-synthesize particles from each concentration used. ....	65
20: UV-Vis spectra of samples synthesized using the microwave zone only with different $T_{MW}$ 's being set for a fixed concentration of silver trifluoroacetate at 423 mM. ....	66
21: (A) UV-Vis spectra for the silver nanoparticles synthesized at different $T_{MW}$ and the addition of the growth bath with $\tau_{GB} = 12\text{ min}$ . The concentration of silver trifluoroacetate was fixed at 423 mM. TEM images show products obtained under those conditions for the respective $T_{MW}$ : (B) $T_{MW} = 135\text{ }^{\circ}\text{C}$ , (C) $T_{MW} = 155\text{ }^{\circ}\text{C}$ , and (D) $T_{MW} = 185\text{ }^{\circ}\text{C}$ . ....	67

## LIST OF FIGURES (Continued)

<u>Figure</u>	<u>Page</u>
<p>22: UV-Vis spectra of silver nanoparticles synthesized using different growth bath residence times (<math>\tau_{GB}</math>) and different microwave temperatures (<math>T_{MW}</math>) for 423 mM of silver trifluoroacetate. ....</p>	68
<p>23: (A) UV-Vis spectra of samples synthesized with 282 mM of silver trifluoroacetate with different <math>T_{MW}</math> being used and with a <math>\tau_{GB} = 12</math> min. For the <math>T_{MW} = 185</math> °C, samples had an additional batch growth containing NaBr which are also included in (A). (B) TEM image of nanocubes synthesized using <math>T_{MW} = 185</math> °C and 20 min of NaBr batch. (C) HRTEM image of a single nanocube, and (D) SAED of single crystal cube shown in (C). ....</p>	69
<p>24: X-ray diffraction of film of silver nanocubes shown in Figure 23(B). Reference pattern was taken from the RUFF open database (RRUFF ID: R070463). ....</p>	70
<p>25: Selectivity and TEM average diameter or edge length for cuboctahedra and cubes, respectively were summarized. (A) Average edge lengths for the three routes (<math>T_{MW} = 185</math> °C, <math>\tau_{GB} = 12</math> min/Different silver trifluoroacetate concentrations) to synthesize ~ 28, 42, and 58 nm silver nanocubes. (B) Average edge length/diameter and selectivity for different <math>T_{MW}</math>'s, <math>\tau_{GB} = 12</math> min, and silver trifluoroacetate concentration = 423 mM. ....</p>	71
<p>26: Schematic of segmented continuous flow microwave-assisted synthetic reactor for MOF-74(Ni). Model on top right was obtained using Comsol<sup>®</sup> shows turbulence in between slugs in segmented flow. ....</p>	90

## LIST OF FIGURES (Continued)

<u>Figure</u>	<u>Page</u>
27: XRD data from MOF-74(Ni) synthesized at different $T_{MW}$ compared to a sample, which has been synthesized using a combination of both microwave zone and growth zone. (Peak at $2\theta = 44^\circ$ present in samples from microwave only synthesis is due to XRD metal sample stage) .....	91
28: Raman spectra of MOF-74(Ni) samples, which were synthesized at different $T_{MW}$ compared to a sample that went through a combination of microwave zone and growth zone.....	92
29: XRD data of samples synthesized at different $T_{MW}$ while growth zone was maintained at constant temperature and residence time. (XRD peaks at $31.75^\circ$ are shown in inset) .....	93
30: Raman spectroscopy of MOF-74(Ni) samples synthesized at different $T_{MW}$ while growth zone was maintained at constant temperature and residence time. ....	94
31: TEM images of samples synthesized without microwaves (A) and at $T_{MW} = 70$ and $150^\circ\text{C}$ (B and C, respectively). ....	95
32: Particle size measurements using on dynamic light scattering taken for samples synthesized with and without microwaves, and different $T_{MW}$ .....	96

## LIST OF FIGURES (Continued)

<u>Figure</u>	<u>Page</u>
33: N <sub>2</sub> physisorption isotherms obtained for segmented continuous flow synthesis of MOF-74(Ni) with and without the use of microwaves. T <sub>MW</sub> was also varied keeping the average residence time constant (0.93 s) while growth zone conditions were fixed at 130 °C for 8 min. ....	97
34: Cumulative surface area (solid lines) and Incremental surface area (crosses) for MOF-74(Ni) synthesized using segmented flow with and without the use of microwaves. T <sub>MW</sub> was also varied keeping the average residence time constant (0.93 s) while heating zone conditions were fixed at 130 °C for 8 min.....	98
35: Thermographic analysis performed on MOF-74(Ni) samples synthesized with and without microwaves, and at two different T <sub>MW</sub> . ....	99
36: Percent conversion of Ni <sup>2+</sup> for reactions carried out with different microwave temperatures and BA to Ni <sup>2+</sup> concentration ratios (A), and a plot of natural logarithm of the rate constant (k) versus inverse temperature for each BA to Ni <sup>2+</sup> concentration ratios (B), where the estimated activation energies are provided. ....	118
37: Powder X-ray diffraction of samples synthesized at different BA and Ni <sup>2+</sup> concentration ratios. Inset provides and expanded view of the peak at 31.75 °. ....	119
38: Raman spectroscopy of samples synthesized at different BA and Ni <sup>2+</sup> concentration ratios.....	120

## LIST OF FIGURES (Continued)

<u>Figure</u>	<u>Page</u>
39: Dynamic light scattering results for samples synthesized at different BA and Ni <sup>2+</sup> concentration ratios. ....	121
40: LaMer model and modulating effects in relatively short synthesis of MOFs causing formation of larger and more uniform crystals. (After Diring <i>et al.</i> ).....	122
41: Adsorption (Ads.) and desorption (Des.) cycles of N <sub>2</sub> physisorption isotherms for samples synthesized using different BA and Ni <sup>2+</sup> concentration ratios.....	123
42: Incremental surface area (ISA) and cumulative surface area (CSA) estimated from N <sub>2</sub> physisorption isotherms for samples synthesized using different BA and Ni <sup>2+</sup> concentration ratios. ....	124
43: Relative mass of metals adsorbed in MOF-74(Ni)/Nafion® composite films. Relative mass was estimated by the difference in metal wt.% between composite and pure polymer film determined by ICP-OES divided by the amount of MOF estimated in samples.....	125
44 X-ray diffraction of pure polymer (Nafion®) and composite films as prepared and after exposure to copper nitrate solution. The exposed sample was representative of other samples exposed to metals. Inset shows the most intense diffraction peak that characterizes the MOF-74(Ni) - interplanar spacing (-120). ....	126

## LIST OF FIGURES (Continued)

<u>Figure</u>	<u>Page</u>
<p>45: Raman spectra of unexposed composite film, of a composite film after exposure to copper nitrate, and of a composite film after exposure to silver nitrate. (A) Raman spectra of composite samples exposed to silver and copper nitrate. (B) Expanded range of composite samples exposed to copper and silver nitrate that shows formation of new peaks for the case in which silver nitrate was used. ....</p>	127
<p>46: X-ray diffraction pattern of as-synthesized <math>\text{Cu}_3\text{SbS}_4</math> nanoparticles. Patterns for <math>\text{Cu}_{12}\text{Sb}_4\text{S}_{13}</math> and <math>\text{Cu}_3\text{SbS}_4</math> were published elsewhere. ....</p>	143
<p>47: (A) HRTEM image of single <math>\text{Cu}_3\text{SbS}_4</math> particle, (B) SAED of a group of <math>\text{Cu}_3\text{SbS}_4</math> particles, (C) STEM image of as synthesized <math>\text{Cu}_3\text{SbS}_4</math> particles, and (D) Particle size distribution obtained using the STEM image shown in (C) .....</p>	144
<p>48: (A) X-ray diffraction of <math>\text{Cu}_3\text{SbS}_4</math> films after air anneal only and after air anneal followed by different conditions of sulfurization. (B) X-ray diffraction of film prepared at optimized sulfurization condition and air anneal only. Labeled peaks: (*) CuS and (**) Mo. Patterns for <math>\text{Cu}_{12}\text{Sb}_4\text{S}_{13}</math> and <math>\text{Cu}_3\text{SbS}_4</math> were published elsewhere. ....</p>	145
<p>49: Ternary diagram for Cu, Sb, and S showing regions of formation of binary and ternary phases that can be formed at <math>T = 300\text{ }^\circ\text{C}</math>. (After Braga <i>et al.</i>) .....</p>	146

## LIST OF FIGURES (Continued)

<u>Figure</u>	<u>Page</u>
50: (A) Top-view SEM image of $\text{Cu}_3\text{SbS}_4$ film that underwent sulfurization at $500^\circ\text{C}$ / 50 min, (B) Top-view SEM image of $\text{Cu}_3\text{SbS}_4$ film that underwent sulfurization at $550^\circ\text{C}$ / 30 min, (C) Top-view SEM image of $\text{Cu}_3\text{SbS}_4$ film that underwent sulfurization at $500^\circ\text{C}$ / 10 min, (D1) Cross-section SEM image of $\text{Cu}_3\text{SbS}_4$ film that underwent sulfurization at $500^\circ\text{C}$ / 10 min, and (D2) Cross-section SEM image of $\text{Cu}_3\text{SbS}_4$ film that was only annealed in air. ....	147
51: UV-Vis spectroscopy of films annealed in air only and annealed in air along with undergoing the optimized sulfurization process. ....	148
52: Raman spectroscopy (A) using $\lambda = 785$ nm laser and (B) using $\lambda = 532$ nm laser. Samples analyzed were films annealed in air only and annealed in air along with undergoing the optimal sulfurization process. $\delta_p$ is the estimated penetration depth calculated based on the absorption coefficient of each sample. Reference spectra are part of the RRUFF database: Famatinite (ID: R110022) and Covellite (ID: R060306) .....	149
53: X-ray Absorption Near-Edge Structure (XANES) of films after the air annealing process only and of films after the air annealing process and the following optimal sulfurization process. (A) XANES results from the fluorescence detector and (B) XANES results from the detection of total electron yield. References shown in dashed lines were published elsewhere.....	150

## LIST OF TABLES

<u>Table</u>	<u>Page</u>
1: Particle size obtained from dynamic light scattering and scanning electron microscope. Particles were measured using software ImageJ <sup>®</sup> . ....	88
2: Reagents conversion (evaluated using UV-Vis spectroscopy for Ni <sup>+2</sup> concentration), mass production rate of MOF-74(Ni), and XRD full width at half maximum (FWHM) from reactions operated in segmented flow at different T <sub>MW</sub> ....	89

In dedication to Luiz Carneiro de Albuquerque Filho, the main reason why I pursued this path. And for Rose, Pedro and Mike, who were the reasons that made me stay on that path.

“It is great that God made us both more than father and son  
He allowed us to share the brightness of the sun that for many will never rise.”

Free translation of an excerpt of the song by Rick and Renner,  
“Mais que pai e filho”, “Passe o tempo que passar”, Warner Music Brasil, 2008.

CHAPTER 1  
INTRODUCTION

Nanotechnology is a science that encompasses materials and processes that occur on the nano-scale. Typically, this covers a size range that is lower on the than 100 nm. In nanotechnology, the use of nanoparticles as smaller portions of materials existing in bulk form has gained importance due to their applications in paints, solar cells, lighting, catalysis, bioimaging, and drug delivery. The search for materials of smaller size is justified by the possible enhancement of their chemical, mechanical, electrical, and optical properties when compared to their bulk configurations due to changes in surface area and other properties.

Although there are many properties within this size scale that are of interest, there are also many challenges involving manufacturing strategies and stability of nanoparticles. Typically, smaller particles possess higher Gibbs energies than bulk materials due to having a higher surface area to volume ratio. Figure 1 shows a qualitative Gibbs energy profile that describes the energetic changes in the process of producing nanoparticles. These precursors require energy to be produced and after the formation of small particles, materials of bulk size will be favored for being at lower energy levels. Therefore, efficient manufacturing approaches should provide an adequate amount of energy in order to create useful nanoparticles.

There are well known chemical and physical approaches that can lead to the formation of nanoparticles, however the mechanical formation of crystals generally leads to formation of particles with wide particle size distributions. Chemical processes can overcome this problem by providing homogeneous products but require large amounts of energy to convert bulk materials into reactive species that can be used in synthetic routes to produce nanoparticles.<sup>1</sup> This disadvantage provides

motivation for investigating more sustainable processes following chemical or physical routes to produce materials of homogeneous size and properties in large scale, which will increase the nanoparticles feasibility from the industrial perspective.

Chemical approaches rely heavily on integrating knowledge of thermodynamics and kinetics to generate homogeneous particles from their precursors. Stabilizing agents, capping agents, and digestive ripening are some of the strategies used to prevent further nucleation events and agglomeration, which lead to formation of non-homogeneous particles.<sup>22</sup> Although these mechanisms try to reduce the speed of growth or increase stability of particles by using steric or repelling effects, uniform nucleation events must be ensured prior to these steps to increase efficiency.

Nucleation is the process in which the first atoms or molecules in a given phase start agglomerating to generate small, metastable structures with the characteristics of a new phase. Most models that describe nucleation using thermodynamics of equilibrium between phases still rely on the classic nucleation model, which uses the minimization of Gibbs energy and maximization of entropy of the entire system. Two types of nucleation comprise the classic nucleation model: homogenous and heterogeneous nucleation. Homogeneous nucleation occurs randomly in the bulk of the original phase as opposed to heterogeneous nucleation, which requires a surface or nucleation sites to initiate, such as on the surface of particles (seeded growth mechanism).

Figure 2 describes the classic nucleation approach describes the change in Gibbs energy and the influences of volume and surface energies on the general Gibbs

energy expression. While particles are formed, a change in free energy occurs as atoms/molecules start agglomerating to form the first clusters. This change in free energy is a result of a combination of interatomic bonding and the establishment of an interface in-between the nuclei and their surroundings. Both terms are size dependent, and as conditions of supersaturation and energy allow formation of nuclei, there is a maximum size (" $r_c$ " = critical radius) at which an energy barrier for nucleation is defined ( $\Delta G_C$ ). To achieve spontaneous nucleation, this energy barrier needs to be exceeded while smaller particles ( $r < r_c$ ) would dissolve and larger particles ( $r > r_c$ ) would grow. The critical radius and the nucleation would largely depend on variables such as temperature and supersaturation conditions. A formulation developed by Becker and Doring in 1935, shown in Equations 1-4, is used to describe nucleation phenomena, where nuclei radius ( $r$ ), surface energy ( $\sigma$ ), and volume/bulk energy ( $\Delta G_V$ ) are considered for the estimation of the Gibbs energy of the entire system.<sup>3</sup> In light of this conceptual model, an expression for nucleation rate ( $J$ ) could also be obtained as a parameter expressed in terms of temperature and an Arrhenius-like energy barrier Equation 5. This energy barrier may be substantially reduced if a nucleation site is available in the medium due to a need of an interface which typically drives the Gibbs energy to higher values.

$$\Delta G = -\frac{4}{3}\pi r^3 \Delta G_V + 4\pi r^2 \sigma \quad (1)$$

$$\text{when } \frac{d(\Delta G)}{dr} = 0 \quad (2)$$

$$r_c = \frac{2\sigma}{\Delta G_V} \quad (3)$$

$$\Delta G_c = \frac{16\pi\sigma^3}{3(\Delta G_V)^2} \quad (4)$$

$$J(T, \Delta G_c) = A \cdot e^{-\frac{\Delta G_c}{k_B T}} \quad (5)$$

In 1950, Lamer *et al.* described the phenomenon of the burst of nucleation for sulfur particles.<sup>4</sup> In this model, described qualitatively in Figure 3, it is assumed that the concentration of a hypothetical monomer has an increasing growing concentration, which continues to increase until growing above the supersaturation level. The association of supersaturation and temperature can overcome the barrier for nucleation, which then leads to the rapid formation of particles related to a marked decrease in the concentration of the monomer. This fast increase in concentration driving a burst of nucleation is considered an efficient strategy for chemical synthesis due to the separation of the nucleation events from the subsequent growth. Figure 3 also shows the growth region, where the increase in particle size is driven by the gradient of concentration and reduced barrier energy for growth (heterogeneous nucleation). As the monomer concentration approaches the saturation limit, Ostwald ripening causes the formation of larger particles by reducing the surface energy of the system; causing larger, more stable, particles to grow and smaller, less stable, particles to dissolve into the medium. There are several different strategies to increase the homogeneity of particles and the model developed by Lamer *et al.* allows an analysis of the imposed changes by each synthetic approach.

The main three methods used to control nucleation and growth of particles in batch chemical synthesis are the heat-up method, the hot injection method, and the “extended-LaMer” method. The heat-up method is the simplest approach, which consists of heating a mixture containing precursors to a temperature necessary to induce nucleation of particles. While the solution is heated, nuclei are formed and start to grow as additional nucleation events take place, leading to the formation of polydisperse particles. This method pays for its simplicity because of the overlap between the nucleation and growth steps.

Another common approach is the hot-injection method. As most reagents stay in the reactor at the reaction temperature, a limiting reagent, which is needed for the reaction to start, is injected quickly allowing the reaction to begin. That precursor rapidly reaches supersaturation and causes the fast formation of nuclei and decrease in concentration from the liquid phase while solids are formed. This approach separates the nucleation from the growth steps leading to the formation of particles of high uniformity.<sup>5</sup>

A more recent approach is the promising “extended-LaMer” method. This method uses a very well controlled growth step by introducing the primary reagent gradually into the system to produce particles with a linear growth correlation with time. This method avoids the Ostwald ripening step by keeping the concentration of precursors above the solubility limits, but a fine control over the nucleation step is not attempted. However, an excellent control over particle size can be achieved after a certain threshold of minimum size is reached. Figure 4 describes qualitative

differences obtained by each of these methods using the classic LaMer model to explain advantages of alternative synthetic approaches.<sup>6</sup>

The methods described present good results in the lab scale with yields typically smaller than 50 mL. However, from the industrial perspective, developing scalable processes that can impose similar changes of concentration (mass transfer) inducing the formation of uniform particles is difficult. In addition, the temperature gradients in larger batches would also lead to formation of polydisperse particles that impact the performance of devices or products that depend on uniform physical and chemical properties.

This work presents an alternative approach in which microwaves are utilized in synthesis of nanomaterials. In a continuous flow system, microwaves can be used to induce the fast formation of nuclei and the separation of the nucleation from the growth event by depleting the concentration of reagents very quickly, therefore avoiding any following nucleation. When compared to conventional heating, microwave heating is an excellent approach for initiating nucleation because of the rapid and uniform volumetric heating that lead to instantaneous nucleation, homogeneous growth, and high reproducibility of reactions. The advantages of microwaves associated with continuous flow (reproducibility, facile automation, efficient mass and heat transfer) can make synthesis of nanoparticles scalable and more feasible.<sup>7</sup> Finally, the particles are taken into a growth bath and reaction residence times can be easily tuned to make the system yield particles of with properties of interest. Figure 5 shows the temperature profile of a synthesis of nanoparticles using this approach causing a fast heating in a matter of seconds leading

to the formation of monodisperse particles with separation of the nucleation from the growth steps.

The study of the control of the nanoparticle nucleation step using a continuous flow microwave-assisted setup was performed for two different systems of particles. Metal-organic frameworks (MOF) and silver nanocrystals were synthesized using simple chemistries to produce nanocrystals that achieves high yield and uniformity with a potentially scalable method. This study will be divided into five chapters: Chapter 2 includes the analytical techniques that were used in the subsequent work; Chapter 3 has a detailed discussion on the selective synthesis of monodisperse silver nanocubes of different sizes using a continuous flow microwave reactor. Chapters 4 and 5 include the synthesis of a metal-organic framework (MOF), more specifically the MOF-74(Ni), with Chapter 4 detailing the microwave effects involved in the synthesis and Chapter 5 focusing on the change in the synthetic approach used, as well as the formation of monodisperse MOF-74(Ni) particles; Finally, Chapter 6 will discuss the study of the thermal processing of  $\text{Cu}_3\text{SbS}_4$  nanoparticles for thin film-based solar cell devices.

#### Segmented flow microwave-assisted synthesis of silver nanocubes

In Chapter 3, the fine control over the nucleation step was again tested with the synthesis of a new system of nanocrystals. The use of a segmented flow continuous microwave reactor to selectively synthesize silver nanocubes was discussed. There have been multiple attempts at synthesizing silver nanocubes with

high monodispersity. In this work, the effects of concentration, microwave temperature, and residence times are discussed and scalable routes to synthesize monodisperse silver nanocubes of 20, 45, and 60 nm are shown. The use of nanocrystals of different shapes allows the studies of phenomena that occur at the specific planes that are exposed. Therefore, the application of particles of different shapes in the preparation of sensing devices, of catalysts, and conductive inks are of industrial and scientific interest.<sup>8,9</sup>

#### Gas-liquid segmented flow microwave-assisted synthesis of MOF-74(Ni)

Metal-organic frameworks (MOFs) are hybrid coordination polymers formed from the coordination of ions or ion clusters with polytopic organic linkers. MOFs present high surface areas and low densities becoming ideal for adsorption and storage applications. However, their synthesis is still a limiting step to their commercialization due to the duration of batch processes and the relatively high temperature and pressure conditions of continuous synthetic approaches. In Chapter 4, a synthetic approach using a continuous flow microwave-assisted reactor (Figure 6) will be discussed. That process allowed the synthesis of MOF-74(Ni) with high space-time yield ( $\sim 90 \text{ g}\cdot\text{h}^{-1}\cdot\text{L}^{-1}$ ) and 96.5 % conversion of reagents. Separation of nucleation and growth steps was performed by using uniform and rapid microwave heating to induce nucleation and differences in MOF-74(Ni) properties were observed as synthesis conditions were changed.

In Chapter 5, the synthesis of MOF-74(Ni) was modified and the addition of a

modulating agent was performed. Chapter 4 demonstrates that high temperatures in the microwave zone induced fast nucleation, but this also resulted in an increase of polydispersity of products at certain conditions. Benzoic acid was used as a chemical modulator and an optimization of the synthetic process resulted in MOF-74(Ni) particles with high crystallinity, high surface area, and narrow particle size distributions.

#### Structural and optical characterization of $\text{Cu}_3\text{SbS}_4$ for solution-based thin film solar cells

In chapter 6, the preparation of  $\text{Cu}_3\text{SbS}_4$  films and their structural and optical properties are investigated. The most efficient inorganic, thin film-based solar cells rely on toxic (Cd) and/or scarce elements (In, Te). The search for more sustainable processing of solar technologies has led to the identification of many Earth abundant and non-hazardous copper chalcogenide absorber materials such as  $\text{Cu}_x\text{Sb}_y\text{S}_z$ .  $\text{Cu}_3\text{SbS}_4$  (also known as Famatinite) is a low band gap ( $\sim 0.9$  eV) material with high absorption coefficients ( $\sim 10^4$  -  $10^5$   $\text{cm}^{-1}$ ), which makes this material of interest for application in a tandem solar device.<sup>10</sup> In this work, the use of nanoparticle inks to prepare thin film based solar cells was investigated using a cost-effective approach for producing higher performance solar cells.

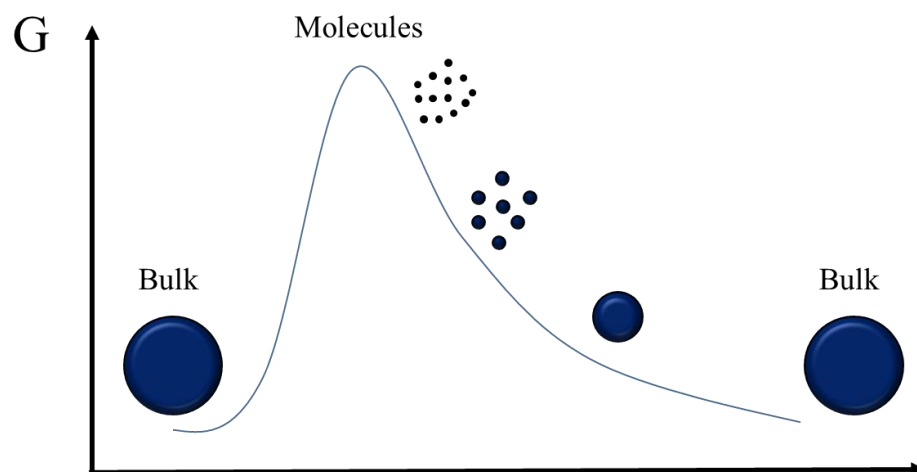


Figure 1: Qualitative representation of Gibbs Energy profile as bulk materials are transformed into precursors throughout the synthesis of nanoparticles.

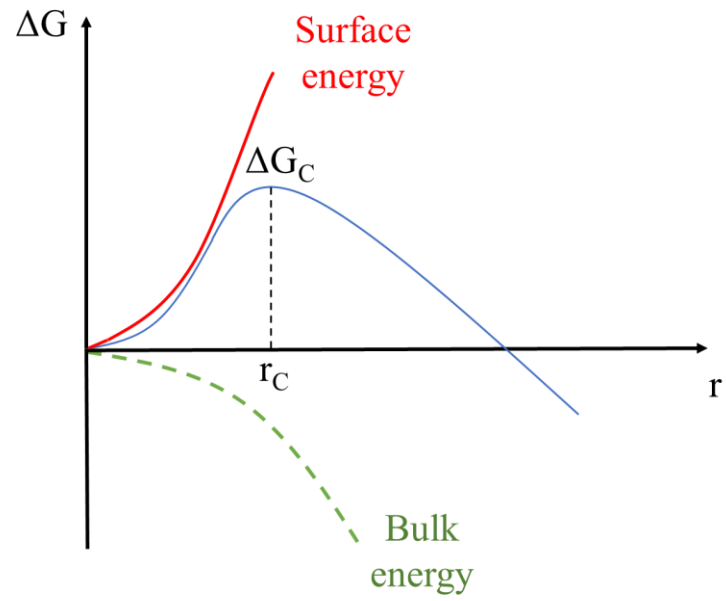


Figure 2: Gibbs energy profile dependence on the surface energy ( $\sigma$ ) and the bulk (volume) energy ( $\Delta G_V$ ).

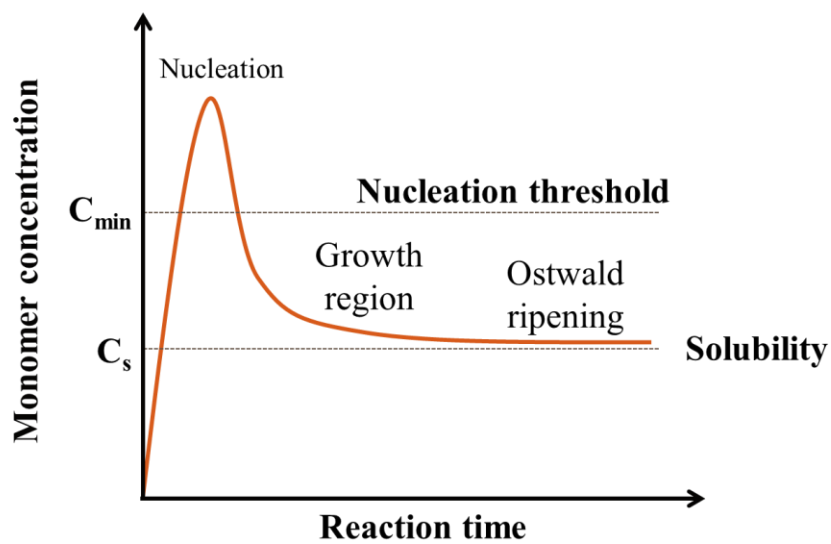


Figure 3: LaMer model describing burst of nucleation as conditions for nucleation such as temperature and supersaturation are achieved.

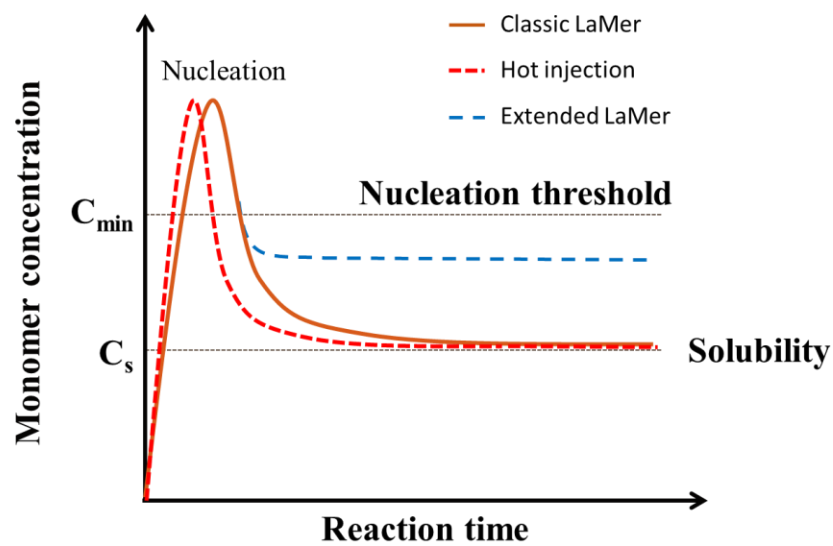


Figure 4: Qualitative description of the different synthetic approaches and main changes explained by the modifications added to the classical LaMer model.

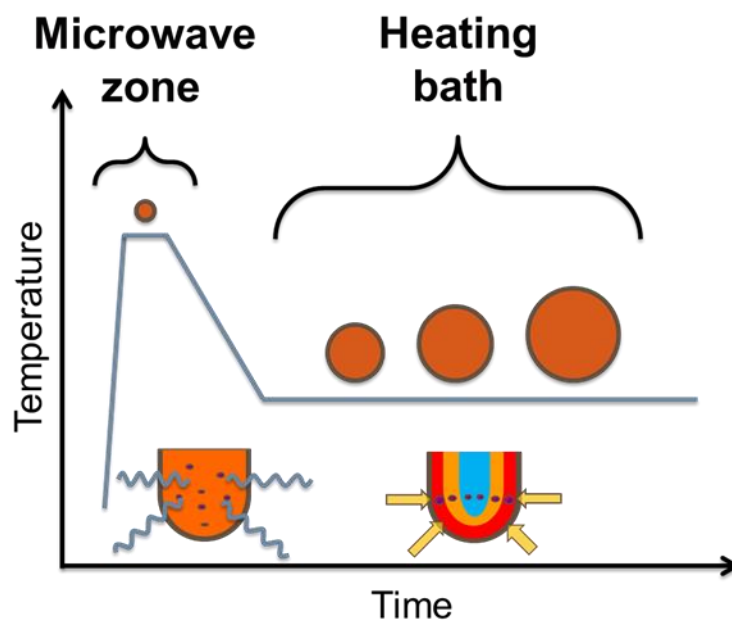


Figure 5: Temperature profile of reactions using microwaves as the nucleation zone and the heating bath as a growth zone.

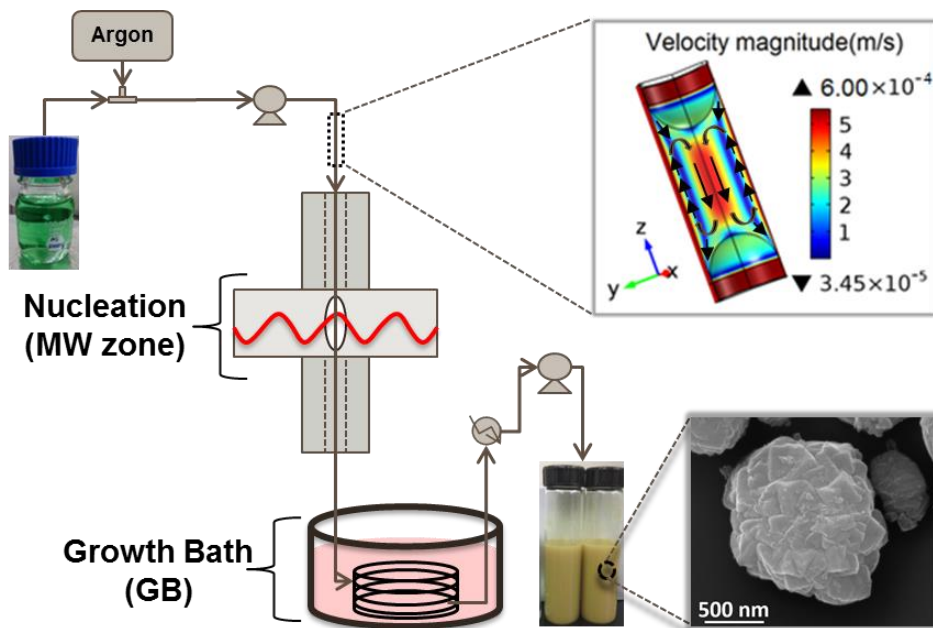


Figure 6: Description of the segmented continuous flow microwave-assisted reactor being used for the MOF-74(Ni) synthesis. SEM image shows a MOF-74(Ni) particle.

CHAPTER 2  
ANALYTICAL TECHNIQUES

Characterizing the properties of an unknown material requires techniques that perturb atoms within a sample. Measuring the resulting changes in the sample yields information that can be used to understand the characteristics of the original system. For example, incoming photons interact with the Earth's atmosphere which results in the apparent colors of the sun and sky as being yellow and blue, respectively. The principle of Rayleigh scattering states that these colors arise when molecules in the atmosphere scatter shorter wavelengths of the sun's light more efficiently than longer wavelengths.<sup>11</sup> If the atmosphere were comprised of a substance with molecules of different elements and properties, a different perception of color would arise. The interaction between radiation and matter allows scientists to answer fundamental questions about materials. Characterization techniques will be introduced in this chapter, and a mechanistic emphasis will be placed on the way that the data used in subsequent chapters were gathered.

## X-ray Diffraction

X-ray diffraction (XRD) relies on the dual particle/wave behavior of X-rays to obtain structural information from samples. An incident beam of a known wavelength is scattered by atoms from a sample. For materials with a consistent spacing between atoms, which is a consequence of long-range order or crystalline behavior, X-rays will interfere constructively and destructively as a function of an angle to the surface

plane, creating a pattern that is characteristic of a crystalline phase. Figure 7 describes this phenomenon as resulting X-rays are detected at different “ $2\theta$ ” angles.

This phenomenon was discovered in 1912 by Max von Laue, who observed that crystalline materials could act as diffraction slits for radiation of wavelengths that are similar to crystalline spacings.<sup>12</sup> In 1913, Sir W. H Bragg and his son Sir W. L Bragg developed an equation that is known as Bragg’s law (Equation 6), where  $n$  is an integer that represents the “order” of the reflection,  $\lambda$  is the wavelength of the X-ray source,  $d$  is the interplanar spacing of the crystalline material, and  $\theta$  is the angle of incidence of X-rays to the surface plane of the sample.

$$n \cdot \lambda = 2d \cdot \sin\theta \quad (6)$$

X-rays sources typically are produced by a heating filament, which is biased so thermionic generation of electrons can cause emission towards a positive target (anode), which is a metal such as copper. X-rays are then generated in all directions as the bombarded electrons result in the characteristic emission for the metal target being used. The beam is directed to the sample with an incidence angle that may be fixed or variable depending on the sweep mode of choice. X-rays are then scattered and detected as a function of the scattering angle. Finally, the moving detector converts X-ray intensity into a current measurement so a diffraction pattern can be displayed. These diffraction patterns can be used to identify crystal structures.

The Scherrer equation, Equation 7 allows a crystallite size ( $\tau$ ) to be estimated from the broadness of the XRD peaks. The broadness is usually estimated using the full width at the half maximum (FWHM) in radians (B). K is a constant that depends mostly on grain shape and distribution. Careful analysis of the XRD data with the Scherrer equation allows for an accurate determination of average crystallite size.<sup>13</sup> The main issues with this analysis are related to determining shape factors that are representative of samples and determining the sample broadening. There are several sources of broadening that may lead to inaccurate crystallite sizes such as X-ray source broadening, experimental setup and intrinsic scattering, and sample inherent broadening.

$$\tau = \frac{K \cdot \lambda}{B \cdot \cos(\theta)} \quad (7)$$

#### X-ray absorption near edge structure

X-ray absorption near edge structure (XANES) relies on the absorption of X-rays that interact with atoms of a given sample. As summarized in Figure 8, the incidence of X-rays of variable energies will cause the emission of electrons and photons from a sample.

As X-rays interact with core electrons and cause them to be excited into empty states or emitted from the sample, through this process core holes are created. Core holes are then filled by electrons that occupy higher energy levels, and either results in emission from an electron from a higher level (Auger Electron) or it results in

emission of a characteristic photon. Figure 9 shows two common detection modes of XANES. A detector absorbs photons emitted in all directions by the sample and that information is considered as total fluorescence yield (TFY). The current from the stage generates the total electron yield (TEY), which represents the total Auger electrons, photoelectrons, and secondary electrons emitted from the sample. As electrons have a short attenuation length ( $\sim$  nm), the TEY information from the detected current is very surface sensitive. The TFY information has a much larger sampling volume and is bulk sensitive.

## Electron Microscopy

Electron microscopy (EM) uses the interaction between electrons and matter to obtain an image of a specimen. Figure 10 qualitatively describes different ways electrons can interact with atoms and shows the emission of photons, of Auger electrons, secondary electrons, and the backscattered electrons. Electron scattering and absorption are the main mechanisms that allow the investigation of sample properties and imaging of the sample surface. Each of the detection modes that are available in EM will be further discussed below. This brief introduction to electron microscopy will now cover the main parts of electron microscopes and introduce the two types of electron microscopes used in this dissertation: scanning electron microscope (SEM) and transmission electron microscope (TEM).

The Rayleigh criterion (Equation 8) used for visible light microscopes can be used to determine the ultimate resolution of a microscope, where  $n$  is the refractive

index of the medium,  $\lambda$  is the radiation wavelength and  $\beta$  is half angle of the cone formed by the radiation as it passes the objective aperture.<sup>14</sup> This equation shows that the maximum resolution obtained by an instrument is directly related to the wavelength from the source of radiation. Therefore, electrons could be used to provide information from samples with a much higher resolution level. This search for higher resolution is what caused the creation of the field of electron microscopy science.

$$\text{Resolution} = \frac{0.612 \cdot \lambda}{n \cdot \sin(\beta)} \quad (8)$$

### Electron Sources

There are two main mechanisms that have been employed to generate electrons in electron microscopes. One type of electron source relies on a thermionic process and the other a field emission mechanism.

#### **Thermionic Emission**

Any materials can emit electrons at a given temperature if the energy provided overcomes their work function ( $\Phi$ ). However, there are not many materials that would be suitable to become a thermionic source due to structural changes caused by the excessive heat that can lead to melting or vaporization. Therefore, only refractory

materials (high melting point) with relatively low work functions are suitable for that task.<sup>14</sup> Tungsten filaments and LaB<sub>6</sub> crystals are materials that are commonly used in thermionic sources, although the operating temperature conditions in which these sources are maintained lead to shorter life times compared to field emission electron guns.

### **Field Emission**

The working mechanism of a field emission gun (FEG) is based on the large electric fields at a tip when a high voltage is applied to a material. A potential of the order of magnitude of 1 kV can lower the working function barrier for a tip of about  $\sim 0.1 \mu\text{m}$ , which creates an electric field of the order of  $10^{10} \text{ V/m}$  allowing an efficient tunneling process out of the tip. This process imposes high mechanical stress to the source, which is usually maintained at high vacuum and low temperatures. Tungsten and LaB<sub>6</sub> can be used as FEGs, which give much longer life times than thermionic sources but at the cost of the stability of current that results.

### **Electron Lenses**

As in light microscopy, lenses are used to control basic operating parameters such as brightness and focus in EM. EM lenses are metal coils that control alignment and direction of the electron beam through changes of magnetic field. In addition, just as in optical microscopes, the EM lenses are located along the column that the electrons go through after being accelerated at the source and towards the sample

chamber. Copper and iron are configured into coils to modify the strength of the field applied in the column to control electron trajectories.

### Electron interaction with matter

Figure 10 demonstrates several different types of processes that occur as a primary electron interacts with an atom. These processes depend on elastic and inelastic interactions. Elastic interactions are those that result in no energy loss or in negligible changes of energy of the primary electrons. Inelastic interactions rely on energy transfer from the primary electrons to the sample.

Lower energy electrons ( $< 50$  eV) are generated by inelastic scattering of the primary electron beam, which knocks a secondary electron (SE) out of the sample because of momentum transfer due to the dual particle/wave behavior of electrons.<sup>15</sup> The emission of secondary electrons are usually followed by emission of X-rays or Auger Electrons as a result of internal relaxation of electrons filling the created hole. Cathodoluminescence also results from the internal relaxation of electrons after secondary electrons are emitted, but the photon energies are in the visible range. Figure 11 shows the sampling volume for the various radiation types induced by interaction with the initial high energy electron beam. Depending on the radiation type, measurements might be limited to effects occurring very near the sample surface, or might be less surface-sensitive. Due to their low energies, secondary electrons have very short escape depths ( $< 5$  nm) and therefore they are very surface sensitive, which provides surface topography information in SEM. Backscattered

electrons (BSE) are generated by elastic scattering processes. These electrons result from the interaction between the primary beam electrons with nuclei of atoms present in the sample and possess much higher escape depth ( $< 100$  nm) due to their higher energy. (See Figure 10) BSE intensity is directly related to the atomic number of samples ( $Z$ ), which in SEM and TEM provide great contrast images. BSE's are also diffracted by crystalline samples before being detected therefore also allowing investigation of crystallographic information through electron backscattered diffraction (EBSD).

When core electrons are displaced because of momentum transfer from a primary electron, emission of X-rays characteristic to an element occur as the energy of the resultant radiation is specifically quantized. For each element, the energy of X-rays will be related to an internal relaxation in order to fill the hole. Characteristic X-rays possess compositional information and their long penetration depth, when compared to electrons, allows for much larger sampling volume to be investigated ( $< 5$   $\mu\text{m}$ ). On the other hand, Auger electrons can be used for very surface sensitive characterization as they possess very low escaping depths compared to SE's and BSE's. This allows the detection of electrons that escape from the top nanometer of the sample.

### Scanning electron microscopy

A SEM relies on the detection of BSE's and SE's using the differences between them to generate different types of images. Typically, modern SEMs use

field emission sources with accelerating voltages that vary from 1 to 50 kV. The electron beam goes through a column containing lenses and an extra set of coils control the scan rate to raster the surface to generate a 2D map of the sample. One of the peculiarities of a SEM is the resulting diameter of the electron beam, which is much smaller than the one used in TEMs.

Finally, the detection of electrons utilizes two different mechanisms in order to separate the BSE's from SE's emitted inside of the chamber. A 4-quadrant backscattered detector (BSD) is located above the sample and it contains a scintillator – a tool that converts the current intensity into photons. The BSD faces the sample being located over the sample and close to the objective aperture (through which the electrons pass when coming from the source through the column) since the backscattering process occurs normal to the surface and that increases the detection yield.

SE's are detected by a scintillator (biased at 10 kV) surrounded by a Faraday cage, which is also positively biased (100V). This detector known as the Everhart-Thornley detector and it is tilted in order to avoid BSE's detection and the positive cage accelerates the secondary electrons to the scintillator and a signal is created. Figure 12 shows the main parts of a SEM and the position of the mentioned detectors.

The scanning Auger microscopy (SAM) mode, along with the use of an Auger electron spectrometry (AES), can be used to build chemical maps that are highly surface sensitive. When a sputtering ion gun is used in combination with an AES, a very detailed chemical depth profile can be built, which adds a large amount of detailed information to a common electron microscopy image.

EBSD information is obtained using a phosphor screen that is located at a high angle from the surface plane of the sample so that diffracted electrons can be detected as they present constructive interference as predicted by Bragg's law.

### Transmission electron microscopy

TEMs, as the name implies, uses transmitted electrons through an ultra-thin specimen to produce images. The main reason for that is because this technique requires electrons to reach the detectors located at the bottom of the instrument after interacting with a sample and therefore the total attenuation of electrons would not allow image formation. Typically, TEM samples are thinner than 100 nm.<sup>14</sup>

Like SEM, TEM uses an electron source at the top of a column, however much higher acceleration voltages are employed (80-400 kV). The electron beam is guided through a column in which a series of lenses converge to a sample holder where a TEM grid is located. The sample size is not only limited by thickness but also by its surface area, as it must be placed into a 3 mm grid.

The detection mode relies on the primary electrons that make it through the sample. The atomic number ( $Z$ ) plays an important role when generating the contrast of images in TEM due to a higher generation of BSE's for higher  $Z$ -values. This trend results in fewer electrons passing through higher  $Z$  materials, which in the image leads to the appearance of darker spots where the sample presents higher density of elements with high  $Z$  value.

## Bright Field Transmission Electron Microscopy

The most simplistic mode of a TEM is when either a phosphor screen or a charge-coupled device (CCD) camera is used at the bottom of the microscope, which detects the resulting electron beam after the interaction with the sample generating a signal. This is how bright field TEM images are formed. Figure 12 shows main differences between the generation of images for SEM and TEM, as well as some basic detecting modes. The contrast in these images is strongly affected by the atomic number of elements that compose samples as discussed above. As magnification is increased, a careful analysis is needed due to the complexity of electron-sample interactions generating interference patterns. At high magnification level, high resolution TEM images (HRTEM) can be obtained. Figure 13 shows BFTEM images and HRTEM images of silver nanocubes, which were prepared by simple dropcasting of a solution of particles onto a TEM grid. The most common preparation of samples containing nanoparticles simply rely on giving contact time between the TEM grid and solution as well as allowing capillarity forces to help adhere particles to the grid film. In general, to create thin-film TEM samples from the sample of interest, a Focused Ion Beam (FIB) lift-out preparation is needed. During this process, it is necessary to remove a slice of the sample that is representative and also thin enough for successful TEM imaging. FIB lift-out procedures will not be covered herein, as this work focuses on nanocrystal synthesis.

## Selected Area Electron Diffraction

The dual wave/particle behavior of electrons also allows them to provide crystallographic information, as they are elastically scattered by crystalline samples. As a convergent beam interacts with a specimen, electrons will exhibit the behavior described by Bragg's law and scatter elastically with samples that are crystalline. A fraction of the electron beam will be elastically scattered in a wider angle, which allows their detection and formation of an image that contains the resulting pattern. Selected area electron diffraction (SAED) is the use of the selected area aperture in diffraction mode. That aperture can focus the beam to a specific region including larger or smaller areas of interest. The resulting diffracted beam is then detected using the CCD camera. Every spot present in the SAED pattern corresponds to a lattice plane of the same family of Miller indices ( $h, k, l$ ) of a crystal. As multiple crystals are included in the selected area aperture, as Figure 14(B) shows, multiple spots can be detected as they originate from the multiple orientations of a sample diffracting a coherent beam of electrons. For polycrystalline samples, the random orientation of the particles disposed in a given area will result in the formation of diffraction rings.

## Scanning Transmission Electron Microscopy

Scanning Transmission Electron Microscopy (STEM) mode uses a small probe that condenses the beam on a small spot and rasters the surface in order to generate an image. This technique still relies on transmission mode and it also allows

the construction of electron energy loss spectroscopy (EELS) and energy dispersive spectroscopy (EDS), which will be discussed in detail below. Bright field STEM (BFSTEM) uses the normal detection mode of transmitted electrons that reach the detector as the electron probe rasters the sample. A dark field STEM image can also be obtained by a high angle annular detector. High angle annular dark field (HAADF) imaging is created by elastically scattered electrons and therefore presents a high dependence on sample density and atomic number. Figure 14 shows an example of a combination of some of the modes of a transmission electron microscope presented so far. Figure 14(A) contains a HRTEM image of  $\text{Cu}_3\text{SbS}_4$  particle, which also presents electron interference patterns resulting from the interaction between the beam and the atomic planes of the (1 1 2) orientation. Figure 14(B) shows the SAED that was obtained from a group of particles shown in Figure 14(C), yielding a pattern that allows the estimation of the diffraction spacing ( $d_{hkl}$ ) that is characteristic of the crystalline phase being analyzed  $\text{Cu}_3\text{SbS}_4$ . In Figure 14(B), the spacings related to the crystallographic planes (2 1 1), (2 2 4), and (3 2 1) could be measured. Figure 14(C) contains an image obtained with STEM mode and the average diameter of multiple particles was estimated and used to generate a particle size distribution shown in Figure 14(D).

### Energy Dispersive Spectroscopy

Energy dispersive spectroscopy (EDS) detects characteristic X-rays from the material. As high energy electrons collide and transfer enough momentum to eject

electrons from the sample, core level holes are created. In addition the Auger process previously described, another possible relaxation mechanism occurs when a characteristic photon is emitted in conjunction with an electron from a higher energy orbital level filling the core hole. This photon is measured where characteristic X-ray energies are specific to the element.

EDS typically uses a silicon crystal detector that is ionized by incoming X-rays, yielding an electrical charge bias. The resultant voltage is a function of the X-rays' energy which allows the identification of different elements present in the sample. Figure 11 shows that the sampling volume of X-rays are significantly larger than the emitted electrons. Therefore, EDS yields 'bulk' information, from several microns in depth.

### Raman spectroscopy

Raman spectroscopy utilizes the excitation phenomenon of a sample by a known monochromatic source of light (laser). Most of incident light is elastically scattered (Rayleigh scattering) but a very small fraction of the original intensity ( $10^{-5}$  %) is inelastically scattered and that signal is amplified by a detector. Figure 15 shows a description of the working principle of Raman spectroscopy. The difference in wavelength between the detected radiation and the source provides information about how much energy was needed to excite vibrational levels of the sample. These are called "Raman shifts" and they are assigned to specific chemical bonds, which present different energy shifts as their vicinity changes. Therefore, this bulk

characterization technique can provide information about the presence of a certain chemical bond in a sample as well as its surrounding environment.

Different laser sources may be used as different samples may show more efficient absorption in visible range as opposed the infrared. Also, the difference in penetration depths of the employed radiation may give information about different regions of thicker samples.

#### Ultraviolet – Visible – Infrared spectroscopy

Ultraviolet-Visible-Infrared spectroscopy (UV-Vis-IR Spec.) uses the attenuation of light as it is transmitted through a sample. As a light source emits light of different wavelengths (200 – 1400 nm) onto a sample, the intensity that reaches the detector is a function of how much is absorbed by the sample. Figure 16 shows along with Equation 9, a representation of the change of intensity caused by an absorption coefficient. This correlation allows the determination of the absorption coefficient ( $\alpha$ ) given a light path (L) for different wavelengths.

$$T = \frac{I}{I_0} = e^{-\alpha(\lambda)L} \quad (9)$$

The absorption coefficient profile measured for different wavelengths of light allows an estimated value for the band gap. As photons provide energy that is

sufficient to excite electrons from the valence band to the conduction band (across the band gap), a steep increase in light absorption is observed. The band gap of a specific material can be estimated by the method developed by Tauc *et al.*,<sup>16</sup> which is based on the application of the Equation 10, where  $h$  is the Planck's constant,  $\nu$  is the radiation frequency,  $\alpha$  is the absorption coefficient, and  $E_g$  is the band gap of the material, and  $B$  is a proportionality constant. The value of the exponent “ $n$ ” characterizes the type of electronic transitions:  $n = 1/2$  for direct transitions  $n = 2$  for indirect transitions.

$$(h\nu \cdot \alpha)^{\frac{1}{n}} = B(h\nu - E_g) \quad (10)$$

### Dynamic Light Scattering

Dynamic light scattering (DLS) is a technique used to determine particle sizes of samples using light scattering and the natural Brownian motion of particles as they diffuse around in a dispersion. DLS focuses on the temporal fluctuation of the intensity of the scattered radiation, which is detected as a function of time and processed to provide a decay function that is related to the diffusion of particles in a liquid. The Einstein-Stokes model (Equation 11) is used to relate the average hydrodynamic radius of particles to the estimated diffusivity, where  $D$  is the diffusion coefficient,  $k_B$  is the Boltzmann constant,  $T$  is the temperature,  $\mu$  is the viscosity of the fluid, and  $R_H$  is the hydrodynamic radius.

$$D = \frac{k_B \cdot T}{6\pi \cdot \mu \cdot R_H} \quad (11)$$

DLS is a very robust technique that can provide measurements at ambient temperature without application of vacuum, however a careful analysis needs to be done considering several factors. The Einstein-Stokes model assumes that the shape of particles is spherical and each particle interacts with only the fluid, therefore a range of dilution is needed in order to avoid particle-particle interactions, which could form larger particles creating a different scattering pattern. Another common problem is the contribution from particles of different sizes in polydisperse samples. As particles of different size scatter the laser light differently, the final particle size distribution may contain results that are not representative of the sample.

### Thermogravimetric Analysis

In thermogravimetric analysis a sample is heated over a temperature range in a controlled environment (air, inert gas, reactive gas, etc.). The weight of the sample is tracked while increasing temperature, which yields information regarding the thermal behavior of the sample, (e.g. a gain in mass by oxidation, a loss in mass from water loss, pyrolysis, etc.). Attaching a mass spectrometer to the outlet of the heating zone may be advantageous, as it provides additional information by showing the mass

distribution of the gaseous desorption or reaction products that result from heating the sample in a given environment.

### Inductively Coupled Plasma Optical Emission Spectrometry

Inductively coupled plasma optical emission spectrometry (ICP-OES) or Atomic Emission Spectrometry (ICP-AES) uses a plasma to excite atoms present in a sample to produce an emission spectrum. Samples are either completely dissolved or digested in a mixture of acids so all elements present in a solid sample can become soluble in high purity water. That solution is then injected and nebulized into an inductively coupled argon plasma flame inside of the instrument. At high temperatures, the elements of the sample will be ionized and thermally excited to emit photons with characteristic energies. These photons are detected with an optical emission spectrometer. The experiment is usually repeated 3 or 5 times and the final intensity is compared to calibration curves obtained from solutions of known concentrations.

This technique allows a sensitive quantification of element concentration in a sample, requiring very small volumes and with very low detection limits (parts per billion). However, this technique requires low concentrations to avoid saturation of the optical spectrometer, which requires multiple dilutions during the sample preparation. Low sensitivity to certain elements and interference among elements are also known issues for this technique.

## Brunauer–Emmett–Teller isotherms

N<sub>2</sub> physisorption experiments are used to generate Brunauer–Emmett–Teller (BET) isotherms. A flask with a fixed volume and containing a sample of interest is filled with nitrogen gas. The flask is maintained in liquid nitrogen (77 K). The equilibrium pressure becomes a quantifying measurement of how much gas adsorbed to the surface of the material.

Brunauer *et al.* described five different types of isotherms that resulted from the different interactions between adsorbent and adsorbate.<sup>17</sup> Those different isotherms are shown in Figure 18. Type I represents an isotherm that follows the ideal model of Langmuir adsorption (monolayer of adsorbate on the surface) and it is typical of microporous materials. Type II is a common shape exhibited when N<sub>2</sub> is used with a porous material that exhibits some mesoporosity, since a plateau (Langmuir region) and a steep increase of adsorbed volume due to multilayer adsorption are present in this isotherm type. Type III shows mostly multilayer adsorption and absence of the Langmuir region (plateau) in the graph, which indicates weak interaction between adsorbate and adsorbent. Types II and III isotherms are related to materials that present macroporosity or nonporosity. Type IV is very similar to the type II but it presents a fast saturation level before the saturation pressure of N<sub>2</sub>, which is typically due to gas condensation inside of small (capillary) pores contained by the sample. Type V represents a combination of saturation of pores with weak interaction

between adsorbent and adsorbate. Type IV and V isotherms are characteristic of samples that present mesoporosity.

Besides information on porosity, the nitrogen physisorption experiment can also be used to determine the specific surface area of the material. The BET equation, Equation 12, was presented by Brunauer, Emmett and Teller in 1930. It is based on the BET model, which assumes a homogeneous surface, that there is no lateral interaction between molecules, that the top layer is at equilibrium with the vapor phase, and that the number of adsorbed layers of molecules becomes infinite at saturation pressure.  $P$  is the equilibrium pressure,  $P_0$  is the saturation pressure of nitrogen at 77 K,  $V_{ads}$  is the adsorbed volume of nitrogen which is estimated using the ideal gas law,  $V_m$  is the volume adsorbed for the region in which a monolayer of nitrogen is adsorbed to the sample, and  $C$  is the BET constant, which depends on the heats of adsorption and liquefaction of nitrogen (adsorbate).

$$\frac{1}{V_{ads}[(P_0/P) - 1]} = \frac{1}{V_m C} + \frac{C - 1}{V_m C} \left(\frac{P}{P_0}\right) \quad (12)$$

At the plateau region when a monolayer of nitrogen is adsorbed to the surface (Only isotherms of type I, II, and IV can be treated using this method), the Equation 12 can be fitted to the volume adsorbed data vs  $P/P_0$  and the parameter  $V_m$  can be determined. Equation 13 can be used for the determination of the BET surface area ( $S_{BET}$ ), where  $N$  is Avogadro's number,  $m$  is the mass of the solid sample, and  $\epsilon$  is the adsorption cross section of nitrogen.

$$S_{BET} = \frac{V_m \cdot N \cdot \varepsilon}{V \cdot m} \quad (13)$$

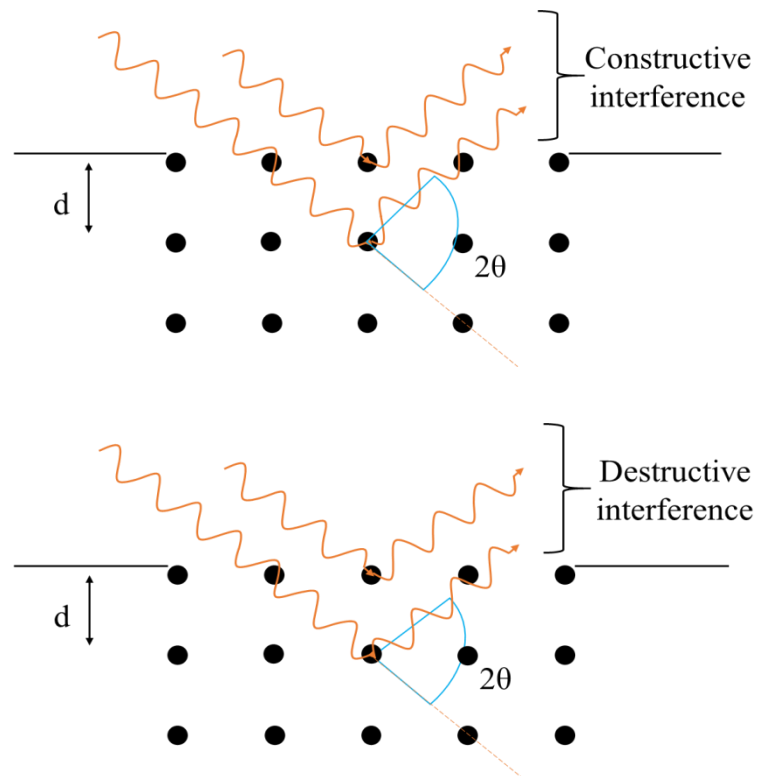


Figure 1: X-rays scattering from atoms of a crystalline sample.

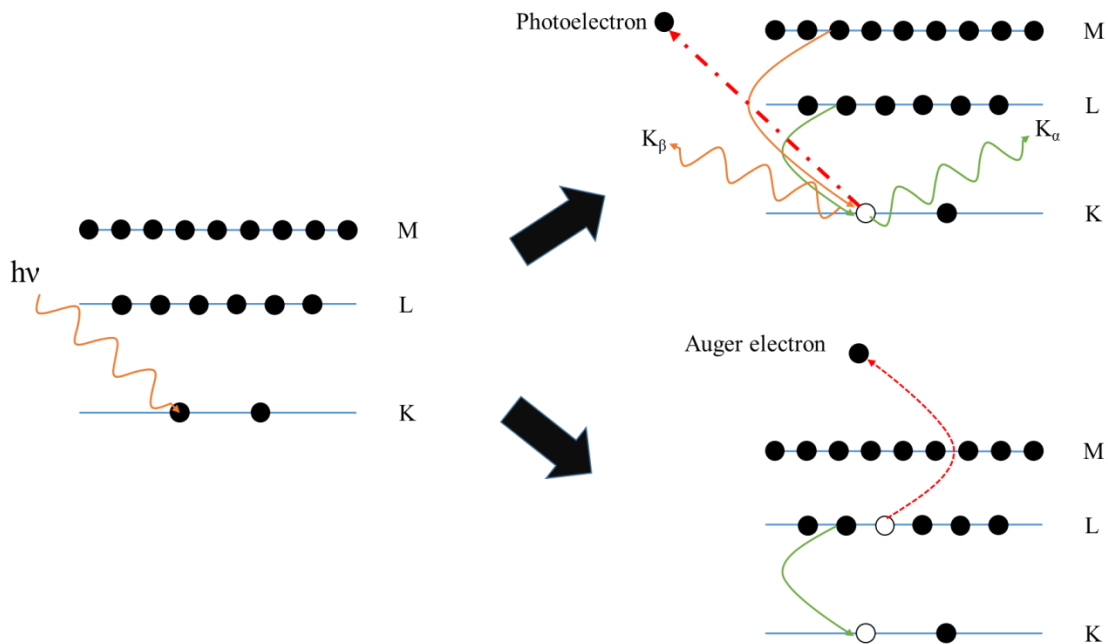


Figure 8: Simple schematic of fundamental phenomena that contribute to X-ray near edge structure spectra.

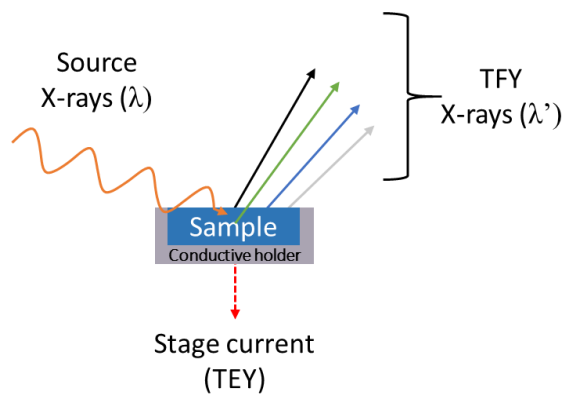


Figure 9: Detection modes of X-ray absorption near edge structure. TFY = Total fluorescence yield and TEY = Total electron yield.

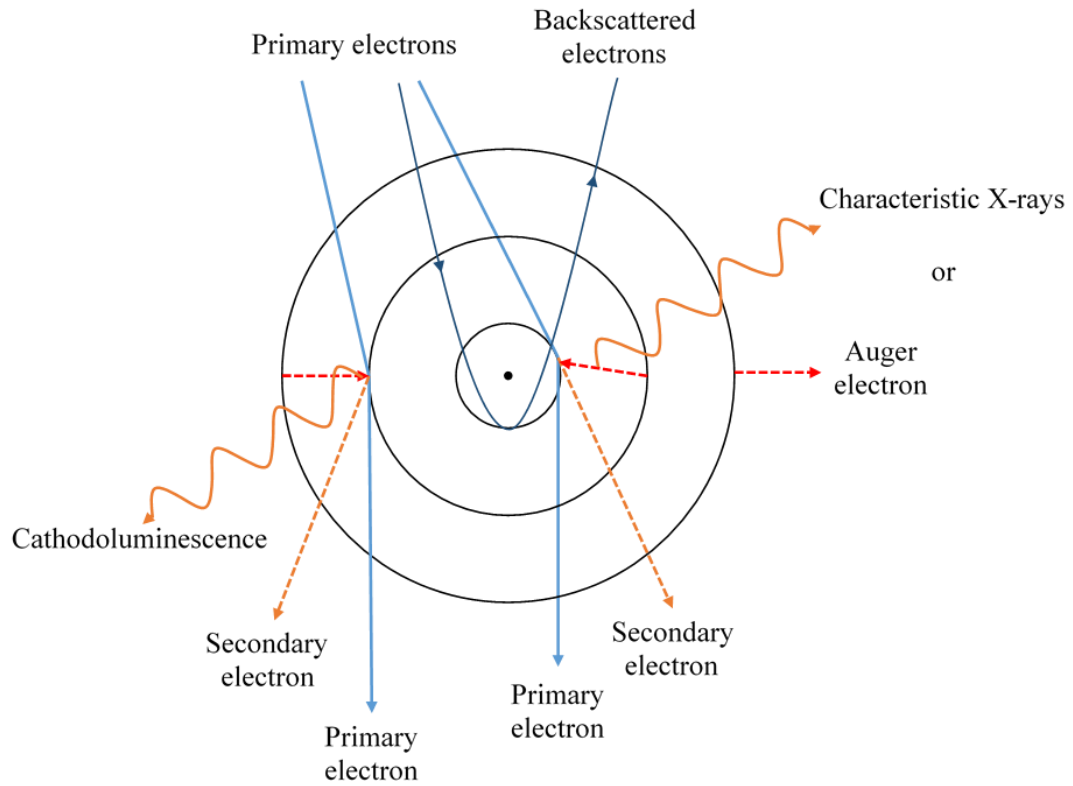


Figure 10: Different observed phenomena when the primary beam interacts with an atom generating secondary electrons (Inelastic scattering), backscattered electrons (elastic scattering), Auger electrons, and photons.

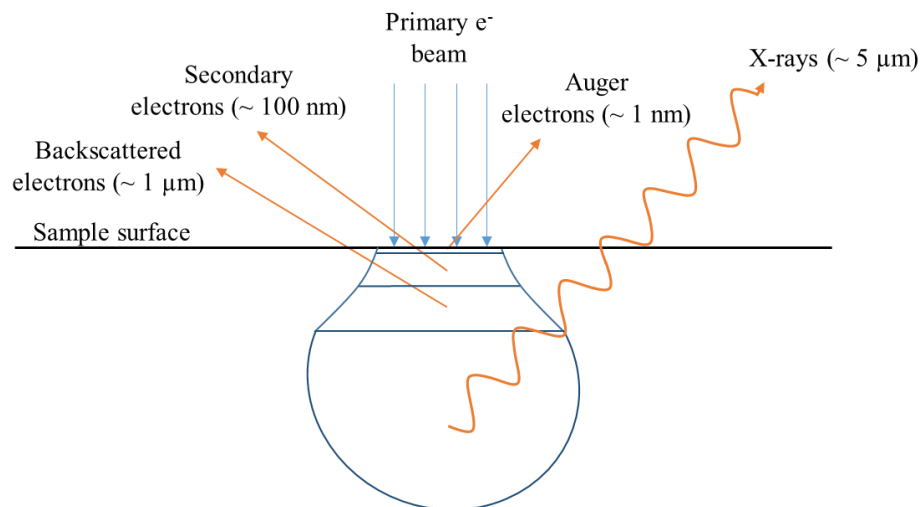


Figure 2: Sampling volume for each type of resulting emission due to the electron-sample interaction. The distances shown represent a rough estimation of the respective escape depths of each type of electron described and X-rays.

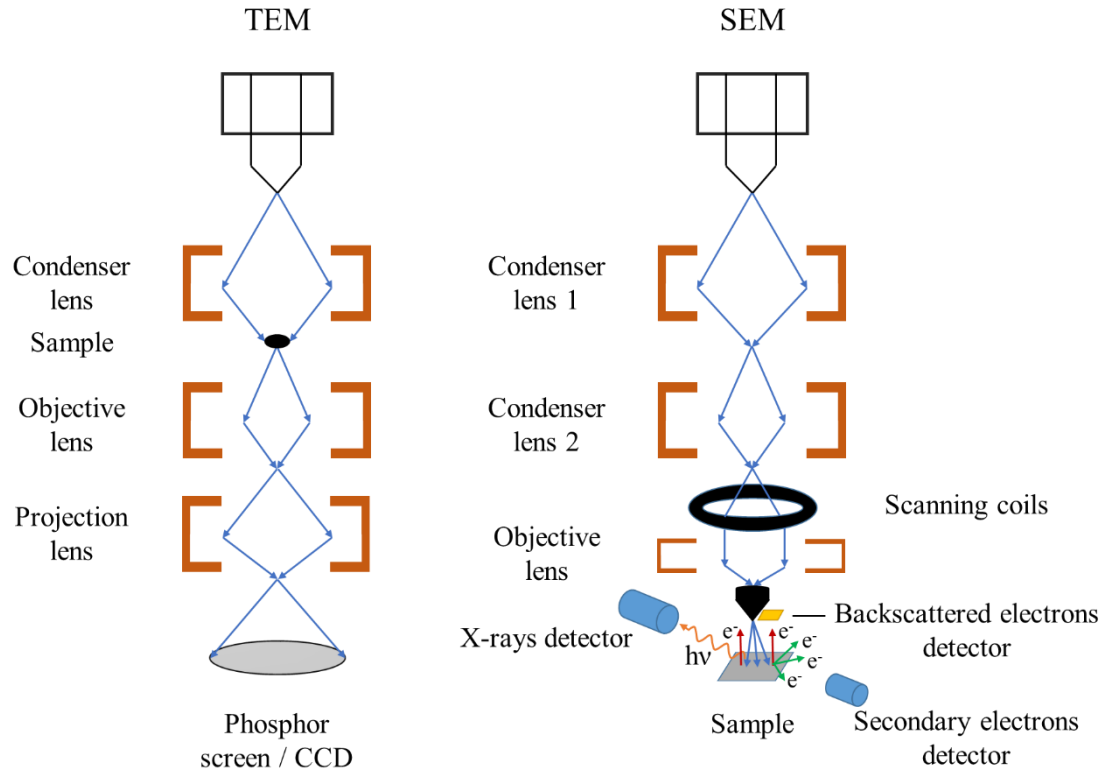


Figure 12: Scheme showing main parts of a transmission electron microscope (TEM) (Left) and a scanning electron microscope (SEM) (Right).

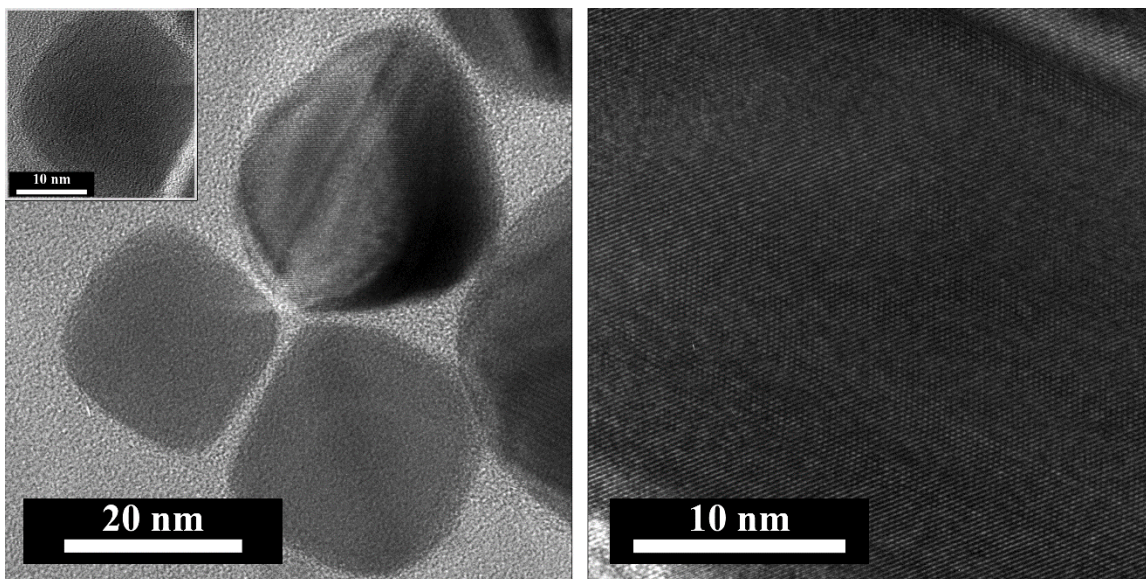


Figure 3: Bright Field Transmission Electron Microscopy (BFTEM) images of silver nanocubes. Left image shows cubes at lower magnification. Inset on the left and right image show silver nanocube in detail High Resolution Transmission Electron Microscopy mode (HRTEM).

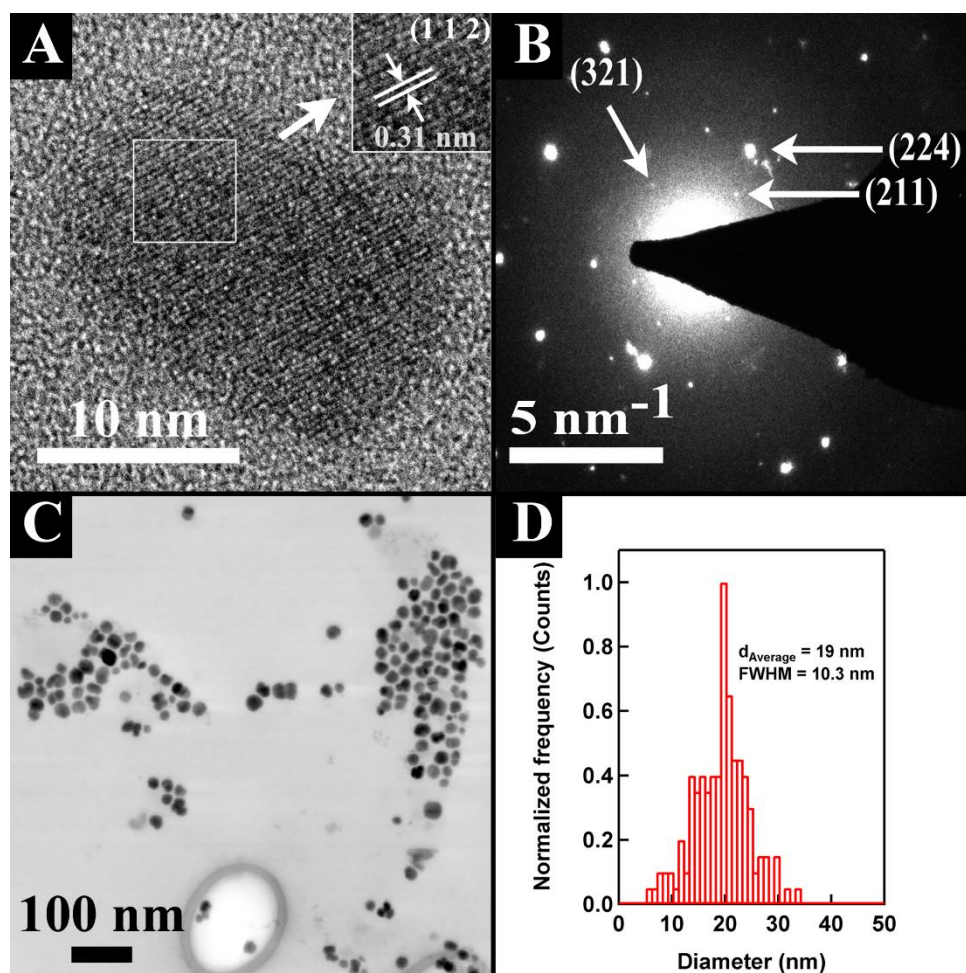


Figure 14: (A) HRTEM of single  $\text{Cu}_3\text{SbS}_4$  particle, (B) SAED of group of  $\text{Cu}_3\text{SbS}_4$  particles, (C) STEM image of as synthesized  $\text{Cu}_3\text{SbS}_4$  particles, and (D) Particle size distribution obtained using the STEM image shown in (C)

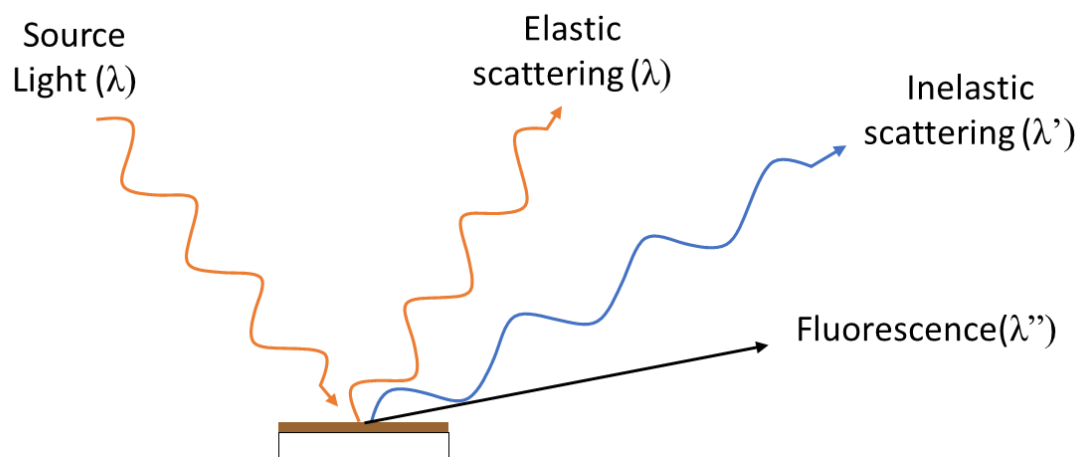


Figure 15: Fundamental phenomena that contribute to the detection of vibrational modes in Raman spectroscopy. The wavelengths shown in the figure represent the energy changes for each type of interaction.

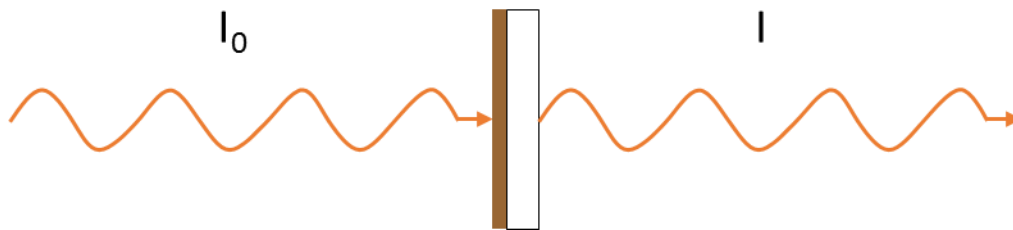


Figure 16: Radiation interaction with an absorbing sample. Phenomenon is basic mechanism of UV-Vis-IR spectroscopy.

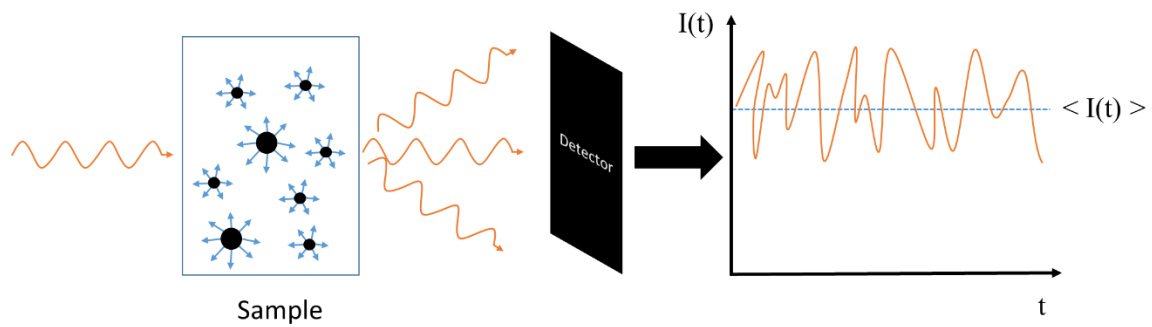


Figure 17: Representation of the elastic scattering phenomenon that occurs as a laser shines a dispersion of particles, which diffuse around in a liquid.

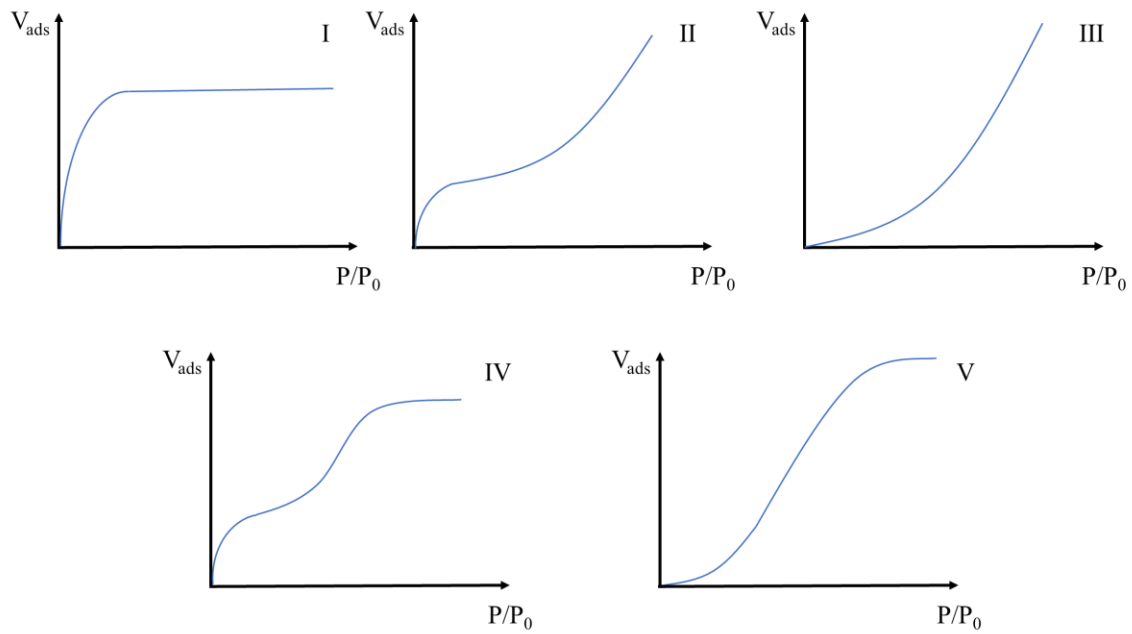


Figure 18: Types of isotherms presented by Brunauer *et al.*<sup>17</sup>

## CHAPTER 3

SEGMENTED FLOW MICROWAVE-ASSISTED SYNTHESIS OF  
SILVER NANOCUBES

Gustavo H. Albuquerque, and Gregory S. Herman\*

Oregon State University, School of Chemical, Biological, and Environmental  
Engineering, Corvallis, Oregon, 97331-2702, USA

\* Corresponding author

Manuscript in preparation

## Abstract

The synthesis of Ag nanocubes with sharp corners and edges has been demonstrated, where nucleation is increased through sulfide formation, and introduction of a regulator enhanced the shape of the cubes. Ag nanocubes have applications in highly sensitive sensors due to surface enhanced Raman scattering effects. The reported synthetic approaches have good control over size and shape, however they have difficulties in scaling to larger volumes. In this study, a segmented flow microwave-assisted reactor was used to separate the nucleation from the growth events, which allows the synthesis of very uniform Ag nanocubes. This approach is scalable to produce large, uniform volume of Ag nanocubes. Transmission electron microscopy images and optical properties were used to optimize the reaction conditions and Ag nanocubes of sizes between 28 to 58 nm were synthesized with a narrow particle size distribution and high selectivities (> 70 %). These results allow the preparation of films containing silver nanoparticles, which can be used for sensing devices.

## Introduction

In the synthesis of nanoparticles, fine control over particle size, shape, and composition is of scientific and industrial interest because of their strong correlation with optical, electronic, physical, and chemical properties of the final products.<sup>18,19,20,21</sup> Silver nanoparticles have been widely studied due to their exceptional morphology dependent properties, which allow impressive performance in applications including plasmonics, catalysis, and sensing via surface enhanced Raman scattering (SERS). These characteristics make silver nanoparticles suitable to studies involving facet-selective catalysis,<sup>22,23</sup> high sensitivity sensing devices,<sup>21,24</sup> and light trapping in photovoltaics.<sup>25</sup>

The use of silver nanocubes in sensing devices has shown excellent results when compared to silver nanoparticles with random shapes or spherical.<sup>26</sup> These results indicate that oriented particles with truncated crystallographic facets exposing sets of (1 0 0) planes, can have charge accumulation on their sharp edges. This enhances the Raman signal, which can significantly increase the detection sensitivity of a given species.<sup>27</sup>

There has been a very rapid development of approaches that are used to synthesize silver nanoparticles with well-controlled shapes for a wide ranges of particle sizes. The application of different silver precursors, reducing agents, solvents, and dispersants have been changed in order to achieve smaller particles with high uniformity and shape selectivity.<sup>28,29,30,31,32</sup> However, most of these approaches only allow the synthesis of small volumes of nanocrystals, with limited scalability.

Microwave radiation has been effective in the synthesis of nanoparticles, where microwave radiation can rapidly and uniformly heat reactants to high temperatures which allows fast nucleation rates, shortens reaction times, and increases conversion rates. The combination of microwave heating with continuous flow approaches can provide improved scalability and high uniformity for the synthesis of nanomaterials.<sup>33</sup> For example, continuous flow microwave-assisted methods have been used in the synthesis of a range of nanomaterials.<sup>34,35,36,37,38</sup> where this approach has demonstrated improvements in reagent utilization, a significant reduction in reaction times, and a decrease in particle size distributions.

In this study, a segmented flow microwave-assisted was used to synthesize silver nanocubes. We have evaluated how each operating parameter changed the particle size and shapes. Optimization of the synthetic parameters led to the development of several approaches to produce nanocubes with different sizes with high selectivity.

## Experimental Section

**Chemicals:** Silver trifluoroacetate ( $\text{CF}_3\text{COOAg} \geq 99.9\%$ ), Poly(vinylpyrrolidone) (PVP of  $\text{MW} \approx 55000$ ), and sodium hydrosulfide hydrate ( $> 66.7\%$ ) were obtained from Sigma-Aldrich. Sodium chloride (99.0%) and sodium bromide (99.0%) were obtained from EMD Millipore. Ethylene glycol was obtained from Macron Fine Chemicals ( $> 99.0\%$  - Batch 0000132351) as well as methanol, acetone, and isopropanol (ACS grade). All chemicals were used as received except

for ethylene glycol. The ethylene glycol used in the synthesis was heated over 3 hours prior to the reaction in an open flask and cooled in an ice bath right before the preparation of reagents. Silver precursors and the sodium hydrosulfide were stored in an N<sub>2</sub>-filled glove box that maintained oxygen and moisture concentrations below 0.5 ppm. Sodium chloride and sodium bromide were stored in a desiccator.

**Synthesis:** The synthetic method reported here is a modification of the synthesis presented elsewhere.<sup>32</sup> Two solutions containing reagents were prepared separately before being used in the continuous flow reactor. In a typical synthesis, the flask 1 contained either 282, 423, or 846 mM of silver trifluoroacetate in 20 mL of ethylene glycol. Flask 2 had reagents mixed in the following order: First 6.25 mL of a solution containing 20 mg/mL of dissolved PVP were mixed with 2.5 mL of a 3 mM solution of NaCl in ethylene glycol. Ethylene glycol was added to the solution until the volume was 19.7 mL. A 0.3 mL solution containing 3.5 mM of NaHS was added to the solution just prior to the start of the reaction. Both flasks were pumped into two PEEK “Y” mixers in series. The first “Y” mixer was used to mix the two precursor solutions and the following mixer was used to inject argon gas into the line creating a segmented flow regime right before the reactor using the same peristaltic pump. The reaction setup had two main parts. The first part was a microwave reactor from Sairem (Model PCCMWR340PVMR1PE GMP 30 K; 2.45 GHz; 3 kW) where the microwave zone temperature ( $T_{MW}$ ) was monitored using an infrared camera (FLIR model E40). The total irradiated length was 4.7 cm and the volumetric flowrate was set at  $\sim 3.8 \text{ mL}\cdot\text{min}^{-1}$ , which resulted in a microwave zone residence time of  $\sim 1.5$  seconds (Teflon<sup>®</sup> tubing – I.D. = 1/16 inch). The second part of the reaction setup is

the growth zone, which consisted of a coil of the same tubing submerged in an oil bath held at 135 °C. The tubing had different lengths, which gave different growth bath residence times ( $\tau_{GB}$ ). Coils of tubing with lengths of 23 m, 15 m, and 8 m were used which gave an average growth bath residence times of 12, 8, and 4 minutes, respectively. After the growth bath, the reaction liquor flowed through a 1 m long coil that was placed inside an ice bath after which the products were collected. Each solution received approximately 12.5 mg of PVP per mL of liquor dispersion. For reactions followed by a sodium bromide bath, 5 mL reaction liquor was added to a 50 mL flask containing 20 mL of 0.375 mM NaBr in ethylene glycol at 135 °C. The NaBr solution was heated for 45 minutes before the injection of products liquor. After the desired batch reaction time the product was collected.

**Post-synthesis purification steps:** The reaction liquor was centrifuged twice at 4500 rpm for 15 minutes. After the first centrifuge step, the supernatant was collected and precipitated at 8000 rpm/10 min after the addition of twice as much acetone. Acetone was used to precipitate particles and remove excess PVP. 18 M $\Omega$  water was used to disperse particles and remove any remaining salts, ethylene glycol, and PVP. Particles were precipitated at 14500 rpm/15 min. This last step was repeated once before dissolving particles in ethanol for storage or isopropanol for the film deposition.

**Characterization:** X-ray diffraction (XRD) was performed using a Rigaku Ultima IV diffractometer ( $\lambda_{Cu-K\alpha} = 0.1542$  nm, 40 kV, 40 mA) on films formed from the cleaned silver nanoparticles. To form films a dispersion of silver nanoparticles in isopropanol was drop-cast onto glass slides and the solvents were evaporated in a N<sub>2</sub>

environment prior to performing XRD. The analysis was performed using a fixed incidence angle for the X-rays ( $\omega = 1.5^\circ$ ). Absorbance measurements were obtained using an UV-Vis spectrophotometer (Thermo Scientific Evolution 220).

Measurements were performed from solutions containing five droplets of the reaction liquor in deionized water without any purification steps. Transmission electron microscopy (TEM) and scanning electron microscopy (SEM) images were taken using a FEI Titan FEG with acceleration voltage at 200 kV and a FEI Quanta 600 FEG SEM with 20-30 kV accelerating voltage, respectively. For TEM imaging, samples were prepared from an ethanol dispersion of silver nanoparticles, which was sonicated for 2 minutes prior to preparation (Branson model 2510 – Max power 130 W). The solution was then drop-cast onto a carbon coated copper grid, which was mounted in the microscope after drying for 5 minutes at 60°C.

## Results and Discussion

**Concentration effects.** Figure 19 shows the effect that different concentrations of silver trifluoroacetate has on the synthesis of silver nanoparticles. For these experiments,  $T_{MW}$  was set at 185 °C and  $\tau_{GB}$  was fixed at 12 minutes. As Figure 19 (A-C) show, the size and shape of the Ag nanoparticles are strongly influenced by the initial concentration of silver trifluoroacetate. When the 282 mM of silver trifluoroacetate was used, spheres with an average diameter of  $\sim 7 \pm 1$  nm were formed (determined by TEM). Increasing the concentrations to 423 and 846 mM resulted in cubes with edge lengths of  $\sim 43 \pm 5$  nm and  $\sim 60 \pm 6$  nm, respectively. As

Figure 19(D) shows, the increase in particle size led to a shift in the absorbance peaks for each of the samples. These peaks were centered at 394, 440, and 469 nm for 282, 423, and 846 mM silver trifluoroacetate concentrations, respectively. The increase in particle size also yielded the formation of cubes with sharp features, which has been previously associated to a characteristic UV-Vis feature that appears at ~360 nm.<sup>32</sup> The presence of absorbance peaks is not only related to absorption but also to light scattering. For example, absorbance peaks located between 400 and 700 nm are related to light scattering effects which are strongly correlated to particle size. However, peaks located between 320 to 420 nm are due to resonances that are associated with the cubic shape of the particles.<sup>39</sup> A shoulder located at higher wavelengths (500-550 nm) were also observed for each of the samples synthesized at higher concentrations (423 mM and 846 mM), which were previously correlated to the formation of larger or agglomerated particles.<sup>29,40</sup> For the concentrations 423 mM and 846 mM there were peaks located at 386 and 390 nm, respectively, which also indicate the formation of cubic particles.

The most intense peaks in the UV-Vis spectra had differences in peak broadening. As the scattering of light is a function of particle volume, the broadness of the peak located in the 400-700 nm range is related to particle size distributions in a given sample. The Ag nanocubes synthesized at 423 mM had the narrowest peaks, and was used to further optimize the Ag nanocube size uniformity.

**T<sub>MW</sub> effects.** To evaluate the role of nucleation effects we have used three different microwave zone temperature (i.e., 135 °C, 155, and 185 °C). These effects were investigated for a fixed silver trifluoroacetate concentration of 423 mM, and

only the MW zone was used for these reactions. Under these conditions only spherical particles were obtained based on TEM analysis. However, the UV-Vis spectra in Figure 20 shows that  $T_{MW}$  has a significant impact on the full width at the half maximum (FWHM) of the main absorbance peaks when only using the MW reactor. The increase in FWHM of the UV-Vis spectra is related to an increase in particle size distributions, since the formation of larger or smaller particles results in shifts in the absorbance spectra. Increasing  $T_{MW}$  resulted in a blue shift and narrowing of the UV-Vis peak, which indicates the formation of smaller particles with a narrower size distributions. This may be due to the higher nucleation rates at higher  $T_{MW}$ , which results in faster reaction kinetics and the formation of more nuclei resulting in higher particle uniformity.

To characterize the role of  $T_{MW}$ , experiments were performed with the growth bath with a fixed concentration of silver trifluoroacetate at 423 mM and a  $\tau_{GB} = 12$  min. Figure 21(A-D) show that at higher  $T_{MW}$ , a small decrease of particle size can be observed along with a reduction in FWHM of the UV-Vis spectra. Diameters and edge lengths were measured from TEM images for particles with rounded features (with initial edge formation) and cubic particles, respectively. The values for characteristic lengths ( $d_{TEM}$ ) were  $44.4 \pm 7.6$ ,  $43.2 \pm 5.6$ , and  $42.6 \pm 5.2$  nm when using  $T_{MW} = 135$ , 155, and 185 °C, respectively. The observed changes in  $d_{TEM}$  after the addition of the growth bath are not significantly different due to the variation observed in each measurement. In Figure 21(A), a shoulder with higher intensities can be seen at ~ 515 nm specially when  $T_{MW} = 135$  °C is applied and a small reduction of the UV-Vis FWHM for the  $T_{MW} = 185$  °C is observed.

In regards to particle shape, changes in  $T_{MW}$  caused a small change in particle size, but sharper cubic shapes are seen for higher  $T_{MW}$ . The features at  $\sim 360$  nm and  $\sim 400$  nm in the UV-Vis spectra only appear with higher intensities for higher  $T_{MW}$ , which is consistent with the TEM results.

**$\tau_{GB}$  effects.** To evaluate the role of the growth bath we have used three different residence times in the growth bath ( $\tau_{GB}$ ) (i.e., 4, 8 and 12 minutes), for three  $T_{MW}$ , while using 423 mM of silver trifluoroacetate. Figure 22(A-C) show UV-Vis spectra for all the different  $\tau_{GB}$  and each  $T_{MW}$  used. There was a distinct red shift of the UV-Vis peaks with longer  $\tau_{GB}$ , as well as an increase in their FWHM. Figure 22(D) shows TEM results, which indicate an increase in  $d_{TEM}$  for longer residence times. For the same  $\tau_{GB}$ , a consistent decrease in the  $d_{TEM}$  was observed as different  $T_{MW}$  were used but the standard deviation of  $d_{TEM}$  also shown in Figure 22(D) makes this difference negligible. TEM also showed no change in shape until  $\tau_{GB} = 12$  min, where only spherical particles were obtained for  $\tau_{GB} \leq 8$  min.

**Synthesis of nanocubes of edge lengths < 30 nm.** To synthesize smaller Ag nanocubes we used lower silver trifluoroacetate concentrations (282 mM) and a growth bath ( $\tau_{GB} = 12$  min). We also added a sodium bromide bath at the end of the process. Figure 23(A) shows that different  $T_{MW}$  results in a shift of the UV-Vis spectra towards shorter wavelengths, which we also observed for the 423 mM silver trifluoroacetate precursor.

Lower  $T_{MW}$  resulted in an increase in particle size and an increase in UV-Vis FWHM as shown in Figure 23(A). Post-treatment of the Ag particles was performed using a sodium bromide bath after the continuous flow process. Figure 23(B) shows a

TEM image of the synthesized particles after 20 minutes in the sodium bromide batch. Before the sodium bromide, the Ag particle size was  $7 \pm 1$  nm, as shown in Figure 19(A). After 20 minutes in the sodium bromide batch, Ag nanocubes had a  $28 \pm 4$  nm edge length. The increase in Ag particle size, and formation of Ag nanocubes with flat edges, resulted in a red shift in the absorbance peaks, as well as the appearance of the two features at  $\sim 360$  nm in the UV-Vis spectra.

High-resolution TEM images are shown in Figure 23(C), where a d-spacing of 0.20 nm was obtained from the image, which corresponds to the (0 2 0) facet of the silver nanocube. Figure 23(D) shows the selected-area electron diffraction (SAED) pattern obtained from the single particle shown in Figure 23(C). The d-spacings 0.210, 0.143, 0.110, and 0.091 nm could be measured, which characterize the atomic planes of orientation (2 0 0), (2 2 0), (0 -4 0), and (4 2 0), respectively. These results confirm the formation of a single crystal silver nanocube.

Figure 24 shows XRD data for Ag nanocubes synthesized with  $T_{MW} = 185$  °C,  $\tau_{GB} = 12$  min, and 20 min of NaBr batch, and a  $d_{TEM} \sim 28$  nm. XRD was used to confirm the formation of pure elemental silver nanoparticles, and the absence of impurities such as silver chloride and silver bromide. Diffraction peaks located at  $2\theta = 38.2, 44.4,$  and  $64.6^\circ$  are due to diffraction from the (1 1 1), (2 0 0), and (2 2 0) crystallographic planes, respectively, and these peak positions are characteristic of metallic silver. No peaks for silver chloride, silver bromide, or other impurities were detected.

**Selectivity results for each synthetic route that resulted in cubes.** In these experiments we developed three different routes for the synthesis of silver nanocubes

with sizes ranging from ~ 28 to 58 nm. An analysis of the selectivity for Ag nanocube size and structure was performed to evaluate each synthetic approach. Figure 25(A) shows the  $d_{\text{TEM}}$  for the silver nanocubes and the selectivity to silver nanocubes for each synthetic process. For this analysis we compared different silver trifluoroacetate concentrations and the addition of a 20 minutes sodium bromide batch process for Ag nanocubes synthesized with 282 mM silver trifluoroacetate. Higher silver trifluoroacetate concentrations resulted in an increase in the average size of the Ag nanoparticles, while the formation of larger particles resulted in a decrease in the selectivity to the formation of nanocubes. Selectivities for the formation of Ag nanocubes were 78, 75, and 40 % as the silver trifluoroacetate concentrations were increased from 282 (including the bromide batch), 423, and 846 mM, respectively.

Although  $T_{\text{MW}}$  had a noticeable effect on the absorbance spectra for samples synthesized only using the microwave zone (Figure 20), Figure 25(B) shows that  $T_{\text{MW}}$  had little influence on the final particle size after the growth bath. However, we found that selectivities were significantly improved (~ 73.3 and 75.0 %) for the highest  $T_{\text{MW}}$  (155 and 185 °C), respectively.

A wide variety of synthetic procedures have been developed showing silver nanocubes of high purity with sizes varying from 15 – 60 nm. Synthetic approaches included the use of water as the only solvent<sup>41</sup>, different glycols as solvents<sup>42</sup>, the addition of sodium hydrosulfide<sup>40</sup>, the use of bromide ions as capping agents<sup>32</sup>, which reduced reaction times and yielded nanocubes with high selectivity. These approaches produced excellent results, however they produce small volumes and rely on batch reactors, which present scalability issues.

The approach presented in this work showed the synthesis of Ag nanocubes with  $d_{\text{TEM}} \sim 28$  and  $\sim 44$  nm, a narrow particle size distribution, and cube selectivities above 70 %, suggesting that segmented flow microwave-assisted reactors can effectively control the size and shape for scalable nanomaterials synthesis.

## Conclusions

In summary, we have developed a scalable approach for the synthesis of silver nanocubes with high cube selectivities. Three different processes were developed which resulted in Ag nanocubes with  $d_{\text{TEM}} = 28, 45,$  and  $58$  nm. The optimization of the reaction parameters ( $T_{\text{MW}}, \tau_{\text{GB}},$  and silver precursor concentrations) led to the formation of highly selective cubic shapes ( $> 70$  %) and narrow size distributions. These results indicated that smaller particles were formed as higher  $T_{\text{MW}}$  were used, which illustrates that microwaves induced faster nucleation rates. This was confirmed due to narrowing and blue-shift of the UV-Vis absorption spectra. Residence time dependence in the growth bath indicated that there was an increase in Ag particle sizes as longer reactions were performed, however Ag nanocubes only formed after  $\tau_{\text{GB}} = 12$  minutes. Silver trifluoroacetate concentrations had the largest impact on particle sizes for the Ag nanocubes. Larger concentrations yield a larger amount of nuclei but it also can result in higher growth rates resulting in the formation of larger particles over the course of the reaction.

## Acknowledgments

This research was funded by the United States National Science Foundation – Scalable Nanomanufacturing program (Grant CBET-1449383). A portion of this research was performed at the Northwest Nanotechnology Infrastructure, a member of the National Nanotechnology Coordinated Infrastructure, which is supported by the National Science Foundation (Grant ECCS-1542101). This material is also based upon work also supported by the National Science Foundation via the Major Research Instrumentation (MRI) program under Grant No. 1040588. We also acknowledge the Murdock Charitable Trust and the Oregon Nanoscience and Microtechnologies Institute (ONAMI) for their financial contributions towards the OSU Titan TEM. The authors also acknowledge the suggestions of Aleksey Ruditskiy who kindly provided details of his experimental work with Professor Xia.

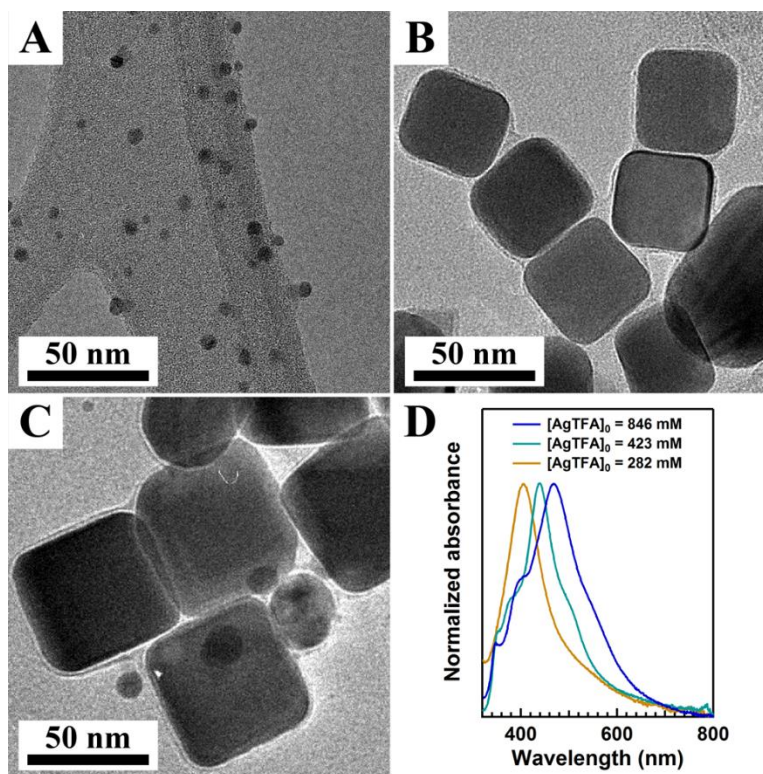


Figure 19: TEM images of particles synthesized at  $T_{MW} = 185\text{ }^{\circ}\text{C}$   $\tau_{GB} = 12\text{ min}$  using different concentrations of silver trifluoroacetate: (A) 282 mM, (B) 423 mM, and (C) 846 mM. (D) UV-Vis spectra for the solutions of the as-synthesized particles from each concentration used.

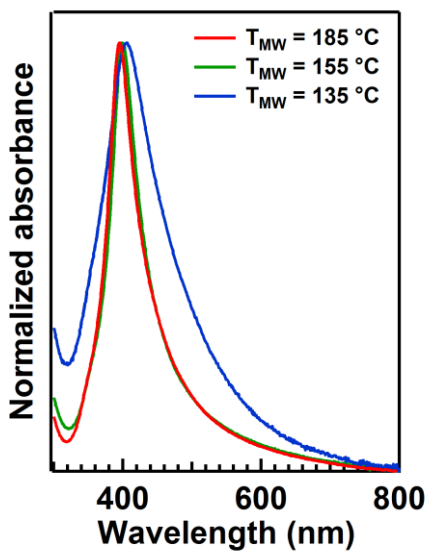


Figure 20: UV-Vis spectra of samples synthesized using the microwave zone only with different  $T_{MW}$  being set for a fixed concentration of silver trifluoroacetate at 423 mM.

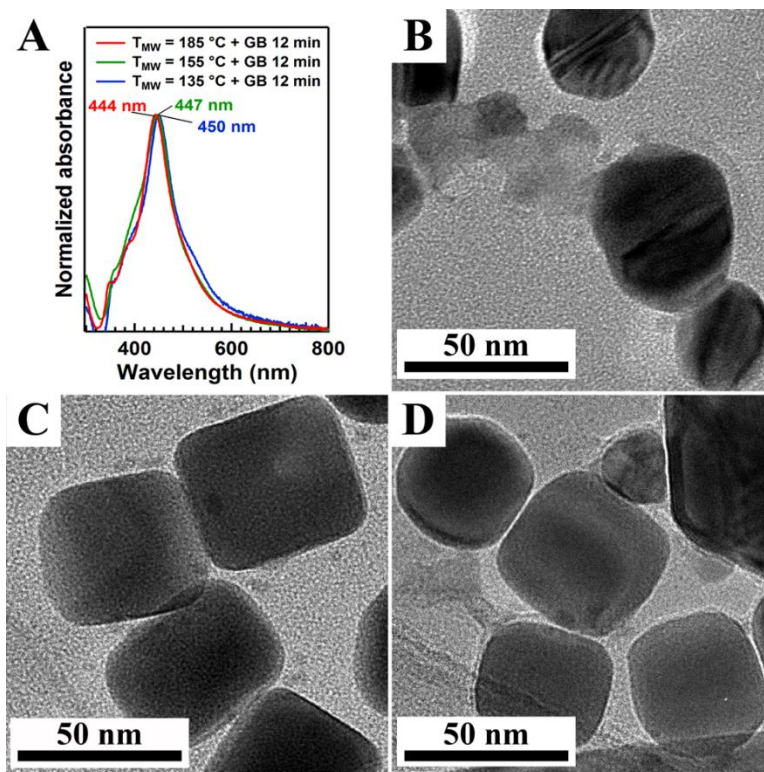


Figure 21: (A) UV-Vis spectra for the silver nanoparticles synthesized at different  $T_{MW}$  and the addition of the growth bath with  $\tau_{GB} = 12$  min. The concentration of silver trifluoroacetate was fixed at 423 mM. TEM images show products obtained under those conditions for the respective  $T_{MW}$ : (B)  $T_{MW} = 135\text{ }^{\circ}\text{C}$ , (C)  $T_{MW} = 155\text{ }^{\circ}\text{C}$ , and (D)  $T_{MW} = 185\text{ }^{\circ}\text{C}$ .

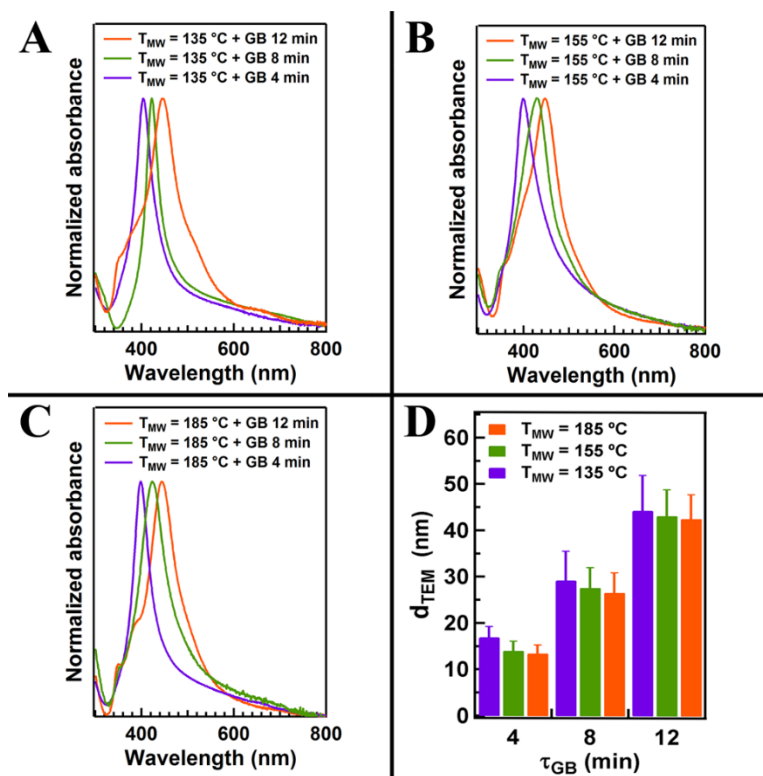


Figure 22: UV-Vis spectra of silver nanoparticles synthesized using different growth bath residence times ( $\tau_{GB}$ ) and different microwave temperatures ( $T_{MW}$ ) for 423 mM of silver trifluoroacetate.

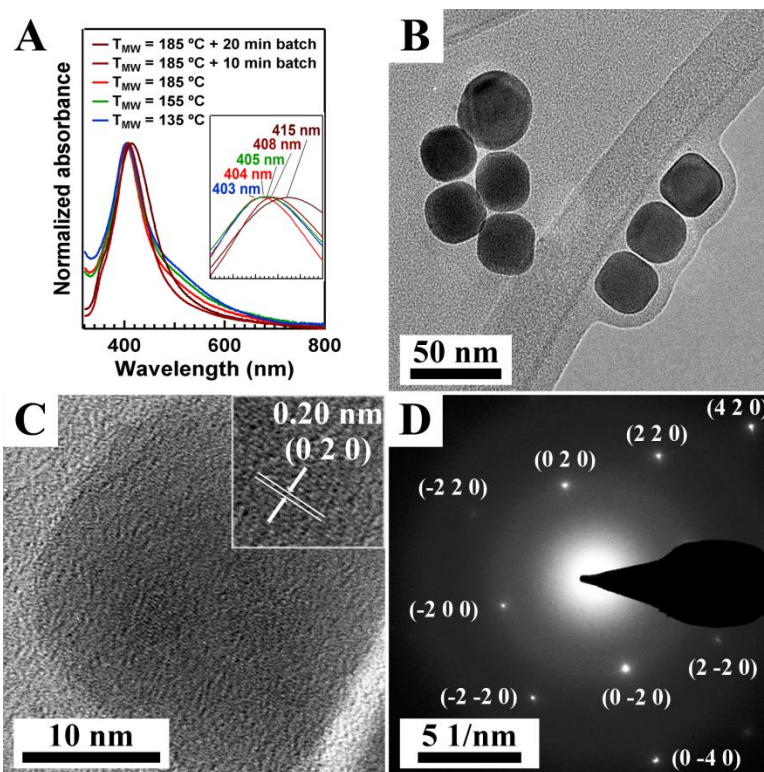


Figure 23: (A) UV-Vis spectra of samples synthesized with 282 mM of silver trifluoroacetate with different  $T_{MW}$  being used and with a  $\tau_{GB} = 12$  min. For the  $T_{MW} = 185$  °C, samples had an additional batch growth containing NaBr which are also included in (A). (B) TEM image of nanocubes synthesized using  $T_{MW} = 185$  °C and 20 min of NaBr batch. (C) HRTEM image of a single nanocube, and (D) SAED of single crystal cube shown in (C).

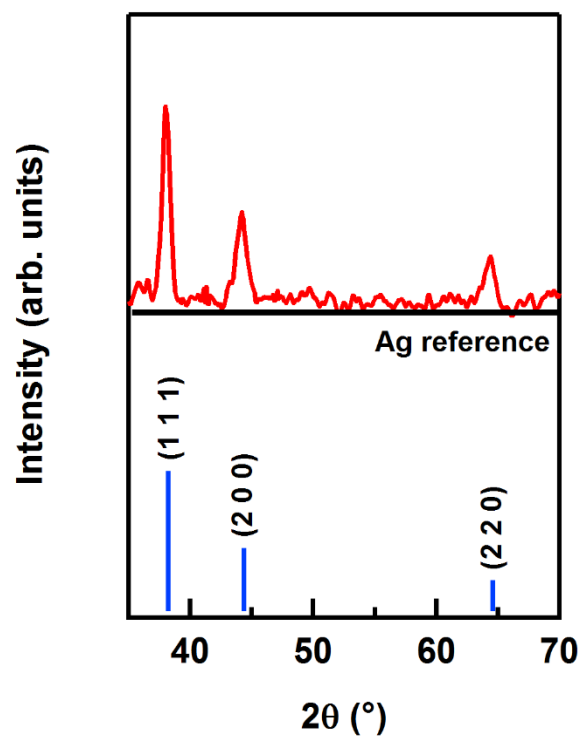


Figure 24: X-ray diffraction of film of silver nanocubes shown in Figure 23(B).

Reference pattern was taken from the RUFF open database (RRUFF ID: R070463).

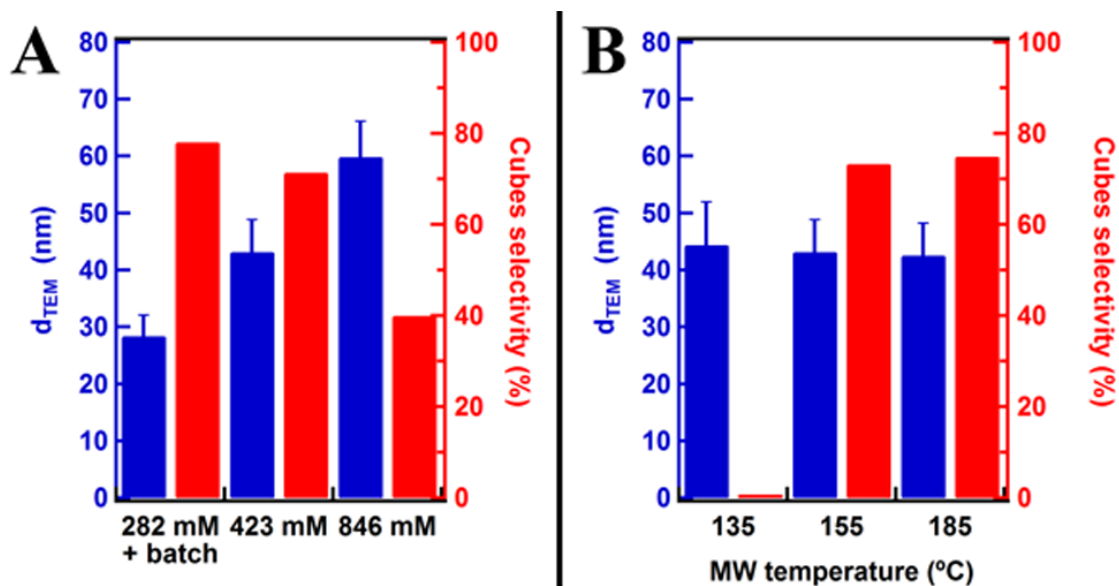


Figure 25: Selectivity and TEM average diameter or edge length for cuboctahedra and cubes, respectively were summarized. (A) Average edge lengths for the three routes ( $T_{MW} = 185$  °C,  $\tau_{GB} = 12$  min/Different silver trifluoroacetate concentrations) to synthesize ~ 28, 42, and 58 nm silver nanocubes. (B) Average edge length/diameter and selectivity for different  $T_{MW}$ 's,  $\tau_{GB} = 12$  min, and silver trifluoroacetate concentration = 423 mM.

## CHAPTER 4

GAS-LIQUID SEGMENTED FLOW MICROWAVE-ASSISTED  
SYNTHESIS OF MOF-74(Ni) UNDER MODERATE PRESSURES

Gustavo H. Albuquerque,<sup>1</sup> Robert C. Fitzmorris,<sup>1</sup> Majid Ahmadi,<sup>1</sup> Nick  
Wannenmacher,<sup>1</sup> Praveen K. Thallapally,<sup>2</sup> B. Peter McGrail,<sup>2</sup> and Gregory S.  
Herman<sup>1,\*</sup>

<sup>1</sup>Oregon State University, School of Chemical, Biological and Environmental Engineering,  
Corvallis, OR 97331-2702, USA

<sup>2</sup>Pacific Northwest National Laboratory, MSIN K4-18, Richland, WA 99352, USA

\*Corresponding Author

Reproduced from Cryst. Eng. Comm., vol. 17, issue 29, pp. 5502-5510, 2015

with permission from the Royal Society of Chemistry

## Abstract

The metal organic framework, MOF-74(Ni), was synthesized in a continuous flow microwave-assisted reactor obtaining high space-time yield ( $\sim 90 \text{ g}\cdot\text{h}^{-1}\cdot\text{L}^{-1}$ ) and 96.5 % conversion of reagents. Separation of nucleation and growth steps was performed by using uniform and rapid microwave heating to induce nucleation, which allowed a substantial increase in conversion for shorter reaction times under mild pressure. High yields were achieved in minutes, as opposed to days for typical batch syntheses, with excellent control over material properties due to more uniform nucleation, and separation of the nucleation and growth steps. Optimization of microwave reactor parameters led to improvements in MOF-74(Ni) crystallinity, reagent conversion, and production rates. Differences in MOF-74(Ni) crystallinity were observed as smaller grains were formed when higher microwave zone temperatures were used. Crystallinity differences led to different final adsorption properties and surface areas. Herein we show that a continuous high space-time yield synthesis of MOF-74(Ni) allows control over nucleation using microwave heating.

## Introduction

Metal organic frameworks (MOFs) are of considerable scientific and technological interest due to their tunable porosity, high surface area, and the large number of available structures.<sup>43,44,45</sup> Metal ions coordinated with a wide variety of polytopic linkers (bridging ligands) form a crystalline nanoporous structure which provides advantages for applications including gas storage,<sup>46,47,48,49,50,51,52</sup> gas separation,<sup>53,54,55,56,57,58,59,60,61,62</sup> catalysis,<sup>63,64</sup> sensing,<sup>65,66,67</sup> and more recently pharmaceuticals.<sup>68,69</sup> The MOF-74 series, also known as CPO-27, (CPO = Coordination Polymer of Oslo) have high adsorption properties for carbon dioxide,<sup>54,57,58,59,70</sup> noble gases,<sup>60,61</sup> toxic gases,<sup>53,55</sup> methane,<sup>71</sup> and water.<sup>54,70,72</sup> MOF-74(Ni) is of increased interest for industrial applications due to the high relative stability in presence of moisture while maintaining high adsorption capacity even after many thermal adsorption/desorption cycles.<sup>54,73</sup>

MOFs provide many unique properties that can be tuned for distinct applications, however the lack of large-scale MOF synthesis methods that provide uniform high quality materials limits commercialization of many MOF enabled products. Traditional solvothermal syntheses of MOFs in batch reactors rely on long and energy intensive processes.<sup>58,74,75</sup> Alternative synthetic approaches have been developed to reduce expense and enhance processing to simultaneously provide better control over particle uniformity and growth by employing microfluidics,<sup>76,77</sup> electrochemistry,<sup>78,79,80</sup> sonochemistry, and microwave radiation.<sup>62,81,82,83,84,85,86</sup>

Scaling difficulties for MOFs have been overcome by employing continuous

flow synthesis approaches using conventional heating or some of the previously mentioned methods.<sup>87,88</sup> These approaches make use of relatively high temperatures and pressures to keep the synthesis in the solvothermal regime which gives high yields.<sup>79,89,90,91</sup> Recently an efficient space-time production approach has been published where a one-pot synthesis of the MOF-74(Ni) was carried out in water at atmospheric pressure with a 1 h reaction time.<sup>92</sup> This process generated 28.5 g.h<sup>-1</sup>.L<sup>-1</sup> of product with 92 % yield. However, an even higher space-time yield may be possible by separating the nucleation and growth regimes during the synthesis process. Procedures such as hot injection have been employed to attain high concentrations of precursors above the nucleation temperature, which allows formation of uniform nuclei. This process is then followed by a lower temperature growth regime. This approach becomes very impractical for large volumes due to mass and heat transfer limitations that lead to formation of less uniform particles.<sup>93</sup>

Compared to conventional heating, microwave heating is an excellent approach for initiating nucleation because of the rapid heating rates and uniform volumetric heating which lead to instantaneous nucleation, homogeneous growth, and high reproducibility of reactions.<sup>94,95</sup> Microwave heating can lead to uniform formation of particles under milder temperature and pressure, with reaction times in minutes as opposed to hours or days. Excellent control over nanoparticle size with very narrow size distributions has been shown for reactions using microwave heating.<sup>76,93,96,97</sup> Further improvements have also been enabled by using gas-liquid segmented flow in combination with microwave heating due to improved mixing, which reduces particle fouling, and also leads to more reproducible results.<sup>76,77,97</sup>

In this study, a microwave-assisted continuous flow reactor using gas-liquid segmented flow was employed to induce fast nucleation to accelerate MOFs synthesis while facilitating control over particle size. Synthetic conditions for MOF-74(Ni), were optimized by varying both the nucleation zone (microwave reactor) and growth zone (heating bath) temperatures. Several parameters were varied with the objective of maximizing reagent conversion with the shortest residence time under mild reaction conditions. The effect of microwave power and resulting nucleation temperature on the synthesis process was investigated to understand the underlying MOF formation mechanism.

#### Experimental section

**Chemicals:** All chemicals were used as purchased without any further purification. Nickel acetate tetrahydrate (> 98 %) was obtained from Alfa Aesar, 2,5-dihydroxyterephthalic acid (> 98 %), (DOBDC), was obtained from TCI America, and dimethylformamide (DMF) (99.8 %) was obtained from EMD.

**Synthesis:** The continuous microwave-assisted synthesis of MOF-74(Ni) was performed at 2.5 bar under solvothermal conditions, where a second peristaltic pump was used as a back pressure regulator. The precursor solution was prepared by mixing 50 mL of nickel (II) acetate tetrahydrate (0.12 M) in deionized (DI) water with 50 mL DOBDC dissolved in DMF (0.06 M). Argon gas was injected into the system using a T-junction to attain segmented flow. The reaction system used Teflon<sup>®</sup> tubing (1/8 in.

outer diameter, 1/16 in. inner diameter) in both the nucleation zone and growth bath. Precursors entered the nucleation zone that consisted of a microwave reactor with a waveguide (Sairem model PCCMWR340PVMR1PE GMP 30 K; 2.45 GHz; 3 kW) resulting in a nucleation residence time of  $\sim 1$  second. The temperature in the microwave zone ( $T_{MW}$ ) was measured using an infrared camera (FLIR model E40) that imaged a total irradiated length of approximately 4.7 cm. The growth region consisted of a 25.4 m long Teflon<sup>®</sup> coil submerged in an oil bath held at a fixed growth bath temperature ( $T_{GB}$ ). The growth region had an average residence time of about 8 min. After the reaction a liquid dispersion of the product was collected in a glass vial and then centrifuged to separate particles from solvents and unconverted reagents. MOF particles were then treated in the purification step by adding approximately 10 mL of water, followed by a second centrifugation with an addition of 10 mL of methanol. Over three days the particles were centrifuged and washed in 10 mL of fresh methanol up to four times. Activation was performed by keeping the samples under vacuum at 80 °C for three days prior to characterization.

**Characterization:** Powder X-ray diffraction (PXRD) was performed at room temperature using a Rigaku Ultima IV diffractometer ( $\text{Cu-K}\alpha = 0.1542$  nm). Data was collected from  $2\theta = 5$ - $50^\circ$ . Prior to PXRD, the dried powder was ground for about 2 min using a mortar and pestle. Thermogravimetric analysis (TGA) was performed using a TA Instruments TGA Q500. Samples were exposed to air for about 30 min and then heated up to 600 °C using a 10 °C/min ramp rate with a  $\text{N}_2$  flow rate of 60 mL/min. Two isothermal steps were taken at 105 and 250 °C for 20 min each. Transmission electron microscopy (TEM) imaging was performed using a FEI Titan

FEG at 200 kV. For TEM imaging, samples were prepared from a hexane dispersion of MOF-74(Ni) particles, which was sonicated for 10 min prior to preparation (Branson model 2510 – Max power 130 W). A carbon coated copper grid was dipped into the MOF dispersion twice and mounted in the microscope after drying at room temperature. Scanning electron microscopy (SEM) imaging was performed using an FEI Quanta 600 FEG SEM with 15-30 kV accelerating voltage. Raman spectra were obtained using a Horiba-Jobin Yvon HR-800 Raman spectrometer with a 532 nm incident laser source. UV-Vis spectroscopy was performed using an AvaSpec-3648 spectrometer on the precursor solution and the supernatant obtained from centrifuged reaction products to estimate conversion efficiencies. N<sub>2</sub> physisorption measurements were obtained using a Micromeritics ASAP 2020. Particle size was determined using dynamic light scattering (DLS) on a Brookhaven Instruments Corp. Zeta Potential analyzer. For the DLS measurements MOF-74(Ni) suspensions (in hexane) were analyzed after 30 min of sonication.

## Results and discussion

A schematic of the continuous flow microwave reactor is shown in Figure 26, where the nucleation and growth zones are indicated. The nucleation zone is heated using a microwave source, while the growth zone is heated using an oil bath. This system allows separation of the microwave zone temperature ( $T_{MW}$ ), and the growth bath temperature ( $T_{GB}$ ). Preliminary studies using single-phase flow were also performed to determine the effect of  $T_{MW}$  on conversion efficiencies when only using

microwave zone with a nucleation time of ~1 second. For example, we observed formation of particles at  $T_{MW} = 70\text{ }^{\circ}\text{C}$  (~ 4 % conversion) to  $150\text{ }^{\circ}\text{C}$  (~ 50 % conversion). Gas-liquid segmented flow was used to facilitate longer reaction times, and an inset in Figure 26 is provided which shows the velocity distribution in the liquid slugs. Gas-liquid segmented flow was also introduced to minimize fouling and deposition on reactor walls, which are common issues for continuous flow nanoparticle synthetic approaches. Deposition on the sidewall can cause clogging and also create hot spots in the microwave zone since deposited particles can have strong microwave absorption. Segmented flow has previously been employed in nanoparticle synthesis for inducing circulation within aqueous slugs and promoting better mass/heat transfer which results in more uniform products.<sup>77,93,96</sup>

Figure 27 shows powder X-ray diffraction (PXRD) data for particles synthesized using both the microwave zone and heating bath, as well as samples collected directly after the microwave zone with no heating bath. The sample collected using  $T_{MW} = 70\text{ }^{\circ}\text{C}$  and  $T_{GB} = 120\text{ }^{\circ}\text{C}$  gave a PXRD pattern for MOF-74(Ni) which is in agreement with available crystallographic data.<sup>5</sup> The most intense peaks were observed at  $2\theta = 6.8^{\circ}$  and  $11.8^{\circ}$  in all samples. The corresponding inter-planar spacings are  $d_{hkl} = 12.99\text{ \AA}$  and  $7.51\text{ \AA}$ , which are associated to crystallographic planes (-120) and (030), respectively. Broad PXRD peaks were obtained for MOFs synthesized using only the microwave zone for  $T_{MW}$  between 70 to  $150\text{ }^{\circ}\text{C}$ . The broad diffraction peaks could indicate formation of smaller particles or an amorphous phase. An increase in diffraction peak intensities were observed in the PXRD patterns for higher  $T_{MW}$ , which suggests the formation of more crystalline material as

microwave power and nucleation temperature increase. However, addition of the growth bath appears to be necessary to prepare highly crystalline MOFs.

Raman spectroscopy was employed as a complementary technique to PXRD to investigate changes related to MOF-74(Ni) linker or linker-metal under different reaction conditions. Figure 28 shows Raman spectra for MOF-74(Ni) grown under the same conditions as the PXRD results shown in Figure 27. Assignments of the Raman peaks are based on prior results,<sup>98</sup> where peaks at 1619, 1560, 570  $\text{cm}^{-1}$  are assigned to stretching vibrations and ring deformation vibrations from the benzene ring present in organic linker, respectively. Peaks at 1501 and 1416  $\text{cm}^{-1}$  are assigned to  $\nu(\text{COO}^-)_{\text{asym}}$  and  $\nu(\text{COO}^-)_{\text{sym}}$ , respectively. The very intense peak at 1275  $\text{cm}^{-1}$  is assigned to  $\nu(\text{CO})$  species after deprotonation of the carboxylic acid groups. The peak at 827  $\text{cm}^{-1}$  is assigned to benzene ring C-H bending modes and finally, the peak at 410  $\text{cm}^{-1}$  is assigned to (Ni-O<sub>ligand</sub>) bond vibration.<sup>98</sup>

All samples have similar relative peak intensities and peak widths for all  $T_{\text{MW}}$  using only the nucleation zone. This confirmed formation of MOF-74(Ni) for reactions run at both low and high  $T_{\text{MW}}$ . Based on the results of PXRD and Raman spectroscopy the  $T_{\text{MW}}$  changes the relative crystallinity of MOF-74(Ni), where PXRD appears to be more sensitive to the long-range order of the MOF. Prior studies have shown differences in adsorption properties of MOF-74(Ni) samples that were synthesized in a microwave batch reactor.<sup>20,20,41</sup> In these prior studies, higher microwave powers led to formation of smaller particles due to higher nucleation rates in the presence of microwave radiation. The presence of smaller particles resulted in an enhancement of the adsorption capacity of  $\text{N}_2$  and several hydrocarbons because of

the higher surface area available.

In Figure 29 we show PXRD patterns for MOF-74(Ni) samples as a function of  $T_{MW}$ . For all samples  $T_{GB}$  remained constant at 130 °C with an 8 min residence time. From top to bottom the PXRD patterns correspond to samples without microwave heating and samples at  $T_{MW} = 70, 110, \text{ and } 150$  °C. In all cases the XRD patterns are consistent with what is expected for this materials system. There is a significant reduction in peak intensity when the  $T_{MW}$  was increased to 110 and 150 °C, suggesting a reduction in crystallinity. As shown in the inset, the highest intensity was observed for  $T_{MW} = 70$  °C for the peak at  $2\theta = 31.7^\circ$ . In Figure 30 we show Raman spectra for samples grown under identical conditions as in Figure 29. In all cases the Raman spectra were consistent with that expected for MOF-74(Ni) without any peak shifts. When  $T_{MW}$  was increased to 110 and 150 °C the Raman peaks became weaker and broader, where the highest intensities were observed for  $T_{MW} = 70$  °C. These data suggest a general trend where there was a reduction of relative crystallinity for higher  $T_{MW}$ , with an optimal  $T_{MW} = 70$  °C.

Raman and PXRD have limitations in the identification of structural defects that may be formed during the very fast nucleation induced in the MW zone, or by formation of smaller grains leading to a nanocrystalline material, or combination of both. As such, transmission electron microscopy (TEM) was used to investigate effects of  $T_{MW}$  and correlate to changes in crystallinity. In Figure 31 A, B, and C we show TEM images for samples grown without microwave heating and with  $T_{MW} = 70$  and 150 °C, respectively. Larger MOF grains were observed for samples synthesized without microwave heating, whereas  $T_{MW} = 150$  °C showed formation of smaller

agglomerated grains which was likely due to the high nucleation rates. Agglomeration and formation of nanocrystalline material at  $T_{MW} = 150\text{ }^{\circ}\text{C}$  helps explain the increase in XRD and Raman peak widths. However, we found no major differences in PXRD, Raman, and TEM for samples synthesized at  $T_{MW} = 70\text{ }^{\circ}\text{C}$  and the sample synthesized without microwave heating. Using TEM the distances between crystallographic planes ( $d_{hkl}$ ) were estimated to be 1.30 nm and 0.78 nm, which are very close to the (-120) and (030) plane spacing in the MOF-74(Ni) structure. These plane spacing are also close to the values obtained from the PXRD data where  $2\theta = 6.8^{\circ}$  and  $11.8^{\circ}$  correspond to  $d_{hkl} = 1.299$  and  $0.751$  nm, respectively. The increase of relative crystallinity shown by PXRD and Raman spectroscopy for  $T_{MW} = 70\text{ }^{\circ}\text{C}$  may be attributed to a balance between increased nucleation and reduction of both agglomeration and growth induced by fast reaction rates in microwave zone. The grain sizes for the samples synthesized at  $T_{MW} = 70\text{ }^{\circ}\text{C}$  are larger in comparison to samples synthesized at higher  $T_{MW}$  and comparable to grains in the samples synthesized without microwave heating.

Particle size measurements were also compared for a range of  $T_{MW}$ . In Figure 32 we show that as  $T_{MW}$  increased the particle size increased and a broader particle size distribution was also observed. These results are summarized in Table 1.

Higher nucleation rates should occur for the reactions run at higher  $T_{MW}$ , especially since  $T_{GB}$  remained constant, and should result in a reduction of particle size since formation of more nuclei in the microwave zone would lead to smaller particles after the growth bath. However, high  $T_{MW}$  could lead to growth with high rates of diffusion, which could lead to formation of non-uniform and agglomerated

particles (Table 2).

LaMer *et al.*<sup>99</sup> has described a model for nucleation and growth which illustrates the benefits of keeping these regimes separate. High, but still uniform, nucleation rates can be achieved when nucleation temperatures (i.e.,  $T_{MW}$ ) increase and can influence the final properties of particles since available precursor concentrations decrease rapidly while uniform nuclei are generated. However, the increase of nucleation temperatures also enhances diffusion and reaction rates. At higher nucleation temperatures rapid diffusion could influence the continuous growth of particles after fractions of a second in the microwave zone. Therefore, tuning the microwave reactor to achieve a regime in which significant nucleation occurs but diffusion and concentration are low enough to ensure slow and more uniform growth becomes a key factor to obtain more uniform particle synthesis.

The increase of nucleation rate as a function of  $T_{MW}$  could be confirmed by the increasing number of smaller grains observed on the sample synthesized at  $T_{MW} = 150$  °C. However, this complex system, which was optimized for a high space-time-yield of MOF-74(Ni), has high reagent diffusion rates and increased mobility due to the high concentrations employed. Therefore, application of microwave energy that induced significant nucleation with a combination of less driven growth ( $T_{MW} = 70$  °C) as opposed to highly driven growth ( $T_{MW} = 150$  °C) resulted in larger grains and higher relative crystallinity. High  $T_{MW}$  does induced faster nucleation, but overheating results in new nuclei being formed due to high diffusion and mobility of precursors resulting in increased particle sizes. Increased broadening for the sample  $T_{MW} = 150$  °C in the dynamic light scattering (DLS) results may indicate that growth

and new nucleation occurred rather than isolated nucleation.

Another factor that could be considered as a plausible cause for agglomeration could be high microwave absorption by MOF-74(Ni). These particles could potential be hotspots and create higher temperature gradients closer to their surface. Several experiments were performed by measuring the temperature of MOF-74(Ni) suspensions at different concentrations in the microwave zone. Initially we used a high absorbing solvent (deionized water and dimethylformamide (DMF) - 50 % v/v) containing different concentrations of MOFs (9.5, 4.75, and 1.9 g.L<sup>-1</sup>) to evaluate their effect on T<sub>MW</sub> at constant microwave power. None of the suspensions had significant temperature differences ( $\pm 2$  °C) when compared to pure solvent. A second experiment was carried out using pure toluene (very low microwave absorbing solvent) and a suspension of MOFs containing 9.5 g.L<sup>-1</sup> of MOF-74(Ni). Again no significant differences in temperature were observed for the solvent compared to the suspensions.

In Figure 33, we show physisorption results for MOF-74(Ni) for different T<sub>MW</sub>. For samples synthesized at T<sub>MW</sub> = 70 °C, or without any microwave heating, the resulting N<sub>2</sub> physisorption isotherms were of type I (Brunauer classification) which is characteristic of microporous materials.<sup>100,101</sup> High T<sub>MW</sub> changed the general behavior of measured isotherm to type 2, which is identified by an increase of N<sub>2</sub> uptake at high relative pressures. This change can be attributed to the agglomeration of the small crystals shown in Figure 31. In Figure 34 we show surface area measurements for the MOFs. High surface areas were obtained for all samples which were close to values available in the literature (1070 m<sup>2</sup>.g<sup>-1</sup>), even though the reaction

times in this study were significantly shorter.<sup>74</sup> A summary of results for different reaction conditions are provided in Table 2. An approximate pore diameter ( $d_p$ ) of 11 Å was calculated for all samples using an incremental surface area analysis, which is in agreement with literature estimates for MOF-74(Ni).<sup>54</sup> However, a lower surface area and slightly shifted peak can be seen for the sample prepared at  $T_{MW} = 150$  °C. In addition different intensities of cumulative surface area varying with  $T_{MW}$  was also observed, which may be related to the agglomerated grains obtained for this sample. These results also indicate that the total surface area for each sample differs as a function  $T_{MW}$ . Pores and intracrystalline diffusion appear to be responsible for nearly all the area obtained by these measurements ( $d_p < 20$  Å), although some contribution appears to occur in the region of 20 – 100 Å which could be attributed to regions in between agglomerated particles (intercrystalline diffusion).

The influence of different activation procedures and their relationship to the presence of pore collapse in MOFs has been previously studied.<sup>102</sup> For these studies interparticle mesoporosity was observed due to the misalignment of micropores at interparticle regions and grain boundaries. The presence of structural defects, with trapped solvent in the pores, can effect internal diffusion and therefore decrease total adsorption capacities. Therefore, the agglomeration seen in our samples could hinder intracrystalline diffusion due to grain/grain boundaries and consequently reduce available surface area for adsorption.

In Figure 35 we show thermogravimetric analysis data for MOF samples under flowing  $N_2$ . These data indicate that samples had mass losses associated to water and DMF desorption during the temperature ramp. The isothermal steps

indicate steep weight losses that are correlated with desorption of moisture and residual solvents that remained in the pores after the activation process. The data also indicate that MOF-74(Ni) thermally decomposed at approximately 350 °C, which is consistent with prior studies.<sup>92</sup>

## Conclusions

In summary, a continuous and segmented flow microwave-assisted synthesis of the MOF-74(Ni) was performed under mild conditions of pressure (~2.5 bar) with high conversion of reagents (~ 96.5 %) and space-time yield (~ 80 – 90 g.h<sup>-1</sup>.L<sup>-1</sup>). Segmented flow was employed to improve mixing and reduce particle fouling which allowed long reactions to be run with very good reproducibility of results. Very stable T<sub>MW</sub> were obtained in the segmented flow regime for all reactions reported. The microwave zone helped reduce reaction times down to 8 min and increased nucleation. Faster nucleation at higher T<sub>MW</sub> resulted in the formation of smaller grains, which resulted in different adsorption behavior even after the growth bath. This was due an agglomeration of grains and formation of structural defects at higher T<sub>MW</sub>, and may result in misaligned and collapsed pores. High microwave absorption by solvents and higher diffusion conditions could significant influence growth in microwave zone and possibly result in more heterogeneous particles.

## Acknowledgements

This work was funded by the United States Department of Energy through ARPA-E and the Department of the Navy.

Table 1: Particle size obtained from dynamic light scattering and scanning electron microscope. Particles were measured using software ImageJ<sup>®</sup>.

<b>Conditions</b>	<b><math>d_p</math> - DLS (nm)</b>	<b><math>d_p</math> - SEM (nm)</b>
<b>No MW</b>	1483 ± 140	1200 ± 430
<b>MW 70 °C</b>	1557 ± 142	1333 ± 470
<b>MW 150 °C</b>	2505 ± 170	2240 ± 1110

Table 2: Reagents conversion (evaluated using UV-Vis spectroscopy for Ni<sup>2+</sup> concentration), mass production rate of MOF-74(Ni), and XRD full width at half maximum (FWHM) from reactions operated in segmented flow at different T<sub>MW</sub>.

<b>Conditions</b>	<b>Conversion</b> (%)	<b>Mass</b> <b>prod. rate</b> <b>MOF-74(Ni)</b> (g/h)	<b>XRD</b> <b>FWHM at</b> <b>31.75° (°)</b>	<b>S<sub>BET</sub></b> (m <sup>2</sup> /g)
<b>No MW</b>	90.8	3.93	0.660	1012 ± 6
<b>MW 70 °C</b>	92.3	4.46	0.536	938 ± 6
<b>MW 110 °C</b>	94.3	4.51	0.662	936 ± 6
<b>MW 150 °C</b>	96.5	4.56	0.850	840 ± 3

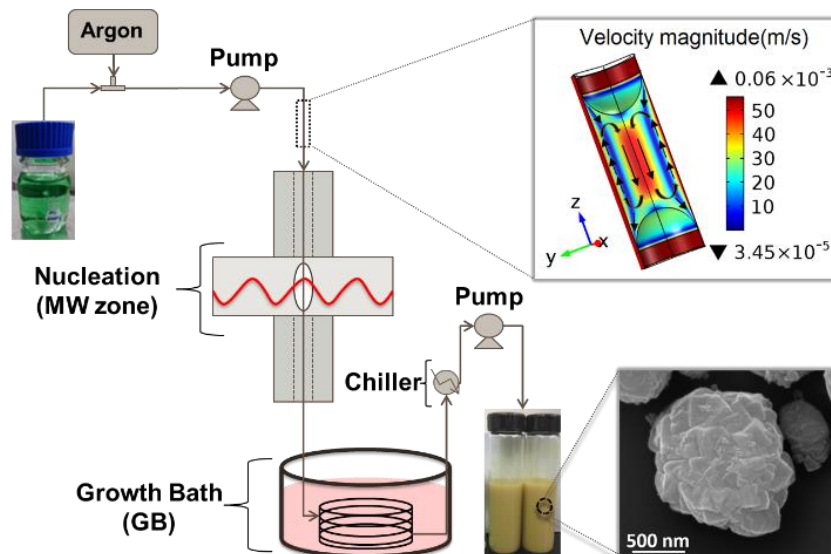


Figure 26: Schematic of segmented continuous flow microwave-assisted synthetic reactor for MOF-74(Ni). Model on top right was obtained using Comsol<sup>®</sup> shows turbulence in between slugs in segmented flow.

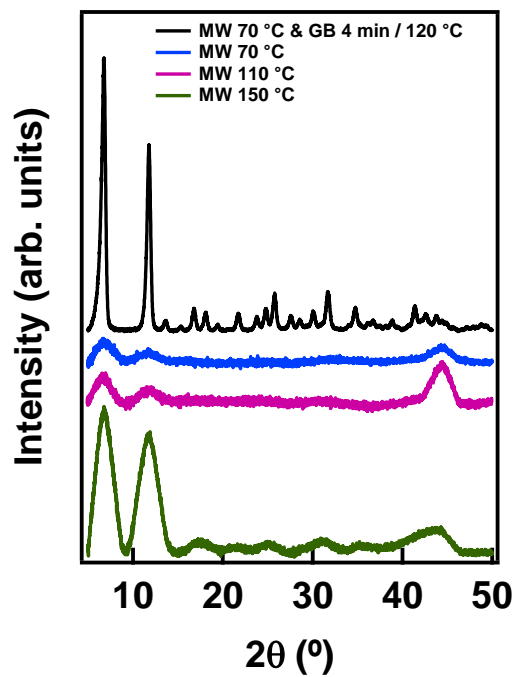


Figure 27: XRD data from MOF-74(Ni) synthesized at different  $T_{MW}$  compared to a sample, which has been synthesized using a combination of both microwave zone and growth zone. (Peak at  $2\theta = 44^\circ$  present in samples from microwave only synthesis is due to XRD metal sample stage)

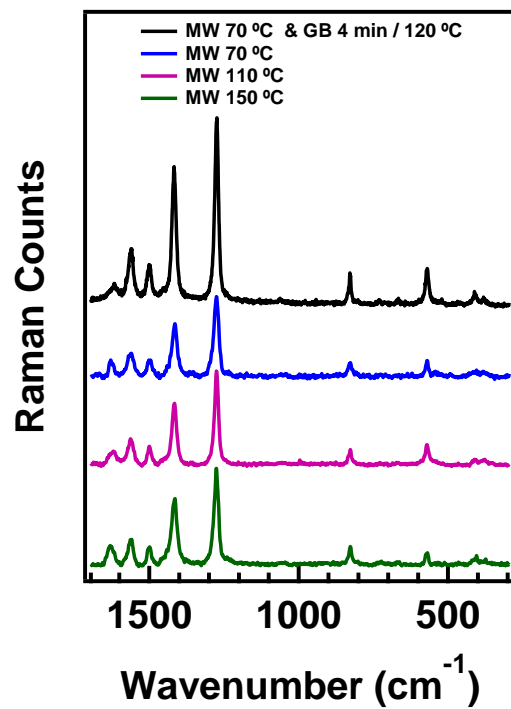


Figure 28: Raman spectra of MOF-74(Ni) samples, which were synthesized at different  $T_{MW}$  compared to a sample that went through a combination of microwave zone and growth zone.

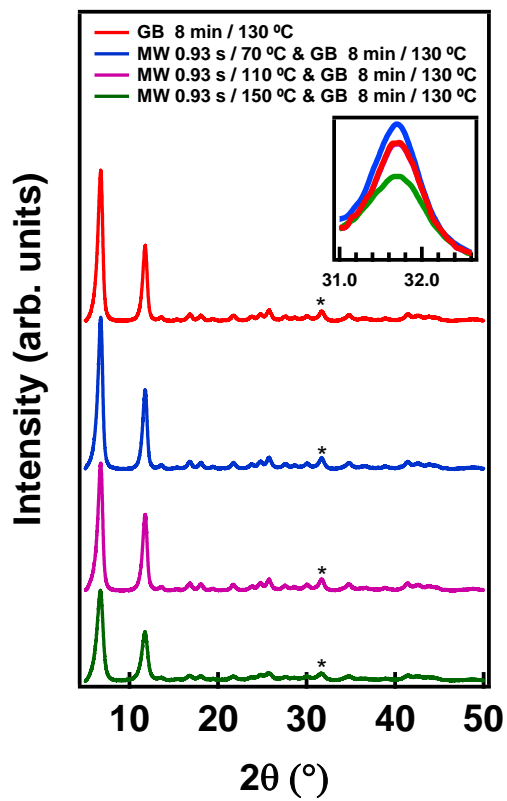


Figure 29: XRD data of samples synthesized at different  $T_{MW}$  while growth zone was maintained at constant temperature and residence time. (XRD peaks at 31.75 ° are shown in inset)

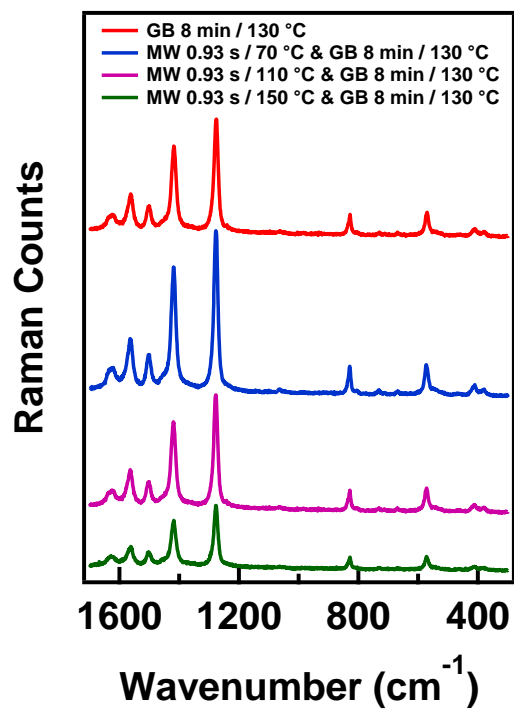


Figure 30: Raman spectroscopy of MOF-74(Ni) samples synthesized at different  $T_{MW}$  while growth zone was maintained at constant temperature and residence time.

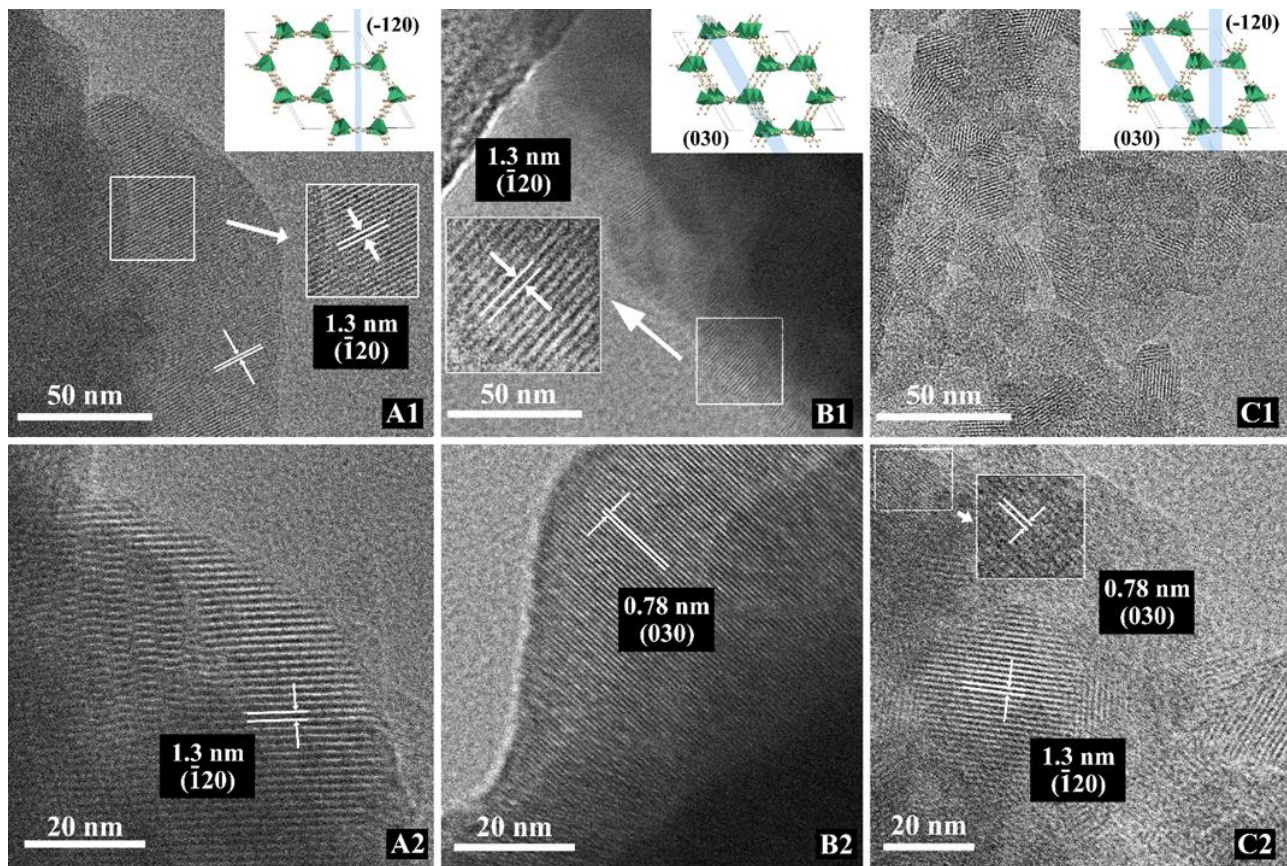


Figure 31: TEM images of samples synthesized without microwaves (A) and at  $T_{MW} = 70$  and  $150$  °C (B and C, respectively).

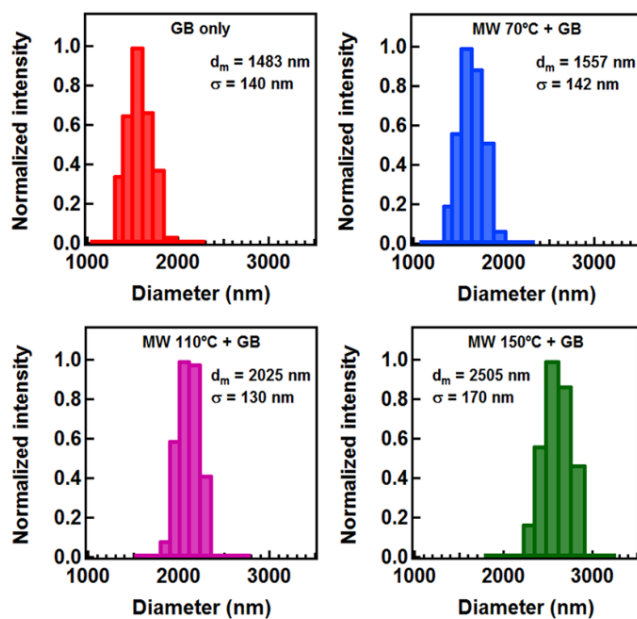


Figure 32: Particle size measurements using on dynamic light scattering taken for samples synthesized with and without microwaves, and different  $T_{MW}$ .

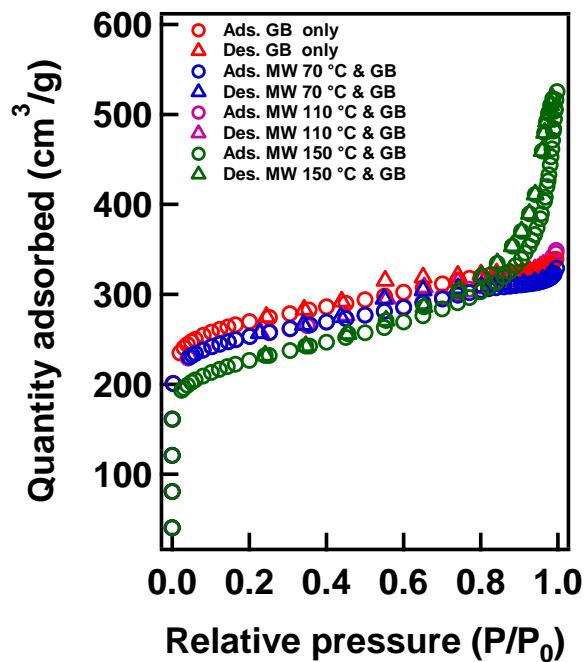


Figure 33: N<sub>2</sub> physisorption isotherms obtained for segmented continuous flow synthesis of MOF-74(Ni) with and without the use of microwaves. T<sub>MW</sub> was also varied keeping the average residence time constant (0.93 s) while growth zone conditions were fixed at 130 °C for 8 min.

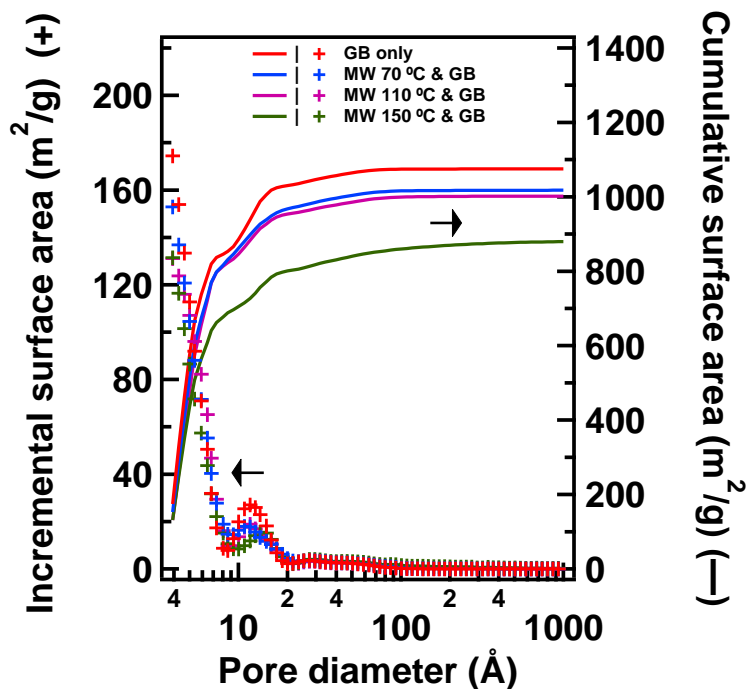


Figure 34: Cumulative surface area (solid lines) and Incremental surface area (crosses) for MOF-74(Ni) synthesized using segmented flow with and without the use of microwaves.  $T_{MW}$  was also varied keeping the average residence time constant (0.93 s) while heating zone conditions were fixed at 130 °C for 8 min.

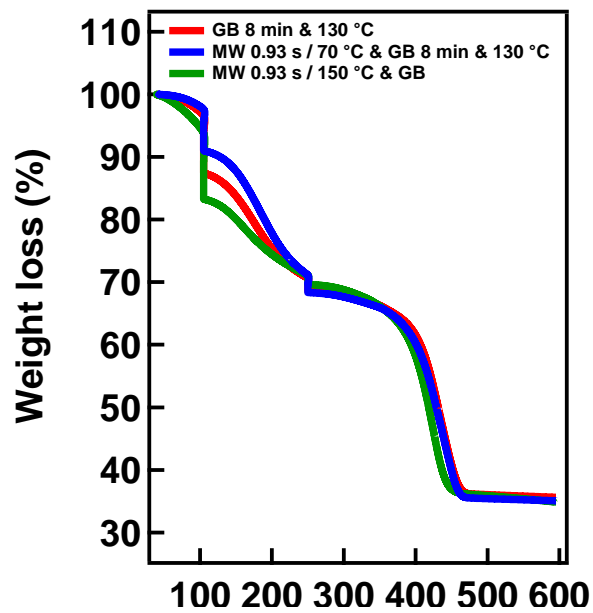


Figure 35: Thermographic analysis performed on MOF-74(Ni) samples synthesized with and without microwaves, and at two different  $T_{MW}$ .

## CHAPTER 5

CHEMICALLY MODULATED MICROWAVE-ASSISTED  
SYNTHESIS OF MOF-74(Ni) AND PREPARATION OF MOF-  
MATRIX BASED MEMBRANES FOR REMOVAL OF METAL IONS  
FROM AQUEOUS MEDIA

Gustavo H. Albuquerque and Gregory S. Herman\*

Oregon State University, School of Chemical, Biological and Environmental  
Engineering, Corvallis, OR 97331-2702, USA

\*Corresponding Author

Reproduced from Cryst. Growth. Des., vol. 17, issue 1, pp. 156-162, 2017

Copyright 2017 American Chemical Society

## Abstract

In this study, microwaves and chemical modulators were used in combination to improve the uniformity of synthesized MOF-74(Ni) materials. A segmented flow, microwave-assisted reactor was used where rapid nucleation in the microwave zone was separated from growth processes in an oil bath. High temperatures in the microwave zone induce fast nucleation, which can result in the formation of polydisperse products through agglomeration that reduces the available surface area. Benzoic acid was used as a chemical modulator where higher benzoic acid to Ni<sup>2+</sup> concentration ratios resulted in a substantial increase in reaction apparent activation energies for short reaction times (~1 s). Optimization of the synthetic process resulted in MOF-74(Ni) particles with high crystallinity, high surface area, and narrow particle size distributions. These synthesized MOF-74(Ni) particles were used to prepare MOF-Nafion<sup>®</sup> matrix based membranes to investigate the removal of metal ions from aqueous solutions with high efficiencies.

## Introduction

One of the main challenges in nanomaterials synthesis is controlling particle uniformity, which often impacts the physical and chemical properties of nanomaterials. Batch synthetic methods, such as hot injection and extended LaMer's, leads to the formation of products with very similar reaction history and narrow particle size distributions.<sup>103,104</sup> From the manufacturing perspective, control over particle size using these approaches becomes much more difficult for significantly larger batch sizes. The combination of microwave heating with continuous flow approaches can provide improved scalability and higher uniformity for the synthesis of nanomaterials.<sup>105,106,107</sup> It has been proposed that continuous flow, microwave-assisted reactors (CFMR) can potentially enable the production of nanomaterials that currently lack scalable synthetic approaches, such as metal-organic frameworks (MOFs).<sup>108</sup>

MOFs are a relatively new class of hybrid materials with increasing scientific interest. The development of scalable methods to synthesize MOFs is of increasing academic and industrial interest. MOFs consist of metal ions (or metal containing clusters) coordinated with polytopic organic linkers (bridging ligands) which form a crystalline porous coordination polymer. The main characteristics of MOFs are high surface area, tunable pore structure, and a diversity of chemistries, structures, and post-synthetic processes that can significantly modify the MOFs chemical properties. All of these attributes make MOFs suitable for a wide range of applications including, gas separation, adsorption, selective catalysis, sensing, and

pharmaceuticals.<sup>109,110,111,112,113</sup>

Continuous flow methods have recently demonstrated promising results for the synthesis of MOFs,<sup>114</sup> where CFMR has shown improvements in reagent utilization, with a significant reduction in reaction times.<sup>105,107,115,116</sup> Microwave radiation can rapidly heat reactants to high temperatures allowing fast nucleation rates, while shortening reaction times, and increasing conversion rates. However, high microwave temperatures can also result in the formation of agglomerated particles, which can reduce the available surface area and decrease the MOFs adsorption performance.<sup>115</sup>

Chemical modulators have also been used to control MOF nucleation and growth.<sup>117,118</sup> Modulation has been investigated by using monocarboxylic acids, which compete with polytopic organic linkers for coordination with metal ions. These competitive reactants have been shown to modify both nucleation and growth of MOF particles for relatively long reaction times (1 to 24 hours), and have resulted in more monodisperse particles.<sup>117,118,119,120,121,122,123</sup> However, the effect of modulators for short reaction times has not been demonstrated for MOFs.

MOFs have extremely high adsorption areas and chemical selectivity, which have led to their use to remove a range of toxic and undesired compounds.<sup>124,125,126,127,128</sup> Several MOFs have shown selective adsorption of toxic metals.<sup>129,130</sup> The MOF-74 series is of interest for these applications due to the relatively good stability in the presence of moisture,<sup>131</sup> and may also improve the removal of toxic metals from aqueous media when incorporated in composite membranes.<sup>132,133,134</sup>

In this study, chemical modulation was investigated for the synthesis of MOF-

74(Ni) using a CFMR. Benzoic acid (BA) was used as the modulator and we determined the optimal concentration of chemical modulators to reduce agglomeration, increase crystallinity, and provide improved adsorption performance. The synthesized MOF-74(Ni) particles were used to prepare composite Nafion<sup>®</sup> membranes, and these composite membranes were investigated for the removal of metal ions from aqueous solutions.

## Experimental section

**Chemicals:** All chemicals were used as purchased without any further purification. Nickel acetate tetrahydrate (> 98 %) was obtained from Alfa Aesar, 2,5-dihydroxyterephthalic acid (DOBDC, > 98 %), was obtained from TCI America, dimethylformamide (DMF, 99.8 %) was obtained from EMD, sodium hydroxide and methanol (ACS grade) were obtained from Macron, and benzoic acid (BA, 99.5 %) was obtained from J.T. Baker. Dupont<sup>™</sup> D2020 Nafion solution was obtained from Ion Power and was used for the composite preparation.

**Synthesis:** The segmented flow microwave-assisted synthesis procedure for the MOF-74(Ni) has been described previously.<sup>115</sup> The metal precursor solution was prepared by mixing nickel (II) acetate tetrahydrate (0.06 M) in 50 mL of deionized (DI) water, while DOBDC (0.03 M) was dissolved in 50 mL DMF. The metal precursor solution was prepared with different BA to Ni<sup>2+</sup> concentration ratios. NaOH was used to neutralize benzoic acid by keeping the pH of all reagent solutions at 8.0.

For these experiments, the microwave zone temperature ( $T_{MW}$ ) was set to 423 K and the temperature was monitored using an infrared camera (FLIR model E40). The total irradiated length was 4.7 cm and the volumetric flowrate was  $\sim 5.2 \text{ mL}\cdot\text{min}^{-1}$ , which results in a microwave zone residence time of  $\sim 1$  second (Teflon<sup>®</sup> tubing – I.D. = 1/16 inch). The growth zone used the same tubing with a length of 39.5 m, and was submerged in an oil bath held at 373 K. This resulted in an average residence time of  $\sim 15$  min. After the reaction, a liquid dispersion of the product was cooled and collected in a glass vial and then centrifuged to separate particles from solvents and unconverted reagents. MOF particles were then treated in a purification step by adding approximately 10 mL of water to an equal amount of product liquor, followed by a second centrifugation, removal of supernatant, and addition of 10 mL of methanol. Over the course of three days the particles were centrifuged and washed in 10 mL of fresh methanol up to four times. Activation was performed by keeping the samples under vacuum at 80 °C for three days prior to characterization.

**Composite preparation and adsorption tests:** MOF-74(Ni) particles synthesized using  $C_{BA}/C_{Ni^{2+}} = 0.1$  were mixed with a Nafion<sup>®</sup> solution. This mixture was prepared with 4 mL of a Nafion<sup>®</sup> solution in n-propanol (20% wt.) with 5 % wt. MOF in the polymer matrix. After stirring for 20 min, the mixture was spin coated onto 1 x 1 inch<sup>2</sup> silicon substrate. Prior to spin coating, the substrate was rinsed with acetone, methanol, and deionized water, followed by a 15 minute long UV-Ozone treatment (PSD Pro Series – Novascan). A layer of pure polymer (Nafion<sup>®</sup>) was deposited on the substrate by spin coating (500 rpm/30 s), followed by drying at 60 °C for 20 minutes. This was followed by five spincoating cycles of the MOF-74(Ni)/Nafion<sup>®</sup> mixture

using the same spin coating conditions and drying process between each coat. A final layer of pure polymer was coated on top of the stack to form a protective layer to prevent loss of MOF particles. The total thickness of the film was 300  $\mu\text{m}$  as determined using a 3D optical profiler (ZeScope – Zometrics). When the substrate was covered with water the film would peel off of the substrate and float to the water surface. The films were held under vacuum for 24 hours before characterization or further experiments. A piece of the composite and pure polymer were immersed in 50 mM solutions containing metals salts (i.e.,  $\text{Cu}(\text{NO}_3)_2$ ,  $\text{Zn}(\text{NO}_3)_2$ ,  $\text{Pb}(\text{NO}_3)_2$ , and  $\text{AgNO}_3$ ). The concentration of metals in each composite and pure polymer was determined using inductively coupled plasma-optical emission spectroscopy (ICP-OES).

**Characterization:** Powder X-ray diffraction (PXRD) was performed at room temperature using a Rigaku Ultima IV diffractometer ( $\lambda_{\text{Cu-K}\alpha} = 0.1542 \text{ nm}$ , 40 kV, 40 mA). Prior to PXRD, the dried powder was ground for about 2 min using a mortar and pestle. Raman spectra were obtained using a Horiba-Jobin Yvon HR-800 Raman spectrometer with a 532 nm incident laser source. UV-Vis spectroscopy was performed using an AvaSpec-3648 spectrometer.  $\text{N}_2$  physisorption measurements were obtained using a Micromeritics ASAP 2020. Particle size was determined using dynamic light scattering (DLS) on a Brookhaven Instruments Corp. Zeta Potential analyzer. For the DLS measurements MOF-74(Ni) suspensions (in ethanol) were analyzed after 30 minutes of sonication (Branson model 2510 – Max power 130 W). Elemental analysis was performed using a Teledyne Leeman Prodigy inductively coupled plasma-optical emission spectrometer. For ICP-OES analysis a fixed amount of MOF composite films

(approx. 20 mg) was digested for 5 hours at 185 °C in a 20 mL Parr reactor. For digestion of the polymers and composites 2.25 mL concentrated nitric acid and 0.25 mL H<sub>2</sub>O<sub>2</sub> 30 % v/v was used. As a testing procedure, the amount of MOF-74(Ni) in the composite was determined by measuring the amount of nickel after the digestion of samples. Using this method, it was determined that 4.6 % wt. of MOF was in the composite. This value was very close to the amount of MOF (~ 5 % wt.) used in the preparation of the composite films.

## Results and discussion

In Figure 36(A) we compare the percent conversion of metal precursors for different microwave zone reaction temperatures ( $T_{MW}$ ) and BA to Ni<sup>2+</sup> concentration ratios. For these results the percent conversion was estimated based on the reduction in the Ni<sup>2+</sup> absorption using UV-Vis spectroscopy. These reactions were performed only using the microwave zone to better contrast the effect chemical modulators have on nucleation rates. Higher concentration ratios of BA to Ni<sup>2+</sup> resulted in a significant reduction in Ni<sup>2+</sup> conversion, suggesting a decrease in reaction nucleation rates.

These data allow us to calculate a reaction rate constant ( $k$ ), which can then be plotted in an Arrhenius form as shown in Figure 36(B). The apparent activation energies ( $E_a$ ) are given in Figure 36(B), and the  $E_a$  for the highest BA to Ni<sup>2+</sup> concentration ratio was found to be ~43 % higher than for reactions without BA. These results suggest that the BA and polytopic organic linker competitively react with Ni<sup>2+</sup> during the synthesis of MOF-74(Ni). This competition can decrease the reagent conversions,

however chemical modulators can also modify the crystal morphology of MOFs and result in improved performance for sensing and catalytic applications.<sup>120</sup> To further improve conversion efficiencies and particle uniformity we have added a heated bath after the microwave zone. This setup allows us to effectively separate nucleation processes, in the microwave zone, and growth processes, in the growth zone. For the remaining experiments, all reactions were performed with BA as the chemical modulator,  $T_{MW} = 423$  K and the growth bath temperature ( $T_{GB}$ ) set to 373 K.

In Figure 37, we show powder X-ray diffraction (PXRD) for samples synthesized with several different BA to  $Ni^{2+}$  concentration ratios. PXRD allowed us to characterize structural changes in MOF-74(Ni) due to changing the BA to  $Ni^{2+}$  concentration ratios, with all other reaction parameters held constant. PXRD patterns confirmed the formation of MOF-74(Ni), except for the sample synthesized with the highest BA to  $Ni^{2+}$  concentration ratio. The most intense PXRD peaks used to identify MOF-74(Ni) are at  $2\theta = 6.8$  and  $11.8^\circ$ , which correspond to the crystal interplanar spacings (-120) and (030), respectively. These main peaks were present for both samples synthesized at low BA to  $Ni^{2+}$  concentration ratios, and samples synthesized without any modulators. When a small amount of BA was added to the reaction mixture solution, an increase in intensity for the PXRD peak was observed, as shown in the inset of Figure 38. The highest PXRD peak intensity was observed for a 10 % BA to  $Ni^{2+}$  concentration ratio ( $C_{BA}/C_{Ni^{2+}} = 0.1$ ), where higher concentration ratios resulted in an increase in the full width at the half maximum (FWHM) of the diffraction peak and a reduction in the diffraction peak intensities. These results suggest there is a reduction in the relative MOF-74(Ni) crystallinity for

these higher concentration ratios. For the highest BA to Ni<sup>2+</sup> concentration ratio no diffraction peaks were observed which suggests the formation of an amorphous phase.

In Figure 38 we show Raman spectra for the samples characterized in Figure 37. The spectra have peaks at wavenumbers that have previously been reported for MOF-74(Ni).<sup>115,135</sup> A similar trend to the PXRD data is observed for the Raman spectra where an increase in FWHMs and reduction in peak intensities were observed for  $C_{BA}/C_{Ni^{2+}} > 0.1$ . These changes can be related to the significant increase in  $E_a$  for higher BA to Ni<sup>2+</sup> concentration ratios, which can lead to significant structural disorder. High BA concentration leads to the formation of less crystalline materials, and even amorphous materials for the highest concentration ratios used in this study.

In Figure 39 we show dynamic light scattering (DLS) results for MOF-74(Ni) synthesized with different BA to Ni<sup>2+</sup> concentration ratios. Increasing the BA to Ni<sup>2+</sup> concentration ratios result in larger effective particle diameters with tighter particle size distribution. In a prior study, we obtained more polydisperse particles without the use of modulators for reactions performed for similar reaction conditions.<sup>115</sup> In the present study, we find chemical modulators significantly decrease the FWHM of the effective diameter of the synthesized MOFs.

In Figure 40 we show a model used to describe nucleation and growth of nanoparticles, which was initially proposed by LaMer *et al.*<sup>136</sup> The traditional nucleation and growth model describes a concentration profile change for a hypothetical reagent at a concentration above supersaturation, where there is enough energy to initiate nucleation. Formation of nuclei occurs rapidly and as a result, the

concentration of reagents is quickly reduced. After nuclei formation, diffusional growth takes place as the concentration gradient of reagents to crystals is reduced. Finally, Ostwald ripening becomes the dominant growth regime. Chemical modulation effects are a result of competitive interactions between metal precursors and the modulators and organic linkers. This interaction leads to growth and nucleation tuning due to an increase in the energy needed to overcome the nucleation threshold and allow diffusional growth.<sup>118,119</sup> The increase in activation energy for increased BA to Ni<sup>2+</sup> concentration ratios (Figure 36(B)) can be attributed to the competitive interactions between Ni<sup>2+</sup>, and the modulator and polytopic organic linker. This causes a change in the nucleation threshold and results in decreased growth rates. This change is qualitatively described in Figure 40. The increase in activation energy leads to lower reaction rates in the microwave zone. This decreases the amount of nuclei and therefore larger crystals can be formed as a product. Another aspect of using modulators is that the slower growth rates result in tighter particle size distributions.

In Figure 41 we show N<sub>2</sub> physisorption isotherms for MOF-74(Ni) particles grown with and without modulators. Different amounts of chemical modulators, and the resulting difference in relative crystallinity, significantly modifies the adsorption behavior of the synthesized MOF particles. For low BA to Ni<sup>2+</sup> concentration ratios, an increase in the amount of adsorbed nitrogen was observed. An isotherm that is characteristic of microporous materials (type I - according to the Brunauer classification) was obtained for these samples.<sup>137</sup> For higher BA to Ni<sup>2+</sup> concentration ratios, the isotherm was similar to samples with no modulators, where the isotherm was

characteristic of mesoporosity. For the highest BA to  $\text{Ni}^{2+}$  concentration ratio, the isotherm had an intermediate behavior between type II and type III that is characteristic of materials that have predominantly multilayer adsorption, which implies a lack of microporosity. Figure 42 shows the incremental and cumulative surface areas extracted from data presented in Figure 41. These surface area curves show similar trends where the highest (lowest) cumulative surface area occurs for the sample synthesized with the lowest (highest) BA to  $\text{Ni}^{2+}$  concentration ratio. The pore size distribution agreed well with the average size expected for MOF-74(Ni), which is  $\sim 11 \text{ \AA}$ .<sup>138</sup> Finally, a wide distribution of pore sizes was observed for the highest BA to  $\text{Ni}^{2+}$  concentration ratio, which agrees with the formation of an amorphous material. These results are consistent with PXRD results.

Figure 43 summarizes the increase in relative mass of the absorbed metal ions for MOF-74(Ni)/Nafion<sup>®</sup> composites compared to pure Nafion<sup>®</sup> samples. The increase in relative mass was estimated using the difference in metal wt.% between the composite and pure Nafion<sup>®</sup> films as determined by ICP-OES. This difference in mass was then divided by the mass of the MOF in the composite samples to obtain a relative mass absorbed. Samples containing pure Nafion<sup>®</sup> were found to adsorb metal ions, however the amount of adsorbed  $\text{Cu}^{2+}$ ,  $\text{Pb}^{2+}$ , and  $\text{Ag}^+$  were significantly higher for MOF-74(Ni)/Nafion<sup>®</sup> composites. The MOF-74(Ni)/Nafion<sup>®</sup> composite adsorption capacity for  $\text{Cu}^{2+}$ ,  $\text{Pb}^{2+}$ , and  $\text{Ag}^+$  were within the range of values obtained for industrial waste materials commonly used to remove heavy metals from aqueous solutions.<sup>139</sup> In order to investigate the metal ion adsorption mechanism for MOF-74(Ni)/Nafion<sup>®</sup>

composite films we have further characterized the composites after exposure to metal ion containing aqueous solutions.

In Figure 44 we show XRD results for pure Nafion<sup>®</sup> and MOF-74(Ni)/Nafion<sup>®</sup> composite samples before and after exposure to a solution containing copper or silver nitrate. XRD was performed to determine if any structural changes occurred for the MOF particles after the extended adsorption experiments in aqueous solutions. Nearly identical XRD patterns were obtained for MOF-74(Ni)/Nafion<sup>®</sup> composite samples after exposure to Zn<sup>2+</sup> and Pb<sup>2+</sup> solutions. The broad XRD peak observed at  $2\theta = 8 - 22^\circ$  is due to Nafion<sup>®</sup>.<sup>140</sup> Close inspection indicates diffraction peaks at  $2\theta = 6.8$  and  $11.8^\circ$ , which are characteristic of MOF-74(Ni) dispersed in the polymer. No diffraction peaks characteristic of copper or silver particles were found at higher  $2\theta$ . The inset indicates that there is a slight broadening of the XRD peak at  $2\theta = 6.8^\circ$  after exposure to Ag<sup>+</sup>, while not for Cu<sup>2+</sup>. The XRD results suggest that there is an interaction between Ag<sup>+</sup> and the MOF-74(Ni) in the composite film, whereas there is a less significant structural interaction for Pb<sup>2+</sup>, Zn<sup>2+</sup>, or Cu<sup>2+</sup>.

In Figure 45(A) and (B) we show Raman spectra for MOF-74(Ni)/Nafion<sup>®</sup> films before and after exposure to solutions containing Cu<sup>2+</sup> and Ag<sup>+</sup> ions. No difference in the Raman spectra was observed between the Nafion<sup>®</sup> and MOF/Nafion<sup>®</sup> composites prior to exposing the samples to solutions, due to the low concentration of MOF particles in the composite films. The Raman spectra did not change after exposure to copper nitrate solution, whereas significant changes were observed after exposure to silver nitrate solution. In Figure 45(B) Raman spectra from Nafion<sup>®</sup> is shown where four distinct vibrational bands at 731, 1216, 1297, and 1377 cm<sup>-1</sup> are observed, which

correspond to  $[-(\text{CF}_2\text{CF}_2)-]$  groups present in the polymer backbone. Side chains in Nafion<sup>®</sup> result in the five other vibrational bands observed at 805, 971, 1060, 1180, and 1360  $\text{cm}^{-1}$ .<sup>141,142,143</sup> Prior studies have paid special attention to the two peaks located at 971 and 1060  $\text{cm}^{-1}$  due to their sensitivity to cation exchange in Nafion<sup>®</sup>.<sup>144,145,146</sup> These peaks correspond to symmetric stretch modes of the ether group and the S-O bonds in the Nafion<sup>®</sup> structure and change when dehydration or cation exchange processes occur. After exposure to an aqueous solution of silver nitrate the Raman spectra of composite films significantly changes, where two intense peaks at 1358 and 1585  $\text{cm}^{-1}$  are observed. These results suggest the formation of silver nanoparticles upon  $\text{Ag}^+$  ion exposure.

Previous studies have used surface-enhanced Raman spectroscopy to investigate the interaction Nafion<sup>®</sup> ionomers and gold and platinum surfaces.<sup>141</sup> New Raman peaks, and an increase in intensities, was observed in these experiments due to interactions between the Nafion<sup>®</sup> ionomers and the SERS-active materials.<sup>147</sup> In Figure 45(B), the adsorption of  $\text{Ag}^+$  results in the disappearance of the Raman peak at 1060  $\text{cm}^{-1}$  and the appearance of new Raman peaks at 912, 938, and 960  $\text{cm}^{-1}$ . A red shift of the symmetric stretching mode  $\text{SO}_3^-$  (usually located at 1060  $\text{cm}^{-1}$ ) has previously been observed using bis(3-sulfopropyl)disulfide on copper surfaces<sup>139</sup> and when using different sulfonate polymers on gold and platinum surfaces.<sup>148</sup> These changes may be attributed to either a lowered symmetry of the vibrational modes after adsorption of Nafion<sup>®</sup> molecules on metal surfaces, field gradient effects, or the interaction between metal ions and the functional groups present in Nafion<sup>®</sup>.<sup>141,147,149</sup> Other low intensity peaks that are very intense in the Raman spectrum of pure Nafion<sup>®</sup> prior to exposure to

metal solutions, also appear in the spectrum in Figure 45. However, the very low intensity implies that the functional groups corresponding to these peaks have little interaction with the silver ions.<sup>150,151,152,153</sup>

Previously, MOFs have demonstrated high removal efficiencies of metal ions from aqueous solutions.<sup>129,130</sup> Furthermore, Nafion<sup>®</sup> is a prototypical cation conductor where metal ions can exchange with protons at the sulfonic acid groups.<sup>154</sup> For our experiments we observed a significant increase in silver ion adsorption when compared to copper, zinc, and lead for MOF-74(Ni)/Nafion<sup>®</sup>. Out of the four metal ions studied, silver has the highest reduction potential, and can be readily converted to a metal via chemical reduction in MOFs.<sup>155</sup> Although we are not intentionally adding a chemical reductant to the system, it is possible that impurities in the composite facilitate these reduction reactions. Recent studies have shown that metallic silver clusters can be formed in MOFs by *in-situ* reduction of Ag<sup>+</sup> with ethanol.<sup>156</sup> FTIR spectra indicate changes in M-O and C=O stretching modes in the silver loaded MOF samples, and Raman spectra show significant broadening of peaks (similar to what we observed in Figure 45). Our MOF-74(Ni)/Nafion<sup>®</sup> composites are formed with a n-propanol Nafion<sup>®</sup> solution, and potentially this solvent can be trapped in the MOF-74(Ni). This solvent can react with silver ions in the composite, which then leads to the greater silver adsorption capacity for the MOF-74(Ni)/Nafion<sup>®</sup> composite compared to pure Nafion<sup>®</sup>. However, it should also be noted that significant relative mass increases are also observed for Cu<sup>2+</sup> and Pb<sup>2+</sup> in the MOF-74(Ni)/Nafion<sup>®</sup> composites, compared to Nafion<sup>®</sup>. These results suggest that other mechanisms, other than metal cation reduction, leads to the increase in the relative mass increases.

FTIR spectroscopy has previously been used to evaluate the adsorption of  $\text{Hg}^{+2}$  in aqueous solutions by MOF-74(Zn), where peak shifts and peak intensities for hydroxyl and carboxylate groups associated with the organic linkers were monitored.<sup>157</sup> Changes in these peaks suggest the formation of Hg-O bonds which was the primary mechanism for the removal of mercury ions from solution. Lanthanide-based MOFs have been used for the adsorption of lead and copper ions from aqueous solutions.<sup>158</sup> It was suggested that the adsorption mechanism for heavy metals was related to Lewis acid-base interactions between hydroxyl groups and metal ions. Changes in the adsorption capacities for MOFs for different pH values indicates that deprotonation of hydroxyl groups in a basic medium allowed for an increase in the adsorption capacity of metal ions. A decrease in pH was shown to desorb ions from the MOFs and allow for a mechanism to regenerate the MOF particles. Low pH ranges have also been used for the regeneration of Nafion<sup>®</sup> membranes that have been used in adsorption experiments of heavy metals.<sup>159</sup> The adsorption mechanism of metal ions in Nafion<sup>®</sup> is based on interactions between cations and the sulfonic acid groups, where the sulfonic acid groups deprotonate at high pH values. This regeneration mechanism may potentially work for the MOF-74(Ni)/Nafion<sup>®</sup> composites in the current study, however was not tried since structural instabilities of MOFs at low pH values has been observed.<sup>158,160,161,162</sup>

For porous materials there are many parameters that can influence the adsorption capacity for metal ions, including pore size, porosity, surface area, hydrate ionic radius, electronegativity, initial concentration, pH, temperature, and competing ions.<sup>159</sup> MOFs can be chosen where these parameters can be tailored to enhance the

selectivity to a specific metal cation out of a mixture of metal cations. For example, the flexibility in MOF design allows the use of organic linkers that possess chemical functionality to increase the selectivity in adsorption of certain species.<sup>129,163</sup> These changes can be employed to increase the selectivity difference in between the matrix (Nafion<sup>®</sup>) and the MOF particles to a certain adsorbate in a mixture of ions for example.

Future investigations focused on the optimization of MOF/polymer composite chemistries may lead to membranes that improve the selectivity and capacity for the absorption of metal cations from aqueous solutions while maintaining the structural properties of the MOF particles, and may result in promising approaches for water treatment processes.

## Conclusions

MOF-74(Ni) was successfully synthesized using a continuous flow, microwave-assisted reactor with benzoic acid as a chemical modulator. These studies indicated that benzoic acid was an effective modulator, even for very short reaction times. Competing reactions pathways for organic linkers and modulators resulted in an increase in the relative apparent activation energies for higher BA to Ni<sup>2+</sup> concentration ratios. These higher ratios resulted in the formation of larger and more uniform particles, with high reagent conversions. Optimization of the MOF synthesis conditions gave good control of particle size distributions, particles with high crystallinity, and high surface area.

The stability of MOF-74(Ni)/Nafion<sup>®</sup> composites in aqueous solutions with metal ions was confirmed by XRD. ICP-OES results indicated a significant difference between the amount of metal ions adsorbed by MOF-74(Ni)/Nafion<sup>®</sup> composite films compared to Nafion<sup>®</sup> alone. Copper, lead, and silver were removed with high efficiencies by the MOF-74(Ni)/Nafion<sup>®</sup> composite film. Silver was removed with the highest efficiencies due to the formation of silver nanoparticles, which was indicated by Raman spectroscopy. We have demonstrated that MOF-based membranes are a relatively simple approach to remove ions from solutions with high efficiencies.

#### Acknowledgements

The authors gratefully acknowledge Abdulrahman Aldossary, Nick Wannemacher, and Andy Ungerer for initial MOF reaction studies, BET isotherm experiments, and ICP-OES measurements, respectively.

This research was funded by the United States National Science Foundation – Scalable Nanomanufacturing program (Grant CBET-1449383). A portion of this research was performed at the Northwest Nanotechnology Infrastructure, a member of the National Nanotechnology Coordinated Infrastructure, which is supported by the National Science Foundation (Grant ECCS-1542101).

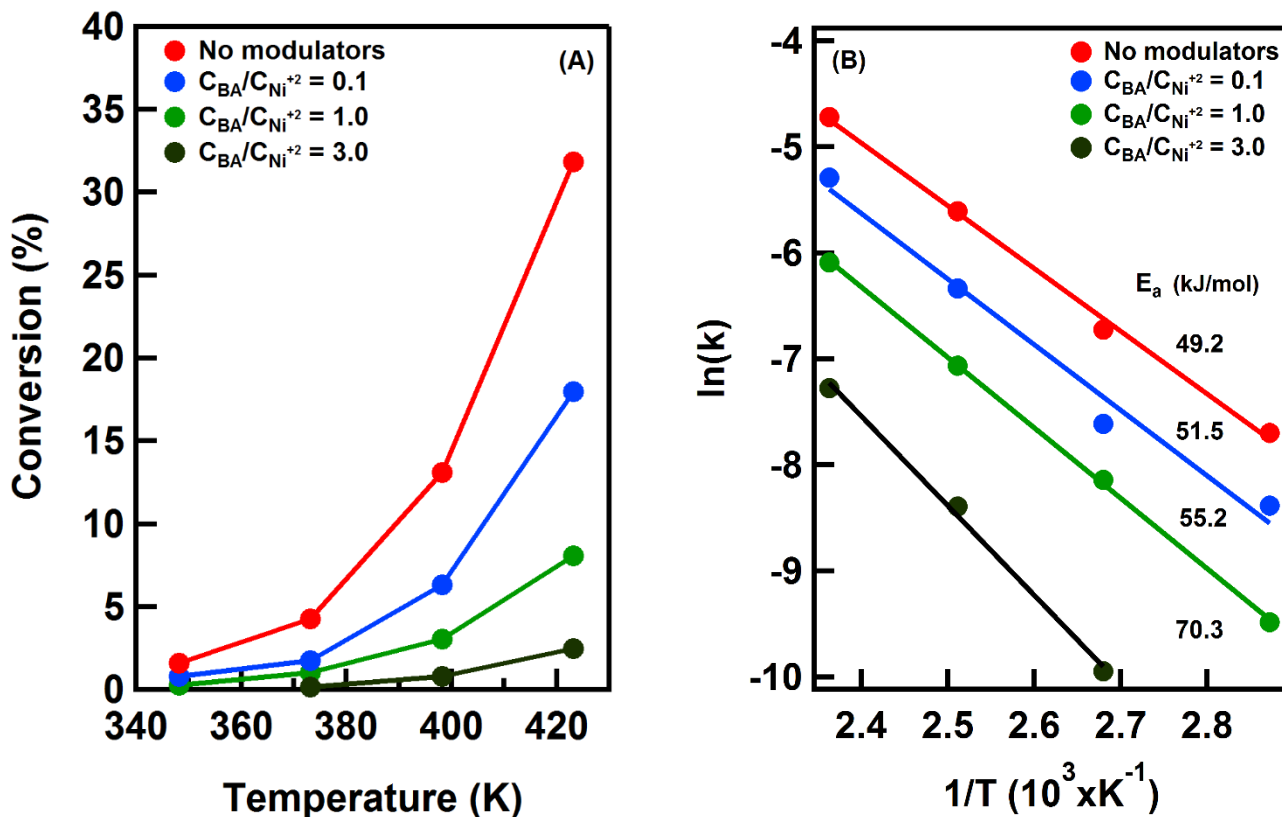


Figure 36: Percent conversion of Ni<sup>2+</sup> for reactions carried out with different microwave temperatures and BA to Ni<sup>2+</sup> concentration ratios (A), and a plot of natural logarithm of the rate constant (k) versus inverse temperature for each BA to Ni<sup>2+</sup> concentration ratios (B), where the estimated activation energies are provided.

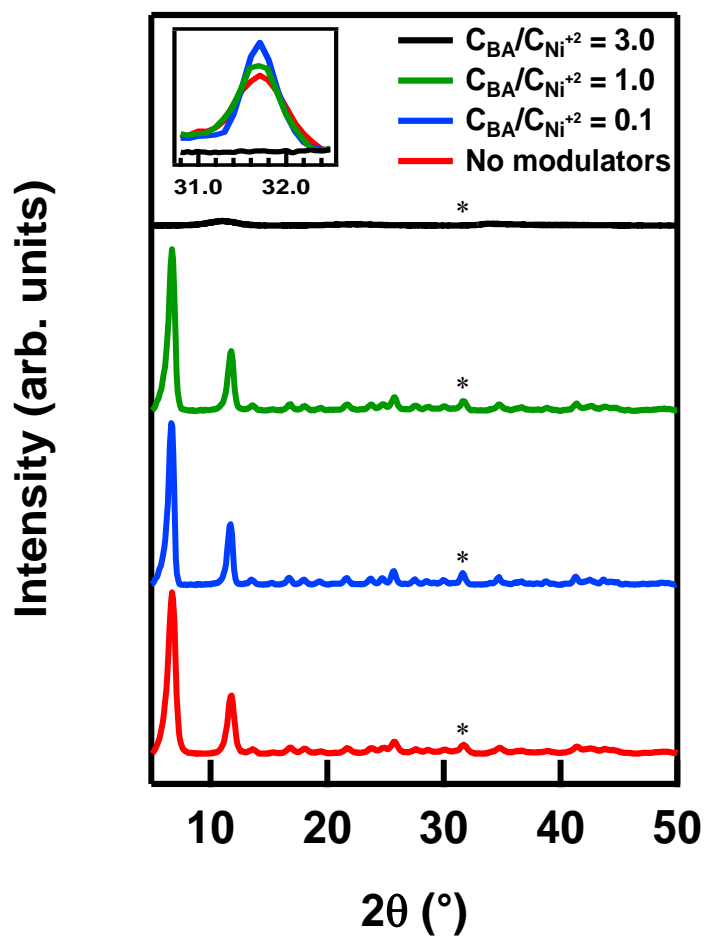


Figure 37: Powder X-ray diffraction of samples synthesized at different BA and Ni<sup>2+</sup> concentration ratios. Inset provides an expanded view of the peak at 31.75 °.

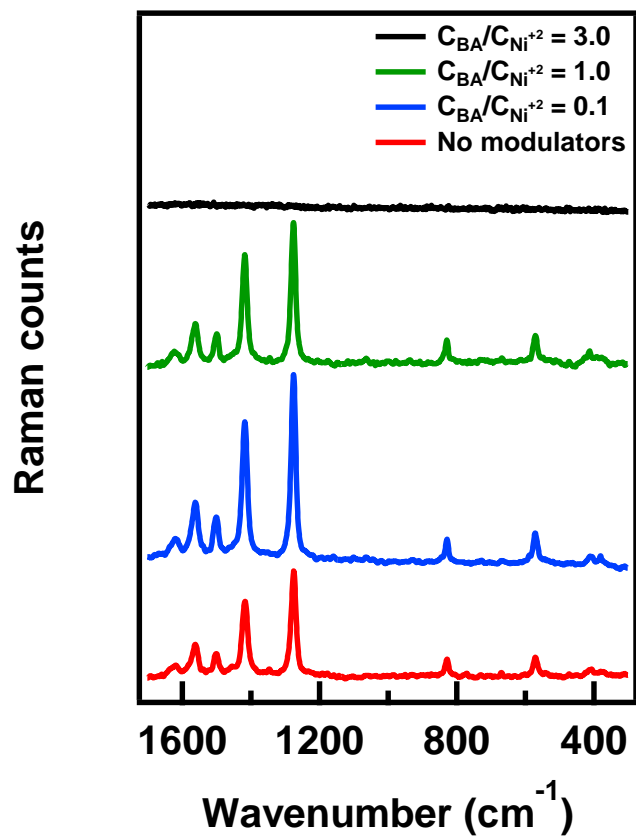


Figure 38: Raman spectroscopy of samples synthesized at different BA and Ni<sup>2+</sup> concentration ratios.

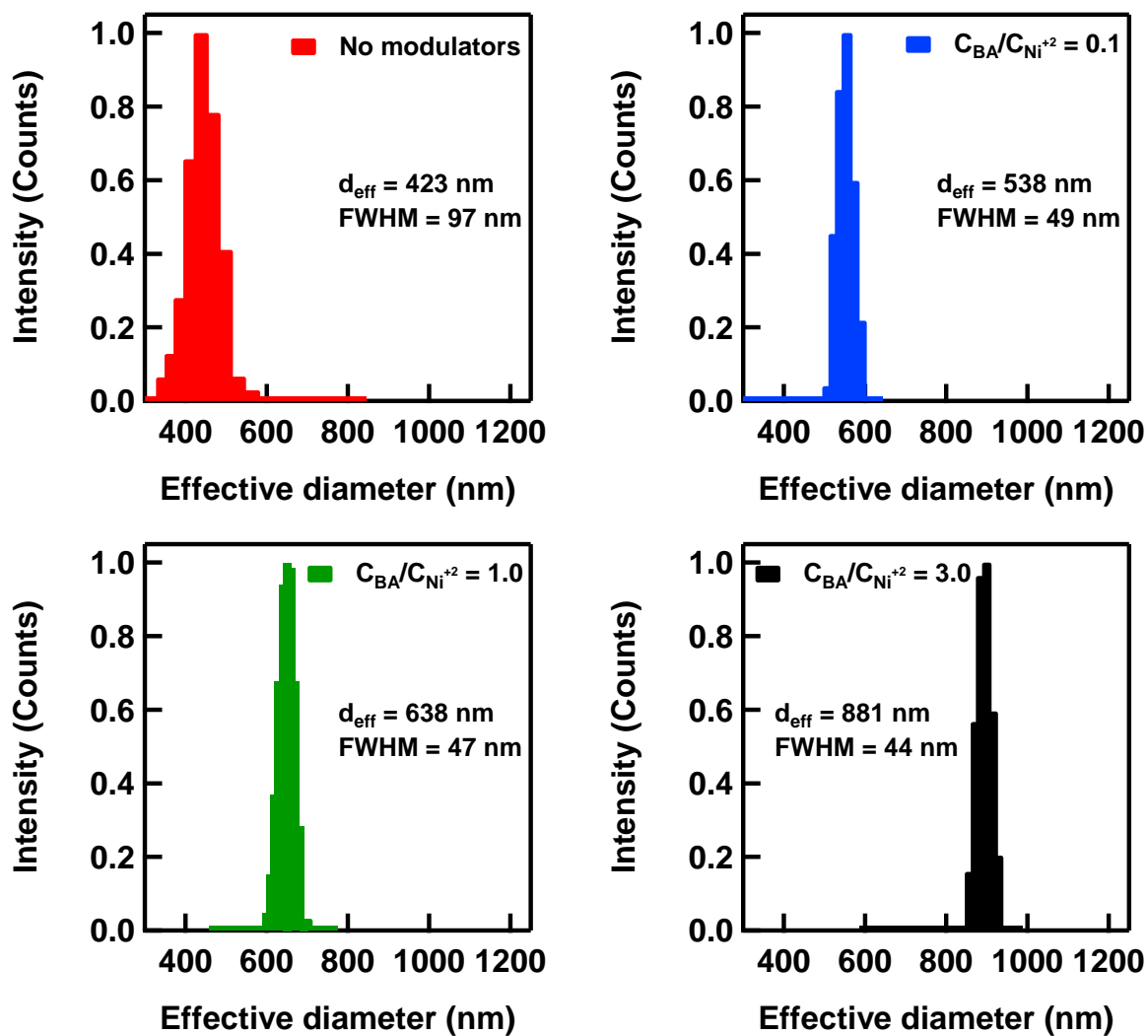


Figure 39: Dynamic light scattering results for samples synthesized at different BA and Ni<sup>2+</sup> concentration ratios.

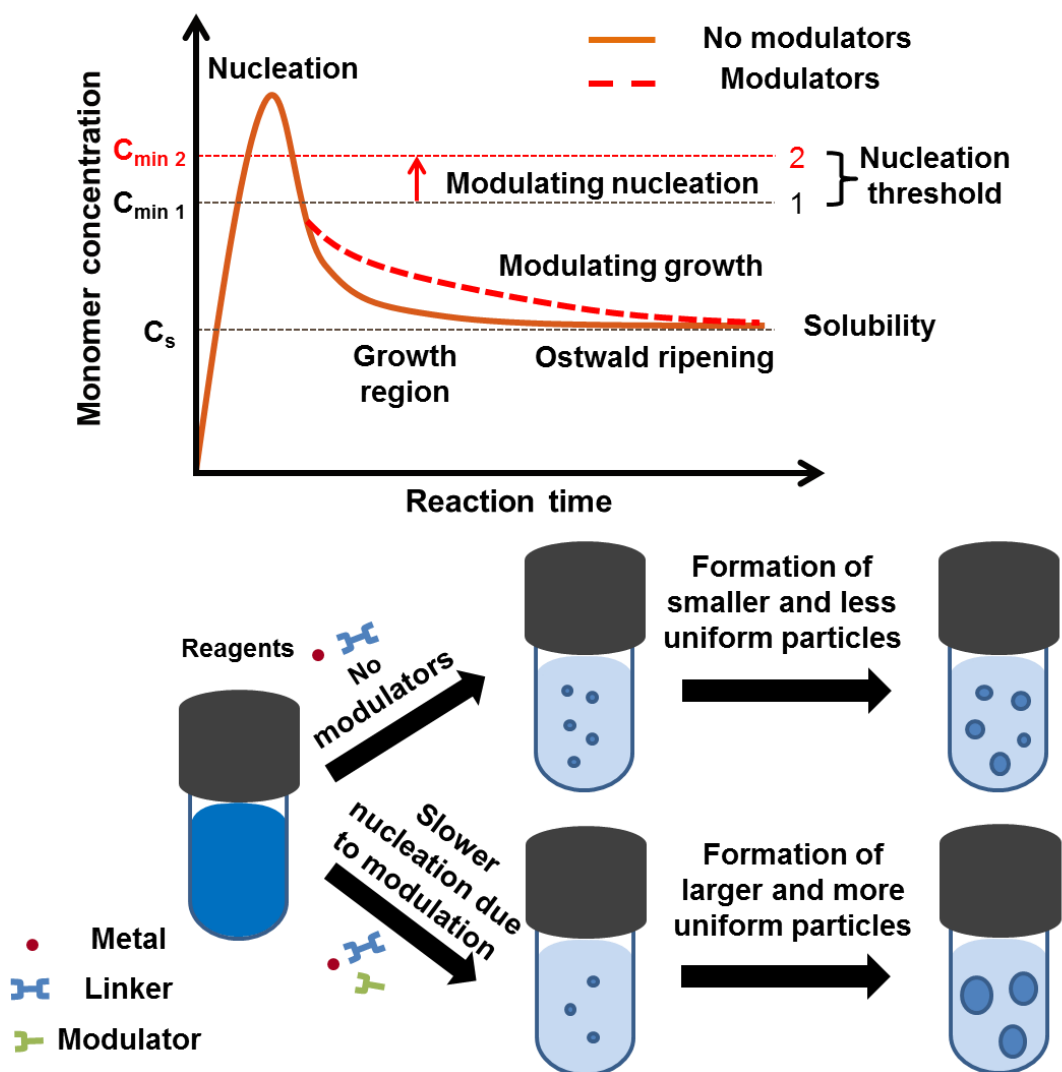


Figure 40: LaMer model<sup>134</sup> and modulating effects in relatively short synthesis of MOFs causing formation of larger and more uniform crystals. (After Diring *et al.*)<sup>117</sup>

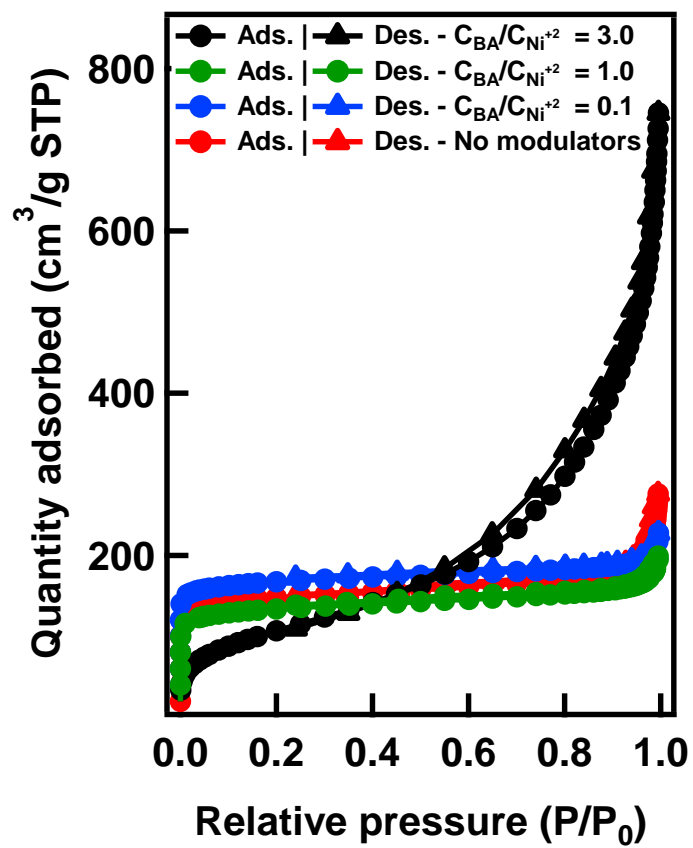


Figure 41: Adsorption (Ads.) and desorption (Des.) cycles of N<sub>2</sub> physisorption isotherms for samples synthesized using different BA and Ni<sup>2+</sup> concentration ratios.

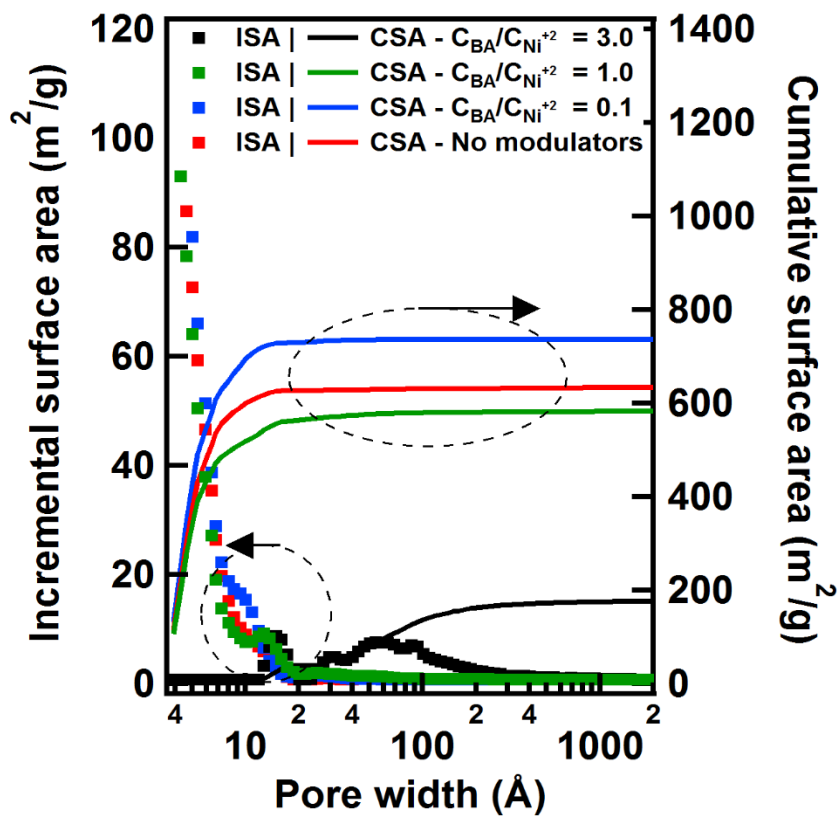


Figure 42: Incremental surface area (ISA) and cumulative surface area (CSA) estimated from N<sub>2</sub> physisorption isotherms for samples synthesized using different BA and Ni<sup>2+</sup> concentration ratios.

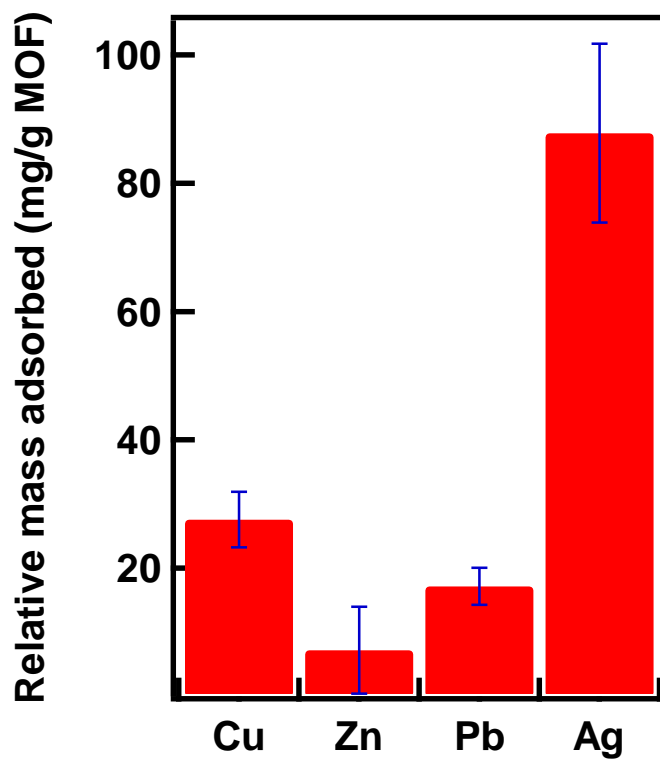


Figure 43: Relative mass of metals adsorbed in MOF-74(Ni)/Nafion® composite films. Relative mass was estimated by the difference in metal wt.% between composite and pure polymer film determined by ICP-OES divided by the amount of MOF estimated in samples.

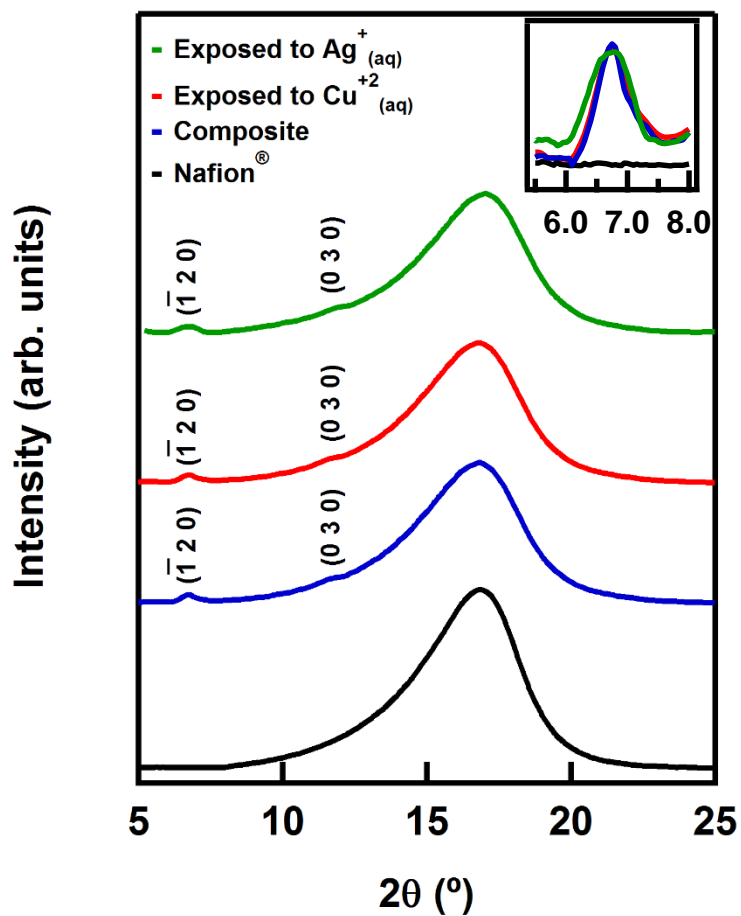


Figure 44 X-ray diffraction of pure polymer (Nafion<sup>®</sup>) and composite films as prepared and after exposure to copper nitrate solution. The exposed sample was representative of other samples exposed to metals. Inset shows the most intense diffraction peak that characterizes the MOF-74(Ni) - interplanar spacing ( $\bar{1}20$ ).

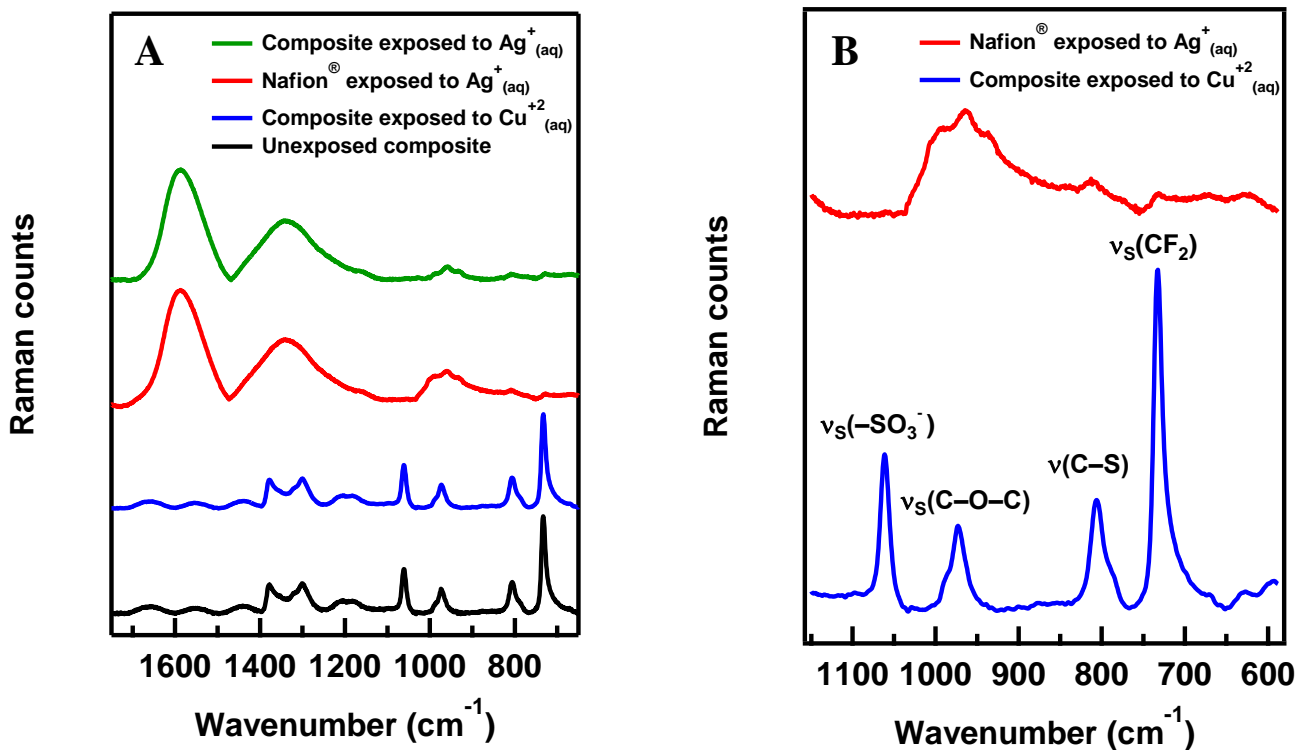


Figure 45: Raman spectra of unexposed composite film, of a composite film after exposure to copper nitrate, and of a composite film after exposure to silver nitrate.

(A) Raman spectra of composite samples exposed to silver and copper nitrate. (B)

Expanded range of composite samples exposed to copper and silver nitrate that shows formation of new peaks for the case in which silver nitrate was used.

## CHAPTER 6

STRUCTURAL AND OPTICAL CHARACTERIZATION OF  $\text{Cu}_3\text{SbS}_4$   
FOR SOLUTION-BASED THIN FILM SOLAR CELLS

Gustavo H. Albuquerque<sup>1</sup>, Ki-Joong Kim<sup>1</sup>, Jonathon I. Lopez<sup>1</sup>, Arun Devaraj<sup>2</sup>,  
Sundeep Manandhar<sup>3</sup>, Yi-Sheng Liu<sup>4</sup>, Chih-hung Chang<sup>1</sup>, and Gregory S. Herman<sup>1,\*</sup>

<sup>1</sup>Oregon State University, School of Chemical, Biological, and Environmental  
Engineering, Corvallis, Oregon, 97331, USA

<sup>2</sup>Physical and Computational Sciences Directorate, Pacific Northwest National  
Laboratory, Richland, Washington, 99354, USA

<sup>3</sup>Environmental Molecular Sciences Laboratory, Pacific Northwest National  
Laboratory, Richland, Washington, 99354, USA

<sup>4</sup>Advanced Light Source, Lawrence Berkeley National Laboratory, Berkeley,  
California, 94720, USA

\* Corresponding author

Manuscript in preparation

## Abstract

The most efficient inorganic thin film chalcogenide-based solar cells use CdTe or CuInGaSe<sub>2</sub> (CIGS) as absorber layers, which rely on toxic (Cd) and/or other scarce elements (In, Te). The desire for more sustainable solar technologies has led to the development of Earth abundant and non-hazardous copper chalcogenide absorber materials. Cu<sub>3</sub>SbS<sub>4</sub> (Famatinite) is a promising Earth abundant p-type semiconductor that has a low band gap (0.9-1.05 eV), high absorption coefficient ( $\alpha \sim 10^4$ - $10^5$  cm<sup>-1</sup>), and has potential as the absorber layer for thin-film solar cells. In this study, we describe a method for synthesizing Cu<sub>3</sub>SbS<sub>4</sub> nanocrystals and the solution-based coating of nanocrystal precursors. Optical and structural characterization was performed after thermal processing the Cu<sub>3</sub>SbS<sub>4</sub> films, where changes in the film due to the annealing conditions were characterized using X-ray diffraction, Raman spectroscopy, electron microscopy, and X-ray absorption near edge structure.

## Introduction

Greenhouse gas emissions, scarcity of minerals, increasing pollution, and global warming have forced changes in the world's energy makeup. Due to increasing demands for cleaner sources of energy, the solar energy production in the U.S. has grown dramatically in the last decade.<sup>164,165</sup> Crystalline silicon (c-Si) is still the major commercial solar cell technology with solar conversion efficiencies of 26.3 %, however other inorganic solar cell technologies have shown promising efficiencies, such as  $\text{Cu}_2\text{ZnSnS}_{4-y}\text{Se}_y$  (12.6 %), CdTe (22.1 %),  $\text{CuIn}_{1-y}\text{Ga}_y\text{Se}_2$  (22.6 %), and GaAs (28.8 %).<sup>166</sup>

The maximum efficiencies for single junction devices is approximately 33.2 %, which is based on the Shockley-Queisser limit.<sup>167</sup> As single junction solar cells approach the Shockley-Queisser limit, other approaches to increase efficiencies are required. One promising approach is the development of multi-junction solar cells, where two or more solar cells with different band gaps are stacked into a single device.<sup>168</sup> Multijunction designs allow more effective absorption of photons from the entire solar spectrum, and consequent an increase in the maximum possible efficiency.

Copper antimony sulfide (CAS), a ternary I-V-VI semiconductor, is composed of relatively inexpensive and abundant elements, which makes it a promising alternative material to CIGS and CdTe.<sup>165</sup> CAS can be synthesized in four major phases including  $\text{CuSbS}_2$  (Chalcostibite),  $\text{Cu}_{12}\text{Sb}_4\text{S}_{13}$  (Tetrahedrite),  $\text{Cu}_3\text{SbS}_3$  (Skinnerite), and  $\text{Cu}_3\text{SbS}_4$  (Famatinite). The bandgap of these four CAS phases can

vary from 0.5 to 2.0 eV which is within the optimal range for high efficiency single junction solar cells.<sup>169</sup> The high absorption coefficient for the  $\text{Cu}_3\text{SbS}_4$  phase in combination with its low band gap ( $\sim 1.0$  eV)<sup>170</sup> makes it a promising material for integration into tandem solar cells.

Higher efficiency solar cells are typically fabricated using vacuum deposition techniques. However, the use of nanoparticle inks to prepare thin film solar cells is considered a cost-effective and promising approach. Several studies have shown functional solar cells for the CAS system but the vacuum deposition methods still have low efficiencies of 0.46 % for sputter deposited  $\text{Cu}_3\text{SbS}_4$ <sup>171</sup> and 0.02 % for an atomic layer deposited  $\text{CuSbS}_2$ .<sup>172</sup> Higher efficiencies of 3.12 % were obtained for spin-coated  $\text{CuSbS}_2$  precursors.<sup>173</sup> Most studies presented so far, have been focusing on different CAS phases and on their structural and optical bulk properties. Therefore, there are opportunities to improve CAS solar cell performance, and to understand what factors lead to the low efficiencies in current CAS solar cells.

The synthesis of uniform colloidal nanoparticles with precise control over composition and optoelectronic properties still has many challenges. The hot-injection method is a promising approach to synthesize uniform nanoparticles, where supersaturation of reagents for a very short time induces rapid formation of nuclei.<sup>174</sup> The combination of rapid nucleation and capping agents lead to the formation of monodisperse, uniform nanoparticles. This study focused on the characterization of the structural, chemical, and optical properties of  $\text{Cu}_3\text{SbS}_4$  films deposited using nanoparticle inks, and the effect of annealing temperature and environment on these properties. CAS films were characterized using Raman and UV-Vis spectroscopy, X-

ray diffraction (XRD), electron microscopy, and X-ray absorption near edge structure (XANES). The ultimate goal of this work was to also use the continuous flow microwave system in the synthesis of  $\text{Cu}_3\text{SbS}_4$  nanoparticles. However, the faster development of the hot injection approach, allowed the use of solution-based deposition techniques and evaluation of the structural and optical behaviors of this phase in the thermal processing that may be part of a solar cell device processing steps.

## Experimental section

**$\text{Cu}_3\text{SbS}_4$  nanocrystals synthesis:** All the reagents used in the synthesis were stored in an  $\text{N}_2$ -filled glove box that kept oxygen and moisture concentrations below 0.5 ppm. Prior to storage the solvents were purged in with  $\text{N}_2$  for 60 min using flasks containing molecular sieves. Copper chloride ( $\text{CuCl}$ , 97 %) and antimony chloride ( $\text{SbCl}_3 \cdot 6\text{H}_2\text{O}$ , 99.5 %) were obtained from Alfa Aesar. Sulfur precipitated powder was obtained from Fisher-Scientific. Chloroform was obtained from J.T. Baker (99.8 %). Oleylamine (OLA,  $\geq 98$  %) and 1-hexanethiol (95 %) were obtained from Sigma-Aldrich.

The synthesis of  $\text{Cu}_3\text{SbS}_4$  nanocrystals was modified from a previously reported method, which uses two separate flasks of reagents.<sup>175</sup> In the first flask, 1.4 mmol of copper chloride and 1.4 mmol of antimony chloride were dissolved in 22 mL of oleylamine. This mixture was heated to 85 °C while being vigorously stirred for about 15 min until the solution became clear. This solution was then transferred to a

three-necked pear-shaped flask. In the second flask, 6.3 mmol of sulfur was added to 8 mL of oleylamine which was heated to 85°C while stirring for about 5 minutes. The three-necked pear-shaped flask containing metal precursors was then connected to a Schlenk line for degassing under low vacuum, followed by purging with high purity Argon. This alternating (degassing/purging) procedure was repeated twice to remove most of the remaining nitrogen. A similar procedure was performed to the sulfur source flask. Finally, the metal precursor flask was heated to 200 °C, at which point the solution from the sulfur source flask was rapidly injected into the metal precursor. The initial temperature was maintained for 30 min. After cooling, about 6 mL of toluene was added to equal volume of product liquor. This liquid was centrifuged at 2400 rpm for 30 minutes and the supernatant was collected and purified using a liquid extraction process with methanol and increasing amounts of acetone. The nanoparticles were crashed with methanol then dispersed in toluene twice before being centrifuged at 4000 rpm in a mixture containing 7 mL of dispersed particles, 1 mL of acetone, and ~ 4 mL of methanol. After the purification steps, the particles were characterized, and preparation of a nanoparticle ink with 20 wt.% CAS in 1-hexanethiol.

**Film deposition and sulfurization process:** The  $\text{Cu}_3\text{SbS}_4$  nanoparticle inks were spin-coated at 3000 rpm for 10 s on 19 mm x 19 mm glass substrates that had a 200 nm Mo coating (Eagle® 2000, 800  $\mu\text{m}$  of thickness) or 20 mm x 20 mm quartz substrates (GM Associates, 1 mm of thickness). The CAS films were annealed in air in two steps: Step 1 was a 180°C anneal for 2 min and step 2 was a 280°C anneal for 10 s. The spin-coating and annealing process was repeated 25 times to obtain films

that were  $\sim 1 \mu\text{m}$  thick. The films were then annealed in a sulfur-rich atmosphere in a tube furnace. The substrates were mounted face down above an alumina crucible containing sulfur powder. The quartz tube (2" diameter) was purged with a 50 mL/min nitrogen flow rate. After one hour the nitrogen flow rate was reduced to 12 mL/min. A 20 min. total temperature ramping time was used for all anneals. Films were characterized within 24 hours of final preparation.

**Characterization:** X-ray diffraction (XRD) was performed using a Rigaku Ultima IV diffractometer ( $\lambda_{\text{Cu-K}\alpha} = 0.1542 \text{ nm}$ , 40 kV, 40 mA). Prior to XRD analysis the nanoparticles were drop casted onto glass slides and the solvent was evaporated in a  $\text{N}_2$  environment. XRD was performed using a fixed X-ray incidence angle ( $\omega = 1.5^\circ$ ). The Raman spectra were obtained using a Horiba-Jobin Yvon HR-800 Raman spectrometer with two different incident laser sources ( $\lambda_1 = 532 \text{ nm}$  and  $\lambda_2 = 785 \text{ nm}$ ). Absorbance measurements were obtained from films deposited on quartz substrates using a Cary 5 UV-Vis-NIR spectrophotometer. Transmission electron microscopy (TEM) and scanning transmission electron microscopy (STEM) images were taken using a FEI Titan FEG with acceleration voltage at 200 kV and a FEI Quanta 600 FEG SEM with 20-30 kV accelerating voltage, respectively. For TEM imaging, samples were prepared from  $\text{Cu}_3\text{SbS}_4$  particles dispersed in a chloroform solution that was sonicated for 2 minutes (Branson model 2510 – Max power 130 W). The solution was then drop casted onto a carbon coated copper grid, which was mounted in the microscope after drying for 5 minutes at  $60^\circ\text{C}$ . Scanning electron microscopy (SEM) imaging and energy dispersive X-ray spectroscopy (EDS) were performed using an FEI Quanta 600 FEG SEM with 5-30 kV accelerating voltage. EDS scans were taken

in 4 different locations on the films and the average and standard deviation are shown in the chemical formula obtained by EDS. The films were cleaved after being frozen in liquid N<sub>2</sub> for cross section images. X-ray near edge structure (XANES) spectroscopy was performed at the Advanced Light Source of the Lawrence Berkeley National Laboratory on Beamline 6.3.1.2. The energy resolution was set to 0.5 eV using a 1200 lines/mm grating. In these experiments the Cu L<sub>3</sub> edge was analyzed and the base pressure of the experimental chamber was below 1x10<sup>-8</sup> Torr. High purity copper metal was used as a reference sample and the spectra were energy corrected by fixing the Cu L<sub>3</sub> edge inflexion point at 932 eV. Data were recorded in total fluorescence yield and total electron yield in order to obtain bulk and surface sensitive information, respectively.

## Results and discussion

In Figure 46 we show an XRD pattern obtained from the as-synthesized nanocrystals. The main XRD peaks were observed at  $2\theta = 29.0^\circ$ ,  $48.3^\circ$ , and  $57.2^\circ$ , which are due to diffraction from the (1 1 2), (2 0 4), and (3 1 2) crystallographic planes for the Cu<sub>3</sub>SbS<sub>4</sub>. No XRD peaks were observed which would indicate the formation of impurity phases, such as copper sulfide, antimony sulfide, and the tetrahedrite CAS phase. This result suggests that the synthetic procedure had high selectivity for the Cu<sub>3</sub>SbS<sub>4</sub> phase nanocrystals.

Transmission electron microscopy was used to characterize the as-synthesized Cu<sub>3</sub>SbS<sub>4</sub> particles, as well as to determine the particle size distribution. Figure 47(A)

shows a single particle high-resolution transmission electron microscopy (HRTEM) image of a  $\text{Cu}_3\text{SbS}_4$  particle. The HRTEM image showed well defined crystallographic planes, where the spacing was estimated to be 0.31 nm which is associated with the (1 1 2) planes. Figure 47(B) shows a selected area electron diffraction (SAED) image, which was obtained from a group of particles. Diffraction spots associated with the (2 1 1), (2 2 4), and (3 2 1) crystallographic planes were observed. These planes also identify that  $\text{Cu}_3\text{SbS}_4$  was the synthesized phase. In addition to crystallographic information, scanning transmission electron microscopy (STEM) was also used to determine the particle size distributions (PSD) shown in Figure 47(C & D). The analysis of this data indicated that the  $\text{Cu}_3\text{SbS}_4$  particles had a 19 nm mean diameter, with a PSD full width of half maximum (FWHM) of 10 nm.

$\text{Cu}_3\text{SbS}_4$  particles capped with oleylamine (OLA) were used to prepare dispersions of nanoparticle inks that were used to spin-coat thin films. After spin-coating, the films were annealed in air to remove the capping agents in order to prevent formation of an insulating layer surrounding the semiconducting particles. As a second step, a higher temperature anneal in a sulfur-rich atmosphere (sulfurization) was used to enhance grain growth.<sup>176</sup>

Figure 48(A) illustrates the structural changes that occurs for the films after several different sulfurization processes. A phase change from  $\text{Cu}_3\text{SbS}_4$  (Famatinite) to  $\text{Cu}_{12}\text{Sb}_4\text{S}_{13}$  (Tetrahedrite) can be determined since the peak at  $2\theta \approx 30^\circ$ , which is characteristic of the (2 2 2) crystallographic plane of  $\text{Cu}_{12}\text{Sb}_4\text{S}_{13}$  phase, increases in intensity. This change was observed for 400 and 450 °C annealing temperatures when 0.3 g of sulfur was used. Several studies have indicated that antimony sulfide

sublimates at high temperatures which results in a phase change from  $\text{Cu}_3\text{SbS}_4$  to  $\text{Cu}_{12}\text{Sb}_4\text{S}_{13}$ .<sup>177,178</sup> The Tetrahedrite phase is metallic, and must be avoided during the thermal processing for solar cell applications.<sup>179</sup> Figure 49 shows a ternary phase diagram for the Cu-Sb-S system, which indicates that excess sulfur for a fixed temperature should result in a chemical potential that favors the formation of  $\text{Cu}_3\text{SbS}_4$ . Therefore, we increased the amount of sulfur during the annealing step, which allowed us to use higher temperatures. This process led to the formation of films that had narrower FWHM for the XRD peaks, suggesting higher crystallinity of the  $\text{Cu}_3\text{SbS}_4$  films. The increase in grain size and crystallinity is important to reduce grain boundaries and defects in the lattice, and ultimately produce films with improved optical and electrical properties. Although, high temperature sulfurization processes increased the crystallinity of films, short anneals were used to avoid formation of  $\text{MoS}_2$ . Using Raman, we found that  $\text{MoS}_2$  formation occurred on exposed Mo on the substrates when we annealed to  $500^\circ\text{C}$  for 30 minutes.

Figure 48(B) shows that using 5 g of S at  $500^\circ\text{C}$  for an annealing time of 10 minutes. The FWHM of the XRD peaks became narrower as the sulfurization process induced formation of larger grains and consequently increased the crystallinity of the prepared films. A closer look at the XRD pattern for both samples showed a minor formation of copper (II) sulfide after the air annealing and after the sulfurization process.

SEM images for the  $\text{Cu}_3\text{SbS}_4$  films are shown in Figure 50 after several sulfurization conditions. Figure 50(A & B) show distinct gaps between  $\text{Cu}_3\text{SbS}_4$  grains, which suggests material loss for anneals  $> 500^\circ\text{C}$  and  $> 30$  min. However,

Figure 50(C) shows no loss occurred for the optimized sulfurization condition (5 g S /500 °C/10 min). When comparing the samples before and after the optimized sulfurization process, the cross-section images in Figure 50(D1 & D2) show the formation of large grains after the sulfurization process. However, even for the optimized conditions of the sulfurization process, a 150 nm layer of small grains and residual carbon from the capping agents remained after the sulfurization process. This issue was minimized as much as possible using both annealing steps in this study. EDS spectra of both films shown in Figure 50 (D) indicated that after the air annealing step and after the subsequent sulfurization step. The composition of the films was determined to be  $\text{Cu}_{3.0\pm 0.02}\text{Sb}_{1.0\pm 0.08}\text{S}_{4.1\pm 0.10}$  and  $\text{Cu}_{3.2\pm 0.10}\text{Sb}_{1.0\pm 0.06}\text{S}_{4.3\pm 0.20}$ , respectively. The EDS results indicate that the composition of the films after sulfurization were both slightly copper and sulfur rich which could be indicating the formation of CuS also shown in the results obtained by XRD.

Along with the structural changes due to the sulfurization process, an increase in the optical absorption properties for  $\text{Cu}_3\text{SbS}_4$  films were also observed. Figure 51 shows absorption for each of the  $\text{Cu}_3\text{SbS}_4$  films before and after the optimal sulfurization process. Both samples have absorption coefficients above  $10^4 \text{ cm}^{-1}$  in the visible regime, and for the sample after sulfurization there was a rapid increase in absorption at the band gap ( $\sim 0.9 \text{ eV}$ ). The sulfurized sample has a high absorption coefficient over a larger range of wavelengths compared to the air annealed sample. The high absorption coefficient and rapid increase in absorption is of interest for solar cell applications since  $\text{Cu}_3\text{SbS}_4$  can absorb longer wavelengths when used as the bottom absorbing layer of a tandem device based on silicon.

Raman spectroscopy results are shown in Figure 52. For this technique, two different wavelengths were used in order to explore the effect of penetration depth to characterize both films. The peaks located at  $247.2\text{ cm}^{-1}$ ,  $272.5\text{ cm}^{-1}$ ,  $322.5\text{ cm}^{-1}$ ,  $360\text{ cm}^{-1}$ , and  $641.1\text{ cm}^{-1}$  in the Raman spectra of films using a visible laser ( $\lambda = 532\text{ nm}$ , low penetration depth) were used to identify the  $\text{Cu}_3\text{SbS}_4$  phase. When the IR laser was used ( $\lambda = 785\text{ nm}$ , high penetration depth) additional peaks that are characteristic of the  $\text{Cu}_3\text{SbS}_4$  phase were identified ( $271.5\text{ cm}^{-1}$ ,  $317.2\text{ cm}^{-1}$ ,  $348.7\text{ cm}^{-1}$ , and  $629.2\text{ cm}^{-1}$ ). However, for the visible excitation source, a low intensity peak was found at  $493.3\text{ cm}^{-1}$ , which indicates the formation of copper (II) sulfide. This observation is consistent with the XRD analysis. For Raman, no peaks for copper sulfide were observed when longer wavelengths were used (longer penetration depth).

XANES was used to evaluate the bulk and the surface of the  $\text{Cu}_3\text{SbS}_4$  samples. Figure 53 shows XANES for  $\text{Cu}_3\text{SbS}_4$  samples from the fluorescence and the total electron yield detectors. A major difference between the two samples was observed at the pre-edge peak, located at approximately 931 eV. In the figure we also show results for reference samples that have different Cu oxidation states.  $\text{Cu}^0$ ,  $\text{Cu}^+$ , and  $\text{Cu}^{2+}$ , which have the electronic configurations  $(\text{Ar})3d^{10}4s^1$ ,  $(\text{Ar})3d^{10}4s^0$ , and  $(\text{Ar})3d^94s^0$ , respectively. For higher oxidation states the partial occupation of the “d” orbitals allows absorption of X-rays due to 2p-3d transitions.<sup>180</sup> Therefore, the pre-edge peak found at 931 eV should only be observed for samples containing  $\text{Cu}^{2+}$  species. The  $\text{Cu}_3\text{SbS}_4$  samples had a Cu  $L_3$  pre-edge peak in both detection modes, due to the presence of  $\text{Cu}^{2+}$  species. Therefore, CuS is likely present in both the bulk and surface of the  $\text{Cu}_3\text{SbS}_4$  films as a result of multiple air annealing steps that were

performed for the samples. However, the sample that underwent the optimal sulfurization process only had  $\text{Cu}^+$  in the bulk and a much lower  $\text{Cu}^{2+}$  intensity using the total electron yield mode. This suggests that only the surface of films after the sulfurization process contained CuS. As mentioned previously, the  $\text{Cu}_3\text{SbS}_4$  absorbing layer solar cell devices have low efficiencies, which are close to 0.50 %.<sup>171</sup> These lower efficiencies could be caused by the changes in the composition of the films in the bulk and at the surface after the imposed thermal processing. Inhomogeneity, growth orientation effects, and interface structural and electronic properties are of fundamental contribution to the efficiencies of solar cell devices.<sup>181</sup> The presence of CuS due to decomposition of the  $\text{Cu}_3\text{SbS}_4$  phase during the thermal annealing processes was detected by XANES and XRD, and these changes could be the main reasons why lower efficiencies of  $\text{Cu}_3\text{SbS}_4$  devices have been reported.

## Conclusions

In summary, the  $\text{Cu}_3\text{SbS}_4$  phase thin films were successfully treated in a sulfur-rich atmosphere anneal, which resulted in films of higher crystallinity using relatively economical deposition and processing methods. An optimization of a sulfurization process was performed in order to increase crystallinity of  $\text{Cu}_3\text{SbS}_4$  films without a major change of crystal phase. Small changes in the stoichiometric ratio were observed as films were thermally processed and bulk characterization techniques like XRD and Raman spectroscopy revealed that  $\text{Cu}_3\text{SbS}_4$  and CuS were present in samples. SEM images corroborated the formation of larger grains in films

that were treated at the optimal operating conditions of sulfurization. The UV-Vis spectroscopy results indicated that the sulfurization process also increased the absorption coefficients of films in the visible and near-IR range.

XANES spectra revealed that after the air annealing process the  $\text{Cu}_3\text{SbS}_4$  films contained  $\text{Cu}^{2+}$  in both the bulk material and at the surface of the film, which corroborates with EDS metal ratios and the impurity peaks observed in XRD and Raman spectroscopy. However, after the sulfurization process at the optimal conditions the only remaining  $\text{Cu}^{2+}$  was detected by the total electron yield detector, which indicates the formation of  $\text{CuS}$  at the surface of these films. The observed structural and composition changes at the surface level can affect the interface of solar cell devices. These findings could be related to the low efficiencies of  $\text{Cu}_3\text{SbS}_4$  solar cells found so far.

#### Acknowledgments

This research was funded by the United States National Science Foundation – Scalable Nanomanufacturing program (Grant CBET-1449383). A portion of this research was performed at the Northwest Nanotechnology Infrastructure, a member of the National Nanotechnology Coordinated Infrastructure, which is supported by the National Science Foundation (Grant ECCS-1542101). This material is also based upon work also supported by the National Science Foundation via the Major Research Instrumentation (MRI) program under Grant No. 1040588. We also acknowledge the Murdock Charitable Trust and the Oregon Nanoscience and Microtechnologies Institute (ONAMI) for their financial contributions towards the OSU Titan TEM. The

XANES portion of this work used resources of the Advanced Light Source, which is a DOE Office of Science User Facility under contract no. DE-AC02-05CH11231. That was a part of an approved program beamline user proposal at Advanced Light Source which was established through chemical imaging initiative, an LDRD program at PNNL. The XANES experiments were conducted at beamline 6.3.1.2 in the ALS facility at Lawrence Berkeley National Laboratory. We acknowledge Dr. Yi-Sheng Liu and Dr. Jinghua Guo for their assistance with the XANES experiments.

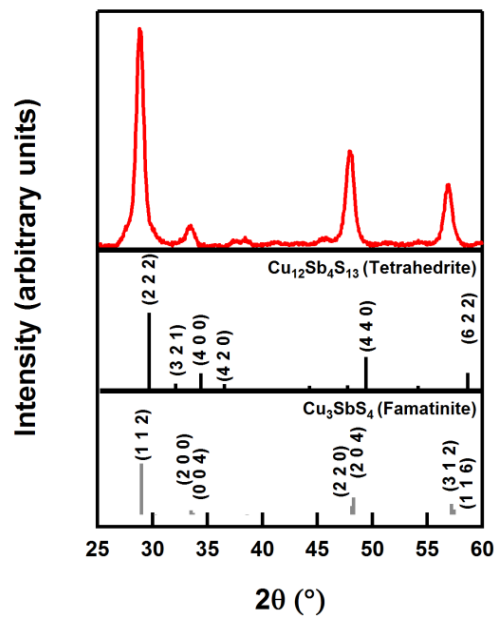


Figure 46: X-ray diffraction pattern of as-synthesized  $\text{Cu}_3\text{SbS}_4$  nanoparticles. Patterns for  $\text{Cu}_{12}\text{Sb}_4\text{S}_{13}$ <sup>182</sup> and  $\text{Cu}_3\text{SbS}_4$ <sup>183</sup> were published elsewhere.

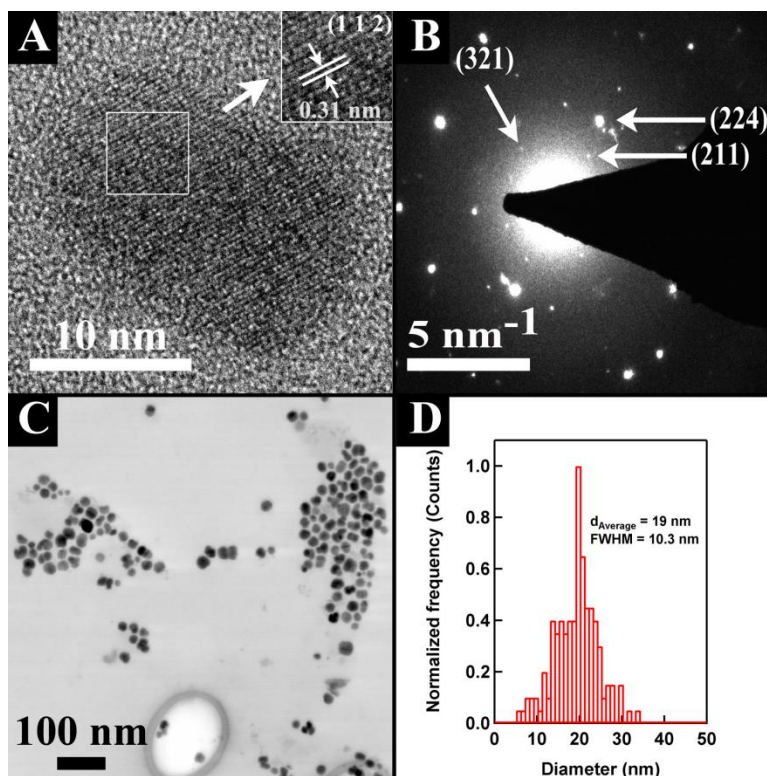


Figure 47: (A) HRTEM image of single  $\text{Cu}_3\text{SbS}_4$  particle, (B) SAED of a group of  $\text{Cu}_3\text{SbS}_4$  particles, (C) STEM image of as synthesized  $\text{Cu}_3\text{SbS}_4$  particles, and (D) Particle size distribution obtained using the STEM image shown in (C)

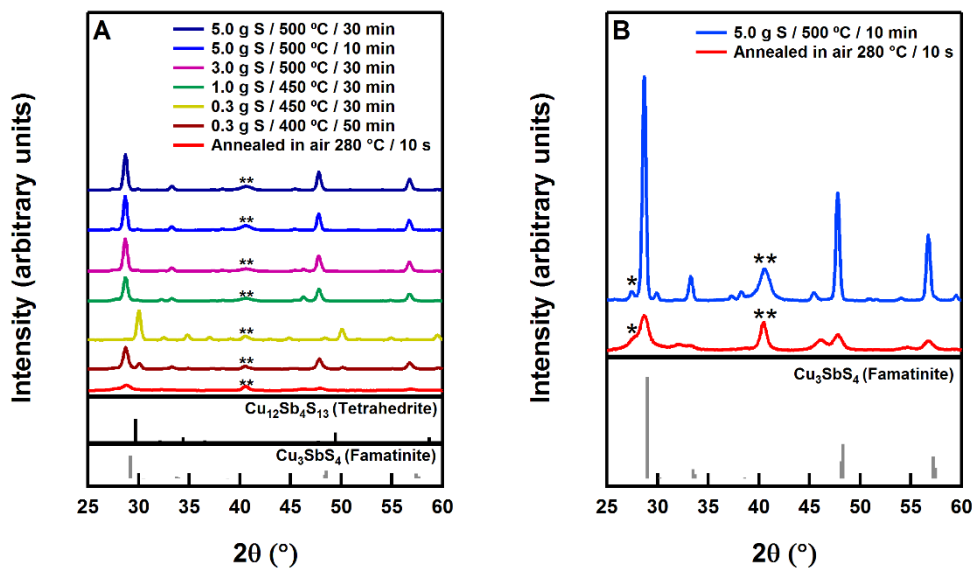


Figure 48: (A) X-ray diffraction of  $\text{Cu}_3\text{SbS}_4$  films after air anneal only and after air anneal followed by different conditions of sulfurization. (B) X-ray diffraction of film prepared at optimized sulfurization condition and air anneal only. Labeled peaks: (\*) CuS and (\*\*) Mo. Patterns for  $\text{Cu}_{12}\text{Sb}_4\text{S}_{13}$ <sup>182</sup> and  $\text{Cu}_3\text{SbS}_4$ <sup>183</sup> were published elsewhere.

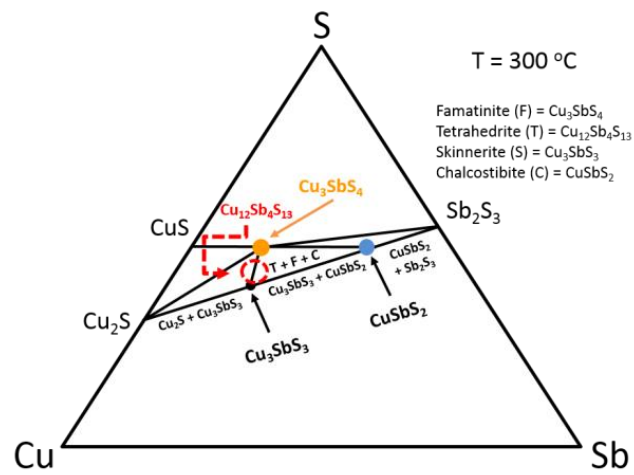


Figure 49: Ternary diagram for Cu, Sb, and S showing regions of formation of binary and ternary phases that can be formed at  $T = 300 \text{ }^\circ\text{C}$ .<sup>184,185</sup> (After Braga *et al.*)

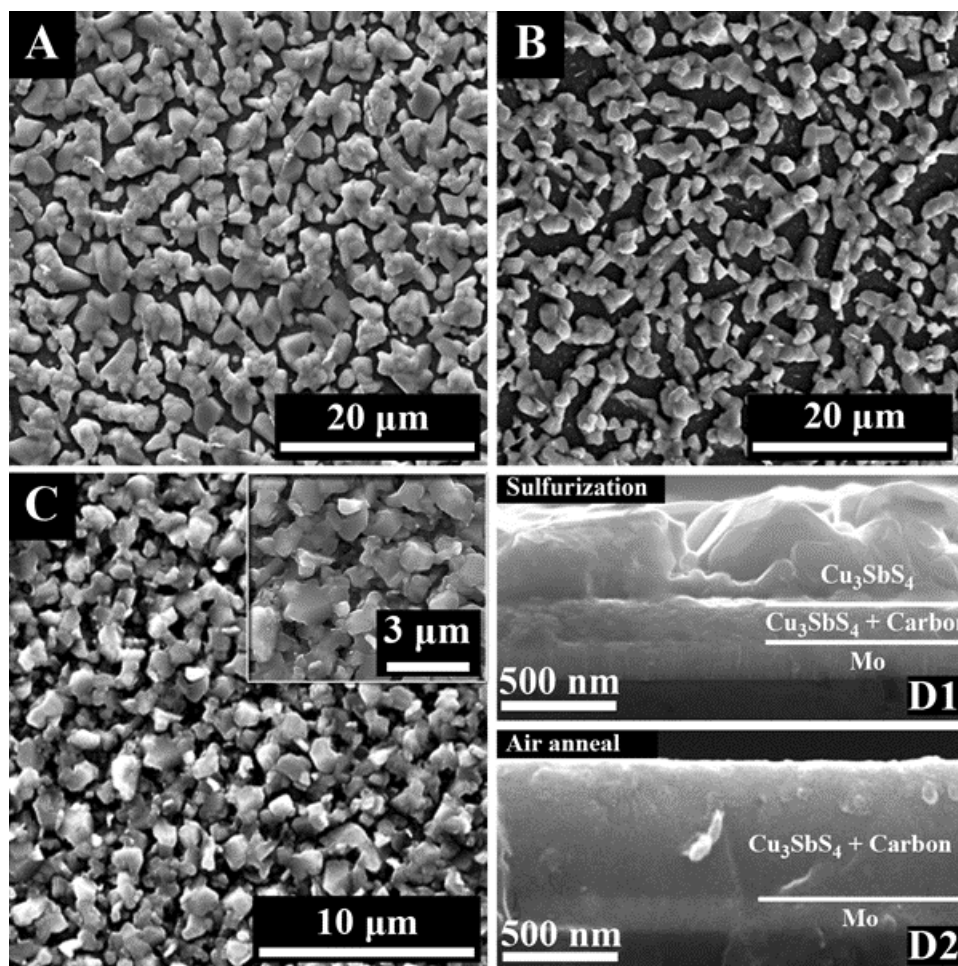


Figure 50: (A) Top-view SEM image of  $\text{Cu}_3\text{SbS}_4$  film that underwent sulfurization at  $500^\circ\text{C}$  / 50 min, (B) Top-view SEM image of  $\text{Cu}_3\text{SbS}_4$  film that underwent sulfurization at  $550^\circ\text{C}$  / 30 min, (C) Top-view SEM image of  $\text{Cu}_3\text{SbS}_4$  film that underwent sulfurization at  $500^\circ\text{C}$  / 10 min, (D1) Cross-section SEM image of  $\text{Cu}_3\text{SbS}_4$  film that underwent sulfurization at  $500^\circ\text{C}$  / 10 min, and (D2) Cross-section SEM image of  $\text{Cu}_3\text{SbS}_4$  film that was only annealed in air.

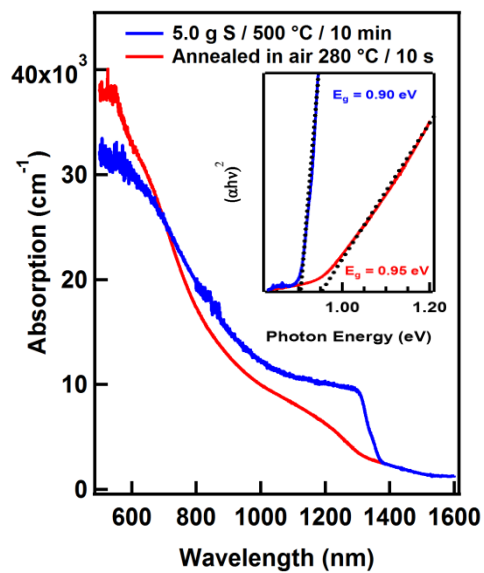


Figure 51: UV-Vis spectroscopy of films annealed in air only and annealed in air along with undergoing the optimized sulfurization process.

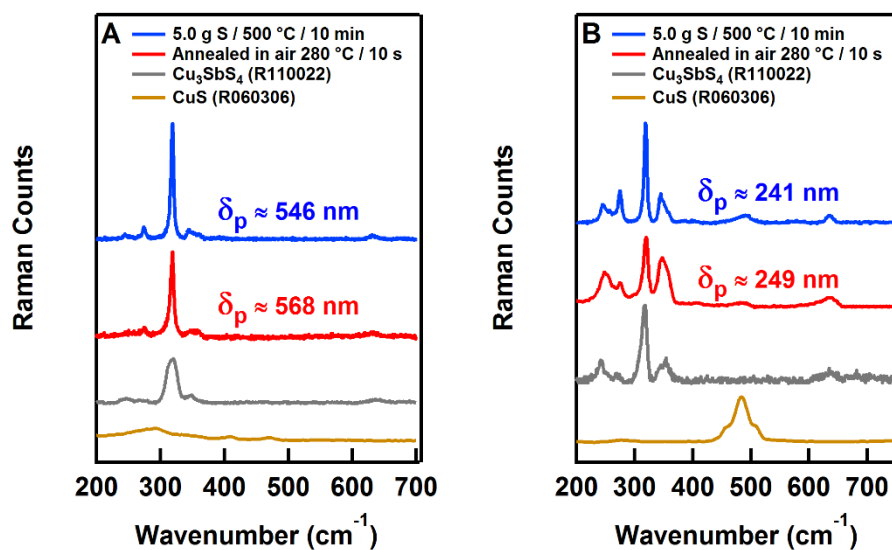


Figure 52: Raman spectroscopy (A) using  $\lambda = 785$  nm laser and (B) using  $\lambda = 532$  nm laser. Samples analyzed were films annealed in air only and annealed in air along with undergoing the optimal sulfurization process.  $\delta_p$  is the estimated penetration depth calculated based on the absorption coefficient of each sample. Reference spectra are part of the RRUFF database: Famatinite (ID: R110022) and Covellite (ID: R060306)

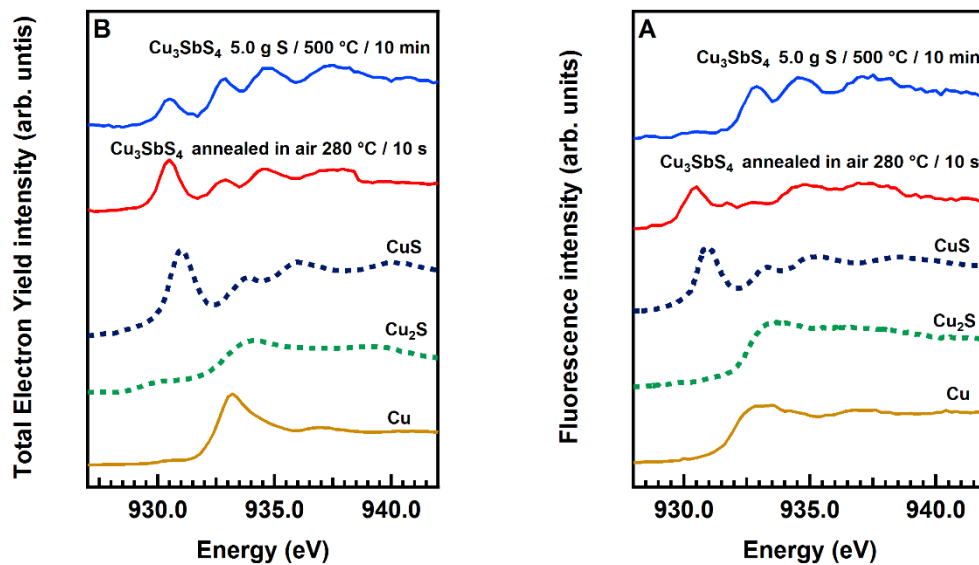


Figure 53: X-ray Absorption Near-Edge Structure (XANES) of films after the air annealing process only and of films after the air annealing process and the following optimal sulfurization process. (A) XANES results from the fluorescence detector and (B) XANES results from the detection of total electron yield. References shown in dashed lines were published elsewhere.<sup>180,186</sup>

## CHAPTER 7

### CONCLUSIONS AND FUTURE DIRECTIONS

In the presented chapters, the scalable synthesis of nanoparticles and the use of nanoparticle inks for the solution-based processing of solar cells has been explored. The continuous flow microwave-assisted synthesis of nanomaterials was successfully performed for different nanomaterials. MOF-74(Ni) was synthesized under milder conditions of pressure ( $\sim 2.5$  bar) with high conversion of reagents ( $\sim 96.5\%$ ) and high space-time yield ( $\sim 80 - 90 \text{ g}\cdot\text{h}^{-1}\cdot\text{L}^{-1}$ ) compared to continuous synthesis with conventional heating sources. Microwaves reduced reaction times down to minutes, as opposed to days in a batch synthesis, and allowed control of nucleation rates. The faster nucleation at higher  $T_{\text{MW}}$  resulted in the formation of smaller grains, which resulted in different adsorption behavior even after the growth bath. Different adsorption behavior was also observed at higher microwave temperatures. This behavior is attributed to the agglomeration of grains and the formation of structural defects, which may result in misaligned and collapsed pores.

The use of benzoic acid as a chemical modulator in the MOF-74(Ni) was proposed as a solution for the agglomeration observed at higher microwave temperatures. The modulation in the synthesis of the MOF-74(Ni) created competing reactions pathways for organic linkers and modulators, and there was an observed increase in the relative apparent activation energies for the MOF-74(Ni) reaction as higher BA to  $\text{Ni}^{2+}$  concentration ratios were used. As a result, synthesis with higher BA to  $\text{Ni}^{2+}$  concentration ratios led to larger and more uniform particles. Optimization of the MOF synthesis conditions allowed for good control of particle size distributions, the formation of particles with high crystallinity, and the formation of particles with high surface area.

The high adsorption capacities of the MOF-74(Ni) and resistance in presence of moisture were tested in a water purification test. ICP-OES results indicated a significant difference between the amount of metal ions present in MOF-74(Ni)/Nafion<sup>®</sup> composite films compared to Nafion<sup>®</sup> alone. Copper, lead, and silver were removed with high efficiencies by the MOF-74(Ni)/Nafion<sup>®</sup> composite film. Silver was the most efficiently removed metal, where Raman spectroscopy indicated this was due to the formation of silver nanoparticles. A scalable method to produce MOF-74(Ni) with excellent control over particle sizes was demonstrated. The synthesized particles were used in a composite in a water purification application showing the removal of metal ions from aqueous solutions. It is suggested that this work would be complemented with regeneration studies of the prepared composites, as well as mechanistic investigations into the amplification of selectivity for more hazardous metal ions.

We developed a scalable synthetic method to create silver nanocubes with high cube selectivities using microwave-assisted methods. Due to surface-enhanced Raman scattering (SERS) effects, nanocubes have important applications in sensing experiments. Different synthesis conditions were varied to yield nanocubes of 28, 45, and 58 nm edge lengths. The optimization of the reactor led to routes for producing particles with cubic-shape selectivity above 70% and narrow size distribution for the cubes of smaller edge length (28 and 45 nm). Further development can use this method to achieve the formation of silver nanocubes with smaller diameters than 15 nm and explore the potential enhancement in sensitivity caused by SERS.

A method for solution-based processing to synthesize and characterize  $\text{Cu}_3\text{SbS}_4$  thin films, a low band gap and superabsorbing material, was successfully developed. This work presented a cost-effective approach in preparing  $\text{Cu}_3\text{SbS}_4$  films, which allowed a study to address structural changes that could be related to the low efficiencies presented by of solar cells using this phase. An optimization of a sulfurization process allowed for an increase in the crystallinity of  $\text{Cu}_3\text{SbS}_4$  films without a major change of crystalline phase. Changes in the stoichiometric ratio of the films were observed through the thermal processing. Bulk characterization techniques such as XRD and Raman spectroscopy revealed that  $\text{Cu}_3\text{SbS}_4$  and  $\text{CuS}$  were present in samples. XANES revealed changes in the oxidation state of copper in the bulk and at the surface level of the films. XANES combined with total electron yield detection further demonstrated the presence of  $\text{Cu}^{2+}$  after the optimized sulfurization process, which indicates the possible formation of  $\text{CuS}$  at the surface of these films. Further studies using XPS are suggested to confirm the observed changes in the XANES spectra. This information could be useful in the optimization of annealing steps so as to avoid the formation of copper sulfide via prevention of the sublimation reactions of antimony sulfide. These studies could lead to the enhancement of efficiencies of solar cell devices that use  $\text{Cu}_3\text{SbS}_4$  as an absorbing layer.

## BIBLIOGRAPHY

---

<sup>1</sup> W. J. Stark, P. R. Stoessel, W. Wohlleben and A. Hafner, *Chem Soc Rev*, 2015, **44**, 5793–5805.

<sup>2</sup> Polte, *CrystEngComm*, 2015, **17**, 6809–6830.

<sup>3</sup> R. Becker and W. Doring, Kinetic treatment of germ formation in supersaturated vapour, *Ann. Phys.*, 1935, **24**, 719–752.

<sup>4</sup> V. K. LaMer and R. H. Dinegar, *J. Am. Chem. Soc.*, 1950, **72**, 4847–4854.

<sup>5</sup> S. G. Kwon and T. Hyeon, *Small*, 2011, **7**, 2685–2702.

<sup>6</sup> E. C. Vreeland, J. Watt, G. B. Schober, B. G. Hance, M. J. Austin, A. D. Price, B. D. Fellows, T. C. Monson, N. S. Hudak, L. Maldonado-Camargo, A. C. Bohorquez, C. Rinaldi and D. L. Huber, *Chem. Mater.*, 2015, **27**, 6059–6066.

<sup>7</sup> T. N. Glasnov and C. O. Kappe, *Chem. - Eur. J.*, 2011, **17**, 11956–11968.

<sup>8</sup> A. Ruditskiy and Y. Xia, *J. Am. Chem. Soc.*, 2016, **138**, 3161–3167.

<sup>9</sup> Y. Wang, Y. Zheng, C. Z. Huang and Y. Xia, *J. Am. Chem. Soc.*, 2013, **135**, 1941–1951.

<sup>10</sup> K. Ramasamy, H. Sims, W.H. Butler, A. Gupta, *Chem. Mater.*, 2014, **26**, 2891–2899.

<sup>11</sup> F. Zagury, The Color of the sky. *Atmospheric Clim. Sci.*, 2012, **2**, 510–517.

<sup>12</sup> M. Birkholz, Principles of X-ray diffraction, in: M. Birkholz (Editor), *Thin Film Analysis by X-Ray Scattering*, Wiley-VCH Verlag GmbH & Co. KGaA, Weinheim, 2006.

<sup>13</sup> I. Langford and A. J. C. Wilson, *J. Appl. Crystallogr.*, 1978, **11**, 102–113.

- 
- <sup>14</sup> M. Williams and C. B Carter, *Transmission Electron Microscopy – Part 1: Basics*, Springer, 2009.
- <sup>15</sup> J. Goldstein, D. Newbury, D. Joy, C. Lyman, P. Echlin, E. Lifshin, L. Sawyer, J. Michael. *Scanning electron microscopy and X-ray Microanalysis*. Springer, 2008.
- <sup>16</sup> J. Tauc, R. Grigorovici, and A. Vancu, Optical properties and electronic structure of amorphous germanium, *Phys. Status Solidi* **15**, 627–637 (1966).
- <sup>17</sup> Brunauer, L. S. Deming, W. E. Deming and E. Teller, *J. Am. Chem. Soc.*, 1940, **62**, 1723–1732.
- <sup>18</sup> Wiley, B.J., Im, S.H., Li, Z.-Y., McLellan, J., Siekkinen, A., Xia, Y.. *J. Phys. Chem. B*, 2006, **110**, 15666–15675.
- <sup>19</sup> Yockell-Lelièvre, H., Lussier, F., Masson, J.-F.. *J. Phys. Chem. C*, 2015, **119**, 28577–2858.
- <sup>20</sup> Zhang, X., Xia, Z., Huang, Y., Jia, Y., Sun, X., Li, Y., Li, X., Wu, R., Liu, A., Qi, X., Wang, S., Wen. *Sci. Rep.*, 2016, **6**, 31404.
- <sup>21</sup> Lee, K.-S., El-Sayed, M.A. *J. Phys. Chem. B*, 2006, **110**, 19220–19225.
- <sup>22</sup> Sangaru, S.S., Zhu, H., Rosenfeld, D.C., Samal, A.K., Anjum, D., Basset, J.-M. *ACS Appl. Mater. Interfaces*, 2015, **7**, 28576–28584.
- <sup>23</sup> Christopher, P., Xin, H., Linic, S.. *Nat. Chem.*, 2011, **3**, 467-472.
- <sup>24</sup> Herrera, G., Padilla, A., Hernandez-Rivera, S. *Nanomaterials*, 2013, **3**, 158–172.
- <sup>25</sup> Atwater, H.A., Polman, A. *Nat. Mater.*, 2010, **9**, 205–213.
- <sup>26</sup> McLellan, J. M., Siekkinen, A., Chen, J. & Xia, Y. *Chem. Phys. Lett.*, 2006, **427**, 122–126.

- 
- <sup>27</sup> R. Kodiyath, S. T. Malak, Z. A. Combs, T. Koenig, M. A. Mahmoud, M. A. El-Sayed and V. V. Tsukruk, *J. Mater. Chem. A*, 2013, **1**, 2777.
- <sup>28</sup> Han, H. J., Yu, T., Kim, W.-S. & Im, S. H., *J. Cryst. Growth*, 2016.
- <sup>29</sup> Im, S. H., Lee, Y. T., Wiley, B. & Xia, Y. *Angew. Chem. Int. Ed.*, 2005, **44**, 2154–2157.
- <sup>30</sup> Khodashenas, B. & Ghorbani, H. R. *Arab. J. Chem.*, 2015.
- <sup>31</sup> M. Nishioka, M. Miyakawa, H. Kataoka, H. Koda, K. Sato and T. M. Suzuki, *Nanoscale*, 2011, **3**, 2621.
- <sup>32</sup> Ruditskiy, A. & Xia, Y. *J. Am. Chem. Soc.*, 2016, **138**, 3161–3167.
- <sup>33</sup> Horikoshi, S. & Serpone, N. *Microwaves in Nanoparticle Synthesis: Fundamentals and Applications*. Wiley-VCH, 2013.
- <sup>34</sup> Albuquerque, G. H. & Herman, G. S.. *Cryst. Growth Des.*, 2017, **17**, 156–162.
- <sup>35</sup> R. C. Fitzmorris, R. P. Oleksak, Z. Zhou, B. D. Mangum, J. N. Kurtin and G. S. Herman, *J. Nanoparticle Res.*, 2015, **17**.
- <sup>36</sup> G. H. Albuquerque, R. C. Fitzmorris, M. Ahmadi, N. Wannemacher, P. K. Thallapally, B. P. McGrail and G. S. Herman, *CrystEngComm*, 2015, **17**, 5502–5510.
- <sup>37</sup> K.-J. Kim, R. P. Oleksak, E. B. Hostetler, D. A. Peterson, P. Chandran, D. M. Schut, B. K. Paul, G. S. Herman and C.-H. Chang, *Cryst. Growth Des.*, 2014, **14**, 5349–5355.
- <sup>38</sup> E. B. Hostetler, K.-J. Kim, R. P. Oleksak, R. C. Fitzmorris, D. A. Peterson, P. Chandran, C.-H. Chang, B. K. Paul, D. M. Schut and G. S. Herman, *Mater. Lett.*, 2014, **128**, 54–59.
- <sup>39</sup> Sosa, I. O., Noguez, C. & Barrera, R. G., *J. Phys. Chem. B*, 2003, **107**, 6269–6275.

- 
- <sup>40</sup> A.R. Siekkinen, J.M. McLellan, J. Chen, Y. Xia, *Chem. Phys. Lett.*, 2006, **432**, 491–496.
- <sup>41</sup> D. Yu and V. W.-W. Yam, *J. Am. Chem. Soc.*, 2004, **126**, 13200–13201
- <sup>42</sup> Y. Wang, Y. Zheng, C. Z. Huang and Y. Xia, *J. Am. Chem. Soc.*, 2013, **135**, 1941–1951
- <sup>43</sup> R. J. Kuppler, D. J. Timmons, Q.-R. Fang, J.-R. Li, T. A. Makal, M. D. Young, D. Yuan, D. Zhao, W. Zhuang and H.-C. Zhou, *Coord. Chem. Rev.*, 2009, **253**, 3042–3066.
- <sup>44</sup> N. L. Rosi, J. Kim, M. Eddaoudi, B. Chen, M. O’Keeffe and O. M. Yaghi, *J. Am. Chem. Soc.*, 2005, **127**, 1504–1518.
- <sup>45</sup> H. Furukawa, K. E. Cordova, M. O’Keeffe and O. M. Yaghi, *Science*, 2013, **341**, 1230444–1230444.
- <sup>46</sup> P. D. C. Dietzel, P. A. Georgiev, J. Eckert, R. Blom, T. Strässle and T. Unruh, *Chem. Commun.*, 2010, **46**, 4962.
- <sup>47</sup> M. T. Kapelowski, S. J. Geier, M. R. Hudson, D. Stück, J. A. Mason, J. N. Nelson, D. J. Xiao, Z. Hulvey, E. Gilmour, S. A. FitzGerald, M. Head-Gordon, C. M. Brown and J. R. Long, *J. Am. Chem. Soc.*, 2014, **136**, 12119–12129.
- <sup>48</sup> S. S. Kaye, A. Dailly, O. M. Yaghi and J. R. Long, *J. Am. Chem. Soc.*, 2007, **129**, 14176–14177.
- <sup>49</sup> A. R. Millward and O. M. Yaghi, *J. Am. Chem. Soc.*, 2005, **127**, 17998–17999.
- <sup>50</sup> R. Plessius, R. Kromhout, A. L. D. Ramos, M. Ferbinteanu, M. C. Mittelmeijer-Hazeleger, R. Krishna, G. Rothenberg and S. Tanase, *Chem. - Eur. J.*, 2014, **20**, 7922–7925.
- <sup>51</sup> N. L. Rosi, *Science*, 2003, **300**, 1127–1129.

- 
- <sup>52</sup> D. Saha, R. Zacharia, L. Lafi, D. Cossement and R. Chahine, *Int. J. Hydrog. Energy*, 2012, **37**, 5100–5107.
- <sup>53</sup> S. Chavan, F. Bonino, L. Valenzano, B. Civalleri, C. Lamberti, N. Acerbi, J. H. Cavka, M. Leistner and S. Bordiga, *J. Phys. Chem. C*, 2013, **117**, 15615–15622.
- <sup>54</sup> A. Das, P. D. Southon, M. Zhao, C. J. Kepert, A. T. Harris and D. M. D'Alessandro, *Dalton Trans.*, 2012, **41**, 11739.
- <sup>55</sup> T. Grant Glover, G. W. Peterson, B. J. Schindler, D. Britt and O. Yaghi, *Chem. Eng. Sci.*, 2011, **66**, 163–170.
- <sup>56</sup> Z. R. Herm, E. D. Bloch and J. R. Long, *Chem. Mater.*, 2014, **26**, 323–338.
- <sup>57</sup> P. Kanoo, A. C. Ghosh, S. T. Cyriac and T. K. Maji, *Chem. - Eur. J.*, 2012, **18**, 237–244.
- <sup>58</sup> J. Liu, J. Tian, P. K. Thallapally and B. P. McGrail, *J. Phys. Chem. C*, 2012, **116**, 9575–9581.
- <sup>59</sup> Q. Liu, L. Ning, S. Zheng, M. Tao, Y. Shi and Y. He, *Sci. Rep.*, 2013, **3**, 2916.
- <sup>60</sup> J. J. Perry, S. L. Teich-McGoldrick, S. T. Meek, J. A. Greathouse, M. Haranczyk and M. D. Allendorf, *J. Phys. Chem. C*, 2014, **118**, 11685–11698.
- <sup>61</sup> P. K. Thallapally, J. W. Grate and R. K. Motkuri, *Chem. Commun.*, 2012, **48**, 347
- <sup>62</sup> X. Wu, Z. Bao, B. Yuan, J. Wang, Y. Sun, H. Luo and S. Deng, *Microporous Mesoporous Mater.*, 2013, **180**, 114–122.
- <sup>63</sup> J. Liu, L. Chen, H. Cui, J. Zhang, L. Zhang and C.-Y. Su, *Chem Soc Rev*, 2014, **43**, 6011–6061.
- <sup>64</sup> J. Lee, O. K. Farha, J. Roberts, K. A. Scheidt, S. T. Nguyen and J. T. Hupp, *Chem. Soc. Rev.*, 2009, **38**, 1450.

- 
- <sup>65</sup> L. E. Kreno, K. Leong, O. K. Farha, M. Allendorf, R. P. Van Duyne and J. T. Hupp, *Chem. Rev.*, 2012, **112**, 1105–1125.
- <sup>66</sup> S. Achmann, G. Hagen, J. Kita, I. M. Malkowsky, C. Kiener and R. Moos, *Sensors*, 2009, **9**, 1574–1589.
- <sup>67</sup> S. Zhang, L. Han, L. Li, J. Cheng, D. Yuan and J. Luo, *Cryst. Growth Des.*, 2013, **13**, 5466–5472.
- <sup>68</sup> S. Rojas, P. S. Wheatley, E. Quartapelle-Procopio, B. Gil, B. Marszalek, R. E. Morris and E. Barea, *CrystEngComm*, 2013, **15**, 9364.
- <sup>69</sup> P. Horcajada, T. Chalati, C. Serre, B. Gillet, C. Sebrie, T. Baati, J. F. Eubank, D. Heurtaux, P. Clayette, C. Kreuz, J.-S. Chang, Y. K. Hwang, V. Marsaud, P.-N. Bories, L. Cynober, S. Gil, G. Férey, P. Couvreur and R. Gref, *Nat. Mater.*, 2010, **9**, 172–178.
- <sup>70</sup> J. Liu, Y. Wang, A. I. Benin, P. Jakubczak, R. R. Willis and M. D. LeVan, *Langmuir*, 2010, **26**, 14301–14307.
- <sup>71</sup> J. A. Mason, M. Veenstra and J. R. Long, *Chem. Sci.*, 2014, **5**, 32–51.
- <sup>72</sup> P. M. Schoenecker, C. G. Carson, H. Jasuja, C. J. J. Flemming and K. S. Walton, *Ind. Eng. Chem. Res.*, 2012, **51**, 6513–6519.
- <sup>73</sup> J. Liu, A. I. Benin, A. M. B. Furtado, P. Jakubczak, R. R. Willis and M. D. LeVan, *Langmuir*, 2011, **27**, 11451–11456.
- <sup>74</sup> S. R. Caskey, A. G. Wong-Foy and A. J. Matzger, *J. Am. Chem. Soc.*, 2008, **130**, 10870–10871.
- <sup>75</sup> P. D. C. Dietzel, B. Panella, M. Hirscher, R. Blom and H. Fjellvåg, *Chem. Commun.*, 2006, 959–961.

- 
- <sup>76</sup> L. Paseta, B. Seoane, D. Julve, V. Sebastián, C. Téllez and J. Coronas, *ACS Appl. Mater. Interfaces*, 2013, **5**, 9405–9410.
- <sup>77</sup> M. Faustini, J. Kim, G.-Y. Jeong, J. Y. Kim, H. R. Moon, W.-S. Ahn and D.-P. Kim, *J. Am. Chem. Soc.*, 2013, **135**, 14619–14626.
- <sup>78</sup> M. Li and M. Dincă, *J. Am. Chem. Soc.*, 2011, **133**, 12926–12929.
- <sup>79</sup> N. Campagnol, T. Van Assche, T. Boudewijns, J. Denayer, K. Binnemans, D. De Vos and J. Fransaer, *J. Mater. Chem. A*, 2013, **1**, 5827.
- <sup>80</sup> U. Mueller, *US Pat.*, 2007/0227898 A1, 2007.
- <sup>81</sup> J.-S. Lee, S. B. Halligudi, N.-H. Jang, D.-W. Hwang, J.-S. Chang and Y.-K. Hwang, *Bull. Korean Chem. Soc.*, 2010, **31**, 1489–1495.
- <sup>82</sup> E. Haque, N. A. Khan, J. H. Park and S. H. Jung, *Chem. - Eur. J.*, 2010, **16**, 1046–1052.
- <sup>83</sup> E. Haque and S. H. Jung, *Chem. Eng. J.*, 2011, **173**, 866–872.
- <sup>84</sup> N. A. Khan and S. H. Jung, *Coord. Chem. Rev.*, 2014, **285**, 11–23.
- <sup>85</sup> J. Ren, T. Segakweng, H. W. Langmi, N. M. Musyoka, B. C. North, M. Mathe and D. Bessarabov, *Int. J. Mater. Res.*, 2014, **105**, 516–519.
- <sup>86</sup> C.-M. Lu, J. Liu, K. Xiao and A. T. Harris, *Chem. Eng. J.*, 2010, **156**, 465–470.
- <sup>87</sup> K.-J. Kim, Y. J. Li, P. B. Kreider, C.-H. Chang, N. Wannemacher, P. K. Thallapally and H.-G. Ahn, *Chem. Commun.*, 2013, **49**, 11518.
- <sup>88</sup> P. M. Schoenecker, G. A. Belancik, B. E. Grabicka and K. S. Walton, *AIChE J.*, 2013, **59**, 1255–1262.
- <sup>89</sup> P. A. Bayliss, I. A. Ibarra, E. Pérez, S. Yang, C. C. Tang, M. Poliakoff and M. Schröder, *Green Chem.*, 2014, **16**, 3796–3802.

- 
- <sup>90</sup> M. Rubio-Martinez, M. P. Batten, A. Polyzos, K.-C. Carey, J. I. Mardel, K.-S. Lim and M. R. Hill, *Sci. Rep.*, 2014, **4**, 5443.
- <sup>91</sup> M. Gimeno-Fabra, A. S. Munn, L. A. Stevens, T. C. Drage, D. M. Grant, R. J. Kashtiban, J. Sloan, E. Lester and R. I. Walton, *Chem. Commun.*, 2012, **48**, 10642-10644.
- <sup>92</sup> S. Cadot, L. Veyre, D. Luneau, D. Farrusseng and E. Alessandra Quadrelli, *J Mater Chem A*, 2014, **2**, 17757–17763.
- <sup>93</sup> K.-J. Kim, R. P. Oleksak, E. B. Hostetler, D. A. Peterson, P. Chandran, D. M. Schut, B. K. Paul, G. S. Herman and C.-H. Chang, *Cryst. Growth Des.*, 2014, **14**, 5349–5355.
- <sup>94</sup> S. Horikoshi and N. Serpone, *Microwaves in Nanoparticle Synthesis: Fundamentals and Applications*, Wiley-VCH, 2013.
- <sup>95</sup> R. P. Oleksak, B. T. Flynn, D. M. Schut and G. S. Herman, *Phys. Status Solidi A*, 2014, **211**, 219–225.
- <sup>96</sup> E. B. Hostetler, K.-J. Kim, R. P. Oleksak, R. C. Fitzmorris, D. A. Peterson, P. Chandran, C.-H. Chang, B. K. Paul, D. M. Schut and G. S. Herman, *Mater. Lett.*, 2014, **128**, 54–59.
- <sup>97</sup> V. Sebastian Cabeza, S. Kuhn, A. A. Kulkarni and K. F. Jensen, *Langmuir*, 2012, **28**, 7007–7013.
- <sup>98</sup> F. Bonino, S. Chavan, J. G. Vitillo, E. Groppo, G. Agostini, C. Lamberti, P. D. C. Dietzel, C. Prestipino and S. Bordiga, *Chem. Mater.*, 2008, **20**, 4957–4968.
- <sup>99</sup> V. K. LaMer and R. H. Dinegar, *J. Am. Chem. Soc.*, 1950, **72**, 4847–4854.

- 
- <sup>100</sup> S. Brunauer, L. S. Deming, W. E. Deming and E. Teller, *J. Am. Chem. Soc.*, 1940, **62**, 1723–1732.
- <sup>101</sup> A. P. Nelson, O. K. Farha, K. L. Mulfort and J. T. Hupp, *J. Am. Chem. Soc.*, 2009, **131**, 458–460.
- <sup>102</sup> C.-S. Tsao, C.-Y. Chen, T.-Y. Chung, C.-J. Su, C.-H. Su, H.-L. Chen, U.-S. Jeng, M.-S. Yu, P.-Y. Liao, K.-F. Lin and Y.-R. Tzeng, *J. Phys. Chem. C*, 2010, **114**, 7014–7020.
- <sup>103</sup> N. T. K. Thanh, N. Maclean and S. Mahiddine, *Chem. Rev.*, 2014, **114**, 7610–7630.
- <sup>104</sup> E. C. Vreeland, J. Watt, G. B. Schober, B. G. Hance, M. J. Austin, A. D. Price, B. D. Fellows, T. C. Monson, N. S. Hudak, L. Maldonado-Camargo, A. C. Bohorquez, C. Rinaldi and D. L. Huber, *Chem. Mater.*, 2015, **27**, 6059–6066.
- <sup>105</sup> E. B. Hostetler, K.-J. Kim, R. P. Oleksak, R. C. Fitzmorris, D. A. Peterson, P. Chandran, C.-H. Chang, B. K. Paul, D. M. Schut and G. S. Herman, *Mater. Lett.*, 2014, **128**, 54–59.
- <sup>106</sup> K.-J. Kim, R. P. Oleksak, E. B. Hostetler, D. A. Peterson, P. Chandran, D. M. Schut, B. K. Paul, G. S. Herman and C.-H. Chang, *Cryst. Growth Des.*, 2014, **14**, 5349–5355.
- <sup>107</sup> R. C. Fitzmorris, R. P. Oleksak, Z. Zhou, B. D. Mangum, J. N. Kurtin and G. S. Herman, *J. Nanoparticle Res.*, 2015, **17**.
- <sup>108</sup> Y. G. Chung, J. Camp, M. Haranczyk, B. J. Sikora, W. Bury, V. Krungleviciute, T. Yildirim, O. K. Farha, D. S. Sholl and R. Q. Snurr, *Chem. Mater.*, 2014, **26**, 6185–6192.

- 
- <sup>109</sup> E. M. Dias and C. Petit, *J Mater Chem A*, 2015, **3**, 22484–22506.
- <sup>110</sup> T. Rodenas, I. Luz, G. Prieto, B. Seoane, H. Miro, A. Corma, F. Kapteijn, F. X. Llabrés i Xamena and J. Gascon, *Nat. Mater.*, 2014, **14**, 48–55.
- <sup>111</sup> J. Liu, L. Chen, H. Cui, J. Zhang, L. Zhang and C.-Y. Su, *Chem Soc Rev*, 2014, **43**, 6011–6061.
- <sup>112</sup> B. Liu, *J. Mater. Chem.*, 2012, **22**, 10094.
- <sup>113</sup> B. Li, M. Chrzanowski, Y. Zhang and S. Ma, *Coord. Chem. Rev.*, 2016, **307**, 106–129.
- <sup>114</sup> S. Cadot, L. Veyre, D. Luneau, D. Farrusseng and E. Alessandra Quadrelli, *J Mater Chem A*, 2014, **2**, 17757–17763.
- <sup>115</sup> G. H. Albuquerque, R. C. Fitzmorris, M. Ahmadi, N. Wannemacher, P. K. Thallapally, B. P. McGrail and G. S. Herman, *CrystEngComm*, 2015, **17**, 5502–5510.
- <sup>116</sup> M. Taddei, D. A. Steitz, J. A. Van Bokhoven and M. Ranocchiari, *Chem. - Eur. J.*, 2016, **22**, 3245–3249.
- <sup>117</sup> T. Tsuruoka, S. Furukawa, Y. Takashima, K. Yoshida, S. Isoda and S. Kitagawa, *Angew. Chem. Int. Ed.*, 2009, **48**, 4739–4743.
- <sup>118</sup> S. Diring, S. Furukawa, Y. Takashima, T. Tsuruoka and S. Kitagawa, *Chem. Mater.*, 2010, **22**, 4531–4538.
- <sup>119</sup> M. Sindoro, N. Yanai, A.-Y. Jee and S. Granick, *Acc. Chem. Res.*, 2014, **47**, 459–469.
- <sup>120</sup> A. Umemura, S. Diring, S. Furukawa, H. Uehara, T. Tsuruoka and S. Kitagawa, *J. Am. Chem. Soc.*, 2011, **133**, 15506–15513.

- 
- <sup>121</sup> A. Schaate, P. Roy, A. Godt, J. Lippke, F. Waltz, M. Wiebcke and P. Behrens, *Chem. - Eur. J.*, 2011, **17**, 6643–6651.
- <sup>122</sup> M. Y. Masoomi, S. Beheshti and A. Morsali, *Cryst. Growth Des.*, 2015, **15**, 2533–2538.
- <sup>123</sup> R. J. Marshall, C. L. Hobday, C. F. Murphie, S. L. Griffin, C. A. Morrison, S. A. Moggach and R. S. Forgan, *J Mater Chem A*, 2016, **4**, 6955–6963.
- <sup>124</sup> X. Zhu, B. Li, J. Yang, Y. Li, W. Zhao, J. Shi and J. Gu, *ACS Appl. Mater. Interfaces*, 2015, **7**, 223–231.
- <sup>125</sup> J. B. DeCoste and G. W. Peterson, *Chem. Rev.*, 2014, **114**, 5695–5727.
- <sup>126</sup> Z. Hasan and S. H. Jhung, *J. Hazard. Mater.*, 2015, **283**, 329–339.
- <sup>127</sup> S. Qiu, M. Xue and G. Zhu, *Chem Soc Rev*, 2014, **43**, 6116–6140.
- <sup>128</sup> N. Wang, A. Mundstock, Y. Liu, A. Huang and J. Caro, *Chem. Eng. Sci.*, 2015, **124**, 27–36.
- <sup>129</sup> X. Luo, L. Ding and J. Luo, *J. Chem. Eng. Data*, 2015, **60**, 1732–1743.
- <sup>130</sup> C. Wang, X. Liu, J. P. Chen and K. Li, *Sci. Rep.*, 2015, **5**, 16613.
- <sup>131</sup> J. Liu, A. I. Benin, A. M. B. Furtado, P. Jakubczak, R. R. Willis and M. D. LeVan, *Langmuir*, 2011, **27**, 11451–11456.
- <sup>132</sup> H. B. Tanh Jeazet, C. Staudt and C. Janiak, *Dalton Trans.*, 2012, **41**, 14003.
- <sup>133</sup> J. Campbell, J. D. S. Burgal, G. Szekely, R. P. Davies, D. C. Braddock and A. Livingston, *J. Membr. Sci.*, 2016, **503**, 166–176.
- <sup>134</sup> J. B. DeCoste, M. S. Denny, Jr., G. W. Peterson, J. J. Mahle and S. M. Cohen, *Chem Sci*, 2016, **7**, 2711–2716.

- 
- <sup>135</sup> F. Bonino, S. Chavan, J. G. Vitillo, E. Groppo, G. Agostini, C. Lamberti, P. D. C. Dietzel, C. Prestipino and S. Bordiga, *Chem. Mater.*, 2008, **20**, 4957–4968.
- <sup>136</sup> V. K. LaMer and R. H. Dinegar, *J. Am. Chem. Soc.*, 1950, **72**, 4847–4854.
- <sup>137</sup> S. Brunauer, L. S. Deming, W. E. Deming and E. Teller, *J. Am. Chem. Soc.*, 1940, **62**, 1723–1732.
- <sup>138</sup> A. Das, P. D. Southon, M. Zhao, C. J. Kepert, A. T. Harris and D. M. D'Alessandro, *Dalton Trans.*, 2012, **41**, 11739.
- <sup>139</sup> M. J. K. Ahmed and M. Ahmaruzzaman, *J. Water Process Eng.*, 2016, **10**, 39–47.
- <sup>140</sup> R. Jiang, H. R. Kunz and J. M. Fenton, *J. Membr. Sci.*, 2006, **272**, 116–124.
- <sup>141</sup> J. Zeng, D. Jean, C. Ji and S. Zou, *Langmuir*, 2012, **28**, 957–964.
- <sup>142</sup> N. Chourdakis and G. A. Voyiatzis, *J. Polym. Sci. Part B Polym. Phys.*, 2007, **45**, 2509–2517.
- <sup>143</sup> A. L. Maclean, R. S. Armstrong and B. J. Kennedy, *J. Raman Spectrosc.*, 1993, **24**, 897–901.
- <sup>144</sup> I. Kendrick, A. Yakaboski, E. Kingston, J. Doan, N. Dimakis and E. S. Smotkin, *J. Polym. Sci. Part B Polym. Phys.*, 2013, **51**, 1329–1334.
- <sup>145</sup> M. Webber, N. Dimakis, D. Kumari, M. Fuccillo and E. S. Smotkin, *Macromolecules*, 2010, **43**, 5500–5502.
- <sup>146</sup> D. S. Warren and A. J. McQuillan, *J. Phys. Chem. B*, 2008, **112**, 10535–10543.
- <sup>147</sup> M. Moskovits, *Rev. Mod. Phys.*, 1985, **57**, 783–826.
- <sup>148</sup> Z. D. Schultz, Z. V. Feng, M. E. Biggin and A. A. Gewirth, *J. Electrochem. Soc.*, 2006, **153**, C97.

- 
- <sup>149</sup> E. J. Ayars, H. D. Hallen and C. L. Jahncke, *Phys. Rev. Lett.*, 2000, **85**, 4180-4183.
- <sup>150</sup> J. Horakova, K. Tomankova, M. Harvanova, S. Hradilova, V. Masek, J. Malohlava, L. Malina, B. Manisova, K. Kejlova, D. Jirova and H. Horakova, *Microscopy: advances in scientific research and education*, Formatex Research Center, 2014, vol. 1.
- <sup>151</sup> N. Kazemi-Zanjani, E. Kergrene, L. Liu, T.-K. Sham and F. Lagugné-Labarthe, *Sensors*, 2013, **13**, 12744–12759.
- <sup>152</sup> A. Gruger, A. Régis, T. Schmatko and P. Colomban, *Vib. Spectrosc.*, 2001, **26**, 215–225.
- <sup>153</sup> I. Kendrick, D. Kumari, A. Yakaboski, N. Dimakis and E. S. Smotkin, *J. Am. Chem. Soc.*, 2010, **132**, 17611–17616.
- <sup>154</sup> F. Fu and Q. Wang, *J. Environ. Manage.*, 2011, **92**, 407–418.
- <sup>155</sup> Z. Jiang, P. Gao, L. Yang, C. Huang and Y. Li, *Anal. Chem.*, 2015, **87**, 12177–12182.
- <sup>156</sup> R. J. T. Houk, B. W. Jacobs, F. E. Gabaly, N. N. Chang, A. A. Talin, D. D. Graham, S. D. House, I. M. Robertson and M. D. Allendorf, *Nano Lett.*, 2009, **9**, 3413–3418.
- <sup>157</sup> Y. Y. Xiong, J. Q. Li, L. L. Gong, X. F. Feng, L. N. Meng, L. Zhang, P. P. Meng, M. B. Luo and F. Luo, *J. Solid State Chem.*, 2017, **246**, 16–22.
- <sup>158</sup> A. Jamali, A. Azhdari Tehrani, F. Shemirani and A. Morsali, *Dalton Trans*, 2016, **45**, 9193-9200.
- <sup>159</sup> M. M. Nasef and A. H. Yahaya, *Desalination*, 2009, **249**, 677–681.

- 
- <sup>160</sup> A. J. Howarth, Y. Liu, P. Li, Z. Li, T. C. Wang, J. T. Hupp and O. K. Farha, *Nat. Rev. Mater.*, 2016, **1**, 15018.
- <sup>161</sup> Z. Qiao, N. Wang, J. Jiang and J. Zhou, *Chem Commun*, 2016, **52**, 974–977.
- <sup>162</sup> B. Gole, U. Sanyal, R. Banerjee and P. S. Mukherjee, *Inorg. Chem.*, 2016, **55**, 2345–2354.
- <sup>163</sup> G. Chang, M. Huang, Y. Su, H. Xing, B. Su, Z. Zhang, Q. Yang, Y. Yang, Q. Ren, Z. Bao and B. Chen, *Chem Commun*, 2015, **51**, 2859–2862.
- <sup>164</sup> “Primary Energy Production by Source”, U.S. Energy Information Administration (EIA), Monthly Energy Review January of 2017.
- <sup>165</sup> N. Ali, A. Hussain, R. Ahmed, M.K. Wang, C. Zhao, B.U. Haq, Y.Q. Fu, *Renew. Sustain. Energy Rev.*, 2016, **59**, 726–737.
- <sup>166</sup> M.A. Green, K. Emery, Y. Hishikawa, W. Warta, E.D. Dunlop, *Prog. Photovolt. Res. Appl.*, 2016, **24**, 3–11.
- <sup>167</sup> W. Shockley, H.J. Queisser, *J. Appl. Phys.*, 1961, **32**, 510–519.
- <sup>168</sup> T. Todorov, O. Gunawan, S. Guha, *Mol. Syst. Eng.*, 2016, **1**, 370–376.
- <sup>169</sup> K. Ramasamy, H. Sims, W.H. Butler, A. Gupta, *Chem. Mater.*, 2014, **26**, 2891–2899
- <sup>170</sup> L. Shi, C. Wu, J. Li, J. Ding, *J. Alloys Compd.*, 2017, **694**, 132–135.
- <sup>171</sup> N.D. Franzer, N.R. Paudel, C. Xiao, Y. Yan, *Photovolt. Spec. Conf. PVSC 2014 IEEE 40th*, IEEE, 2014, 2326–2328.
- <sup>172</sup> S.C. Riha, A.A. Koegel, J.D. Emery, M.J. Pellin, A.B.F. Martinson, *ACS Appl. Mater. Interfaces*, 2017, **9**, 4667–4673.

- 
- <sup>173</sup> Y.C. Choi, E.J. Yeom, T.K. Ahn, S.I. Seok, *Angew. Chem. Int. Ed.*, 2015, **54**, 4005–4009.
- <sup>174</sup> S.G. Kwon, T. Hyeon, *Small.*, 2011, **7**, 2685–2702.
- <sup>175</sup> S. Ikeda, S. Sogawa, Y. Tokai, W. Septina, T. Harada, M. Matsumura, *RSC Adv.*, 2014, **4**, 40969-40972.
- <sup>176</sup> H. Katagiri, K. Jimbo, W.S. Maw, K. Oishi, M. Yamazaki, H. Araki, A. Takeuchi, *Thin Solid Films*, 2009, **517**, 2455–2460.
- <sup>177</sup> B. Yang, L. Wang, J. Han, Y. Zhou, H. Song, S. Chen, J. Zhong, L. Lv, D. Niu, J. Tang, *Chem. Mat.*, 2014, **26**, 3135-3143.
- <sup>178</sup> A. Welch, L. Baranowski, P. Zawadzki, C. DeHart, S. Johnston, S. Lany, C. A. Wolden, A. Zakutayev, *Prog. Photovolt: Res. Appl.*, 2016, **24**, 929-939.
- <sup>179</sup> J. Heo, R. Ravichandran, C.F. Reidy, J. Tate, J.F. Wager, D.A. Keszler, *Adv. Energy Mater.*, 2015, **5**, 1401506.
- <sup>180</sup> M. Grioni, J.B. Goedkoop, R. Schoorl, F.M.F. De Groot, J.C. Fuggle, F. Schäfers, E.E. Koch, G. Rossi, J.-M. Esteva, R.C. Karnatak, *Phys. Rev. B.*, 1989, **39**, 1541-1545.
- <sup>181</sup> W. Jaegermann, A. Klein and T. Mayer, *Adv. Mater.*, 2009, **21**, 4196–4206.
- <sup>182</sup> R. C. Peterson, I. Miller, *Mineralogical Magazine*, 1986, **50**, 717-721.
- <sup>183</sup> A. Pfitzner, T. Bernert, *Zeitschrift für Kristallographie*, 2004, **219**, 20-26.
- <sup>184</sup> M.H. Braga, J.A. Ferreira, C. Lopes, L.F. Malheiros, *Trans. Tech. Publ.*, 2008, **587-588**, 435–439.
- <sup>185</sup> B.J. Skinner, F. D. Luce, E. Makovicky, *Economic Geology*, 1972, **67**, 924-938.

---

<sup>186</sup> J.R. Vegelius, K.O. Kvashnina, H. Hollmark, M. Klintonberg, Y.O. Kvashnin, I.L.

Soroka, L. Werme, S.M. Butorin, *J. Phys. Chem. C.*, 2012, **116**, 22293–22300.